

APPLICATIONS OF ^{129}Xe NMR SIGNAL ENHANCEMENT:
STUDIES OF THE GAS CLATHRATE HYDRATE FORMATION
AND EXPLORING XENON-PROTEIN INTERACTIONS

By

VINCENT J. STORHAUG

A DISSERTATION PRESENTED TO THE GRADUATE SCHOOL
OF THE UNIVERSITY OF FLORIDA IN PARTIAL FULFILLMENT
OF THE REQUIREMENTS FOR THE DEGREE OF
DOCTOR OF PHILOSOPHY

UNIVERSITY OF FLORIDA

2002

ACKNOWLEDGMENTS

At this time, I would like to recognize officially those individuals who have made my appointment in the Department of Chemistry, at the University of Florida, a successful venture. To Dr. C. Russell Bowers, I express my gratitude and my appreciation. The path has been a long and arduous one, and without his assistance and guidance, success would not have been possible.

I would like to take a moment to thank the support staff of the department. Dr. Ion Ghiviriga and Dr. Wallace Brey, of the departmental NMR services, provided guidance and technical support, and made special accommodations for our experiments. Joe F. Caruso, scientific glassblower, and the members of the departmental machine shop provided technical assistance and craftsmanship without which the path would have been much more difficult. Of course, this statement of appreciation would be incomplete without including the secretarial staff and stockroom personnel, who were always willing to assist and provide information.

The members of the Bowers Research Group do indeed deserve appropriate recognition. Both the current members (Anil Patel, Bhavin Adhyaru, Anthony Zook, Joshua Caldwell) and prior members (Gail Fanucci, John Osegovic, Charles Webster) have been supportive and helpful. With their help I have grown as a person and a researcher, and although that growth is a continuing process, I have come a long way from the person I was when first I joined the department.

My family and friends have been essential to my success. As an official note, but on a definitely personal level, I would like to acknowledge the support of my parents, who never wavered in their decision to back any decision I made. For them as well, it has been a long journey, and my only hope is that in the end, I have done everything in my power to make them and the other members of my family proud.

Finally, it is my desire to honor the memory of Karl Walther, scientific and artistic glassblower. Beyond the appreciation that I owe him for his assistance and guidance, I wish to convey my admiration of his gentle soul. The “Salt of the Earth” has perhaps never been a more appropriate epitaph.

TABLE OF CONTENTS

	<u>page</u>
ACKNOWLEDGMENTS	ii
LIST OF TABLES.....	ix
LIST OF FIGURES	x
ABSTRACT.....	xiv
CHAPTER 1: THESIS OVERVIEW	
Historical Perspective	1
Dissertation Overview	5
CHAPTER 2: CHARACTERIZATION OF MICROPOROUS MATERIALS WITH ¹²⁹ Xe NMR	
Introduction.....	7
Applications of ¹²⁹ Xe NMR to the Study of Microporous Materials.....	8
Estimations of Pore Dimensions and Determinations of Cavity Symmetries	10
Isotropic and Anisotropic ¹²⁹ Xe NMR Line Shapes for Xenon Inclusion Compounds	13
¹²⁹ Xe NMR Characteristics of Xenon Clathrate Hydrates	16
¹²⁹ Xe NMR Line Shapes for Occupied Small and Large Cavities of Clathrate Hydrates	18
Summary	21

CHAPTER 3: INTRODUCTION TO THE SPIN EXCHANGE OPTICAL PUMPING (SEOP) ENHANCEMENT OF THE ^{129}Xe NMR SIGNAL

Introduction.....	22
Non-Equilibrium Techniques for Enhancement of the ^{129}Xe NMR Signal.....	23
Hartmann-Hahn Cross Polarization.....	23
Alkali Metal-Noble Gas Spin Exchange Optical Pumping.....	27
Optical Pumping of Rubidium Metal Vapor.....	28
Rubidium-Xenon Spin Exchange Through Collisional Processes.....	34
Reducing the rate of Nuclear Spin Relaxation Due to Wall Interactions	38
Summary.....	39

CHAPTER 4: RECENT APPLICATIONS OF SEOP ENHANCED ^{129}Xe NMR

Introduction.....	41
Selected Applications.....	43
Applications of SEOP Enhanced ^{129}Xe NMR to Surface	
Adsorption Studies.....	43
Investigating Local Environments in Microporous Materials: Zeolites	45
Polarization Transfer Techniques	46
Selective Binding of Xenon In Inclusion Compounds: Cryptophane-A	50
Time-Resolved Experiments Using SEOP Enhanced ^{129}Xe NMR.....	52
Summary.....	54

CHAPTER 5: STRUCTURES AND THERMODYNAMICS OF GAS CLATHRATE HYDRATES

Introduction.....	55
Historical Perspective	56
Structural Properties of the Gas Clathrate Hydrates.....	58
The Type I and Type II Clathrate Hydrate Structures	58
Thermodynamics of Gas Clathrate Hydrates.....	64
Applying the Solid-Solution Model to Gas Clathrate Hydrate	
Thermodynamics.....	67
Summary	73

CHAPTER 6: PROPOSED MECHANISMS AND KINETICS OF TYPE I XENON CLATHRATE HYDRATE FORMATION

Introduction.....	75
Proposed Models for Gas Clathrate Hydrate Nucleation	
Induction Periods Observed for Selected Simple Gas Hydrate Clathrates	76
Differences in the Observed Induction Periods	79
Modeling Gas Clathrate Hydrate Crystal Growth Following the	
Induction Period.....	81
Modeling Gas Clathrate Hydrate Formations at the Molecular Level.....	85
The Use SEOP Enhanced ^{129}Xe NMR to Monitor Clathrate	
Hydrate Formation	88
Summary of Prior Work.....	91
Original Proposed Kinetics Models for the Formation of the Type I Clathrate Hydrate	
Model I: Interdependency of Cavity Formation	94
Model II: Two-Step Guest Enclathration.....	99

CHAPTER 7: MONITORING XENON CLATHRATE HYDRATE FORMATION THROUGH GAS UPTAKE MEASUREMENTS AND SEOP ENHANCEMENT OF ^{129}Xe NMR SIGNAL

Introduction.....	102
Experimental	
Preparation of D_2O Ice	105
Time-Resolved Pressure Measurements for Clathrate Hydrate Formation ...	105
Spin Exchange Optical Pumping of ^{129}Xe	106
Providing SEOP Enhanced ^{129}Xe to a Finely Powdered Ice Sample.....	108
Results and Discussion	
Gas Uptake Data, Pressure-Time Dependence Measurements.....	110
Temperature Dependence of ^{129}Xe NMR Lineshape.....	111
Time-Resolved SEOP Enhanced ^{129}Xe NMR Spectra.....	118
Conclusions.....	123

CHAPTER 8: SEOP ENHANCED ^{129}Xe NMR SPECTROSCOPY OF SF_6/Xe AND ACETONE- d_6/Xe MIXED TYPE II CLATHRATE HYDRATES

Introduction.....	126
-------------------	-----

Experimental	
Preparation of D ₂ O Ice.....	129
Formation of the Type I Clathrate Hydrate.....	130
Formation of the Type II SF ₆ /Xe Clathrate Hydrate.....	132
Formation of the Acetone- <i>d</i> ₆ /Xe Type II Clathrate Hydrate	132
Spin Exchange Optical Pumping of ¹²⁹ Xe	133
Acquisition of NMR Spectra	133
Results and Discussion	
¹²⁹ Xe NMR Spectra of Mixed Type II Clathrate Deuteriohydrates	134
Time-Resolved ¹⁹ F NMR of the Type II SF ₆ and the SF ₆ /Xe Deuteriohydrates	141
Time Dependence of the ¹²⁹ Xe Enclathration of the Mixed Type II Clathrate Hydrates	148
Conclusions.....	154
CHAPTER 9: EXPLORING SURFACES AND CAVITIES IN SELECTED OTHER PROTEINS BY SEOP ENHANCED ¹²⁹ XE NMR	
Introduction.....	158
Description of Proteins Selected for ¹²⁹ Xe NMR Studies.....	161
Experimental	
Preparation of Lyophilized Proteins	165
Generation of SEOP Enhanced ¹²⁹ Xe.....	166
SEOP Enhanced ¹²⁹ Xe NMR of Lyophilized Protein Samples	167
¹²⁹ Xe NMR of Protein Solutions.....	169
Gas Adsorption Isotherm Measurements.....	169
Results and Discussion	
Solution State ¹²⁹ Xe NMR	171
SEOP Enhanced ¹²⁹ Xe NMR Studies on Lyophilized Proteins	174
N ₂ , Xe and CH ₄ Gas Adsorption Isotherms	184
Conclusions.....	187
APPENDIX I: Experimental Apparati for the Generation of SEOP Enhanced ¹²⁹ Xe NMR.....	190
APPENDIX II: Calculating the ¹²⁹ Xe NMR Signal Enhancement.....	197
APPENDIX III: Apparatus for Measurement of the Time-Dependence of Pressure During the Formation of the Xenon Type I Clathrate Hydrate.....	202

REFERENCES	204
BIOGRAPHICAL SKETCH.....	215

LIST OF TABLES

<u>Table</u>	<u>page</u>
Table 2-1 Summary of Typical ^{129}Xe NMR Parameters for The Type I and Type II Gas Clathrate Hydrates	19
Table 3-1 Measured ^{129}Xe T_1 Values for SEOP Enhancement of ^{129}Xe With Optically Pumped Rubidium Vapor In Coated and Uncoated Cells	39
Table 5-1 A Summary of Physical Characteristics of the Type I and Type II Gas Hydrate Clathrates	60
Table 5-2 Occupancies of the Cavities of Type I Simple Clathrate Hydrates, at the Dissociation Pressure and 0 °C, as Calculated Through Both Experiment and Theory	65
Table 5-3 Ratios of Molecular Diameters To Cavity Diameters for Selected Type I Gas Hydrate-Forming Molecules.....	68
Table 8-1 Summary of ^{129}Xe NMR Chemical Shielding Parameters (2 ppm Error), Referenced to the Gaseous ^{129}Xe Signal, in the Type I Xenon Deuteriohydrate and the Type II SF_6/Xe and Acetone- d_6/Xe Deuteriohydrates	141
Table 9-1 Parameters from Adsorption Isotherm Data for Lyophilized Proteins	185

LIST OF FIGURES

<u>Figure</u>	<u>page</u>
Figure 2-1 The thermally polarized ^{129}Xe NMR spectrum of the type I simple xenon clathrate deuteriohydrate	17
Figure 3-1 Enhancement of nuclear magnetization, M_z , may be accomplished through non-equilibrium techniques	24
Figure 3-2 The Hartmann-Hahn cross polarization pulse sequence brings the two reservoirs of the I and S spins into thermal contact	26
Figure 3-3 Energy Level Diagram for ^{87}Rb	30
Figure 3-4 The physics of the optical pumping of an alkali metal vapor, where pressure broadening has made the fine structure irresolvable	31
Figure 3-5 Mechanisms for spin exchange of optically pumped alkali metal vapor with a noble gas	35
Figure 4-1 The pulse sequence employed by Long and co-workers to transfer nuclear spin polarization from a reservoir of laser-polarized ^{129}Xe to the protons on the surface of poly(triarylcarbonyl) at 213 K	49
Figure 5-1 Three of the most common cavity types found in clathrate hydrates	59
Figure 5-2 Clathrate hydrates are crystalline substances in which the hydrogen bonding of water molecules forms large, distinct cages	62
Figure 5-3 Clathrate hydrate forming capabilities of selected gases	63
Figure 6-1 The quasi-liquid layer covers the surfaces of ice crystals and may be a few molecular layers to nanometers thick, depending on the temperature	81

Figure 6-2	(Above is depicted) a pictorial representation of the Ullrich-Selim-Sloan kinetics scheme	85
Figure 6-3	Pictorial representations of the formation kinetics scheme proposed by Pietraß and co-workers.....	92
Figure 6-4	Pictorial representation of a proposed mechanism for the formation of the simple type I clathrate hydrate, involving the interdependency of the formations of the small and large cavities	96
Figure 7-1	10 mm O.D. medium wall NMR tube, modified for the type I clathrate hydrate formation	107
Figure 7-2	Monitoring the enclathration of xenon gas as a function of pressure ...	109
Figure 7-3	SEOP enhanced ^{129}Xe NMR spectra of the xenon type I hydrate clathrate at selected temperatures between 203 and 300 K	112
Figure 7-4	Theoretical fit of the CSA for the SEOP enhanced ^{129}Xe NMR spectrum of the xenon type I clathrate hydrate at 253 K	113
Figure 7-5	Summary of signal intensities for the SEOP enhanced ^{129}Xe NMR spectra of the xenon type I clathrate hydrate taken to 300 K, after formation at 223 K	115
Figure 7-6	Hyperpolarized ^{129}Xe NMR spectra acquired as a function of time following insertion of the NMR tube containing pulverized D_2O ice and spin-polarized ^{129}Xe into the NMR probe at 223 K	117
Figure 7-7	Summary plot for time-resolved ^{129}Xe NMR detection of the exposure of pulverized D_2O ice to SEOP ^{129}Xe NMR at a probe temperature of 233 K	119
Figure 7-8	Vertically stacked plot for time-resolved ^{129}Xe NMR detection of the exposure of pulverized D_2O ice to SEOP enhanced ^{129}Xe NMR at a probe temperature of 223 K	120
Figure 7-9	Summary plot for time-resolved ^{129}Xe NMR detection of the exposure of pulverized D_2O ice to hyperpolarized ^{129}Xe NMR at a probe temperature of 223 K	121
Figure 7-9	Summary plot for time-resolved ^{129}Xe NMR detection of the exposure of pulverized D_2O ice to hyperpolarized ^{129}Xe NMR at a probe temperature of 233 K	122

Figure 8-1	Diagrams of the vacuum manifolds used to prepare the type II clathrate hydrate samples	131
Figure 8-2	SEOP enhanced ^{129}Xe NMR spectra (110.7 MHz) of SF_6/Xe type II clathrate deuteriohydrates at 223 K	135
Figure 8-3	SEOP enhanced ^{129}Xe NMR spectrum (110.7 MHz) of the acetone- d_6/Xe type II clathrate deuteriohydrate formed at 223 K	138
Figure 8-4	Comparison of the SEOP enhanced ^{129}Xe NMR spectra (110.7 MHz) of the 5^{12} cavity signals in the (a) acetone- d_6/Xe and the (b) SF_6/Xe type II clathrate deuteriohydrates recorded at 223 K	140
Figure 8-5	^{19}F NMR spectra of SF_6 enclathrated into the $5^{12}6^4$ cavities type II SF_6 clathrate deuteriohydrate recorded at 223 K	142
Figure 8-6	Time-resolved ^{19}F NMR spectra of SF_6 enclathrated into $5^{12}6^4$ cavities of the type II SF_6/Xe mixed clathrate deuteriohydrate recorded at a probe temperature of 223 K	144
Figure 8-7	(a) Overlay of the ^{19}F NMR spectra of the SF_6 and the SF_6/Xe type II deuteriohydrates at 223 K; (b) Overlay of the SEOP ^{129}Xe NMR spectra of the SF_6/Xe type II and the Xe type I deuteriohydrates at 223 K	146
Figure 8-8	Time-resolved SEOP enhanced ^{129}Xe NMR spectra (110.7 MHz) following the formation of the acetone- d_6/Xe clathrate hydrates, <i>in situ</i>	149
Figure 8-9	Time dependence of the SEOP enhanced ^{129}Xe NMR absorption signal integrals acquired during the <i>in situ</i> formation of the acetone- d_6/Xe type II deuteriohydrate at 223 K	151
Figure 8-10	Time dependence of the SEOP enhanced ^{129}Xe NMR absorption signal integrals acquired during the <i>in situ</i> formation of the SF_6/Xe type II deuteriohydrate at 223 K	152
Figure 9-1	The tertiary structure of metmyoglobin	162
Figure 9-2	The tertiary structure of hen egg white lysozyme	164
Figure 9-3	The conventional ^{129}Xe NMR spectra, depicted in (a), was acquired as a function of temperature for a solution containing 3.3 mM metMb in 0.50 mL of ethylene glycol, 0.50 mL of methanol, and 1.0 mL of D_2O	172

Figure 9-4	The conventional ^{129}Xe NMR spectra are depicted in (a) for a 1 mL solution containing 50 mg of lipoxigenase, type SBL-1 from soybeans, dissolved in a 0.01 mM potassium cryoprotectant solvent	173
Figure 9-5	SEOP enhanced ^{129}Xe NMR study of xenon adsorption on 100-150 mg samples of lyophilized powders of (a) hen egg white lysozyme (Hel), (b) metmyoglobin (metMb), (c) methemoglobin (metHb), and (d) soybean lipoxigenase (SBL-1) at several temperatures	175
Figure 9-6	SEOP Enhanced ^{129}Xe NMR study of xenon adsorption on 142 mg of lyophilized soybean lipoxigenase (SBL-1) exposed to (a) 2.5 atm (298 K) and (b) 6.0 atm of enhanced xenon	178
Figure 9-7	Xenon and methane adsorption isotherms for binding at 210 K to lyophilized proteins, lipoxigenase (SBL-1), metmyoglobin (metMb), and hen egg white lysozyme (Hel)	185
Figure AI-1	Diagram of an $Rb\text{-}^{129}\text{Xe}$ SEOP apparatus mounted atop the laser table	191
Figure AI-2	Modified 10 mm O.D. medium-wall NMR tube	193
Figure AI-3	Diagram of an $Rb\text{-}^{129}\text{Xe}$ SEOP apparatus mounted atop the <i>Bruker Avance 400</i> spectrometer	195
Figure AII-1	Enhancement of the ^{129}Xe NMR signal obtained through spin exchange with optically pumped rubidium vapor with the magnet-top system	200
Figure AIII-1	Apparatus for real-time measurement of pressure during the formation of the xenon type I clathrate hydrate	203

Abstract of Thesis Presented to the Graduate School
of the University of Florida in Partial Fulfillment of the
Requirements for the Degree of Doctor of Philosophy

APPLICATIONS OF ^{129}Xe NMR SIGNAL ENHANCEMENT:
STUDIES OF THE GAS CLATHRATE HYDRATE FORMATION
AND EXPLORING XENON-PROTEIN INTERACTIONS

By

VINCENT J. STORHAUG

December 2002

Chairman: Dr. Clifford R. Bowers
Major Department: Department of Chemistry

Formation reactions of the xenon type I clathrate deuteriohydrates on the surfaces of ice crystals for temperatures in the range of 203 to 263 K were studied using spin exchange optically pumped (SEOP) ^{129}Xe NMR. The signals arising from ^{129}Xe enclathrated into the tetrakaidecahedral and the dodecahedral cavities of the hydrate clathrate are well resolved. The sensitivity enhancement of the ^{129}Xe NMR signal achieved through the alkali metal-noble gas SEOP technique permits the acquisition of a spectrum with a single scan using only a small tip angle. As a result, the combination of ^{129}Xe NMR signal enhancement and the use of small tip angles provided the ability to monitor both the formations and decomposition reactions of the xenon deuteriohydrate in real time. Xenon-129 NMR spectra of the type I xenon clathrate deuteriohydrate

demonstrated a temperature-dependent line shape from xenon-occupied large cages that reflects the changes in the disorder of D₂O molecules comprising the cavity.

SEOP enhanced ¹²⁹Xe NMR was also applied to the study of the mixed SF₆/Xe and the acetone-*d*₆/Xe type II deuteriohydrates, which were formed at 223 K. Spin-polarized ¹²⁹Xe gas was reacted with a preformed type II structure to prepare the mixed clathrate deuteriohydrates. Fluorine-19 NMR of both the simple SF₆ and the mixed SF₆/Xe clathrates confirmed the existence of the preformed type II clathrate hydrate structure. Xenon-129 NMR spectra of the mixed deuteriohydrates indicate that xenon is more effectively excluded from the hexakaidecahedral cavities of the acetone-*d*₆/Xe deuteriohydrate than from the analogous cavities of the SF₆/Xe deuteriohydrate. In addition, SEOP ¹²⁹Xe NMR was employed to monitor the time dependence of xenon enclathration into the dodecahedral cavities of the type II structure; analysis of the build-up and decay of the ¹²⁹Xe NMR signals facilitated the determination of relative rates of formation of type II mixed clathrate hydrates.

In a third application of SEOP enhanced ¹²⁹Xe NMR discussed in this thesis, spectra resulting from the exposures of four lyophilized proteins have been examined for evidence of site-specific xenon binding. Metmyoglobin, methemoglobin, hen egg white lysozyme, and soybean lipoxygenase yielded distinctly different NMR line shapes. All of the proteins, except lysozyme, possess paramagnetic iron centers that are expected to rapidly relax ¹²⁹Xe and produce a shift in its resonance. Thermally-polarized ¹²⁹Xe NMR studies of metmyoglobin and lipoxygenase in the solution state reveal temperature dependences of both the chemical shifts and line shapes, which provide information concerning exchange of xenon between adsorption sites and dissolved, unbound xenon.

CHAPTER 1 THESIS OVERVIEW

Historical Perspective

Over the past four decades, research involving the use of alkali metal-noble gas spin-exchange optical pumping has evolved from fundamental studies of the optical pumping and spin exchange processes¹⁻⁷ to routine applications for solving chemical problems. Just over forty years ago, researchers demonstrated the first transfer of the angular momentum of circularly polarized photons to the nuclear spins of a rare gas via spin exchange with optically pumped alkali metal atoms.⁸ It would be thirty years before the enhancement of the nuclear spins of noble gases would first be exploited in NMR, for the purpose of solids characterization.

In parallel to the basic research of optical pumping,⁹⁻¹¹ the high sensitivity of the ^{129}Xe NMR chemical shift to changes in the physical and chemical environment was applied to the investigation of local chemical environments within microporous materials.⁹⁻¹² In the 1980s Fraissard and Ito⁹⁻¹¹ first proposed that ^{129}Xe NMR, using atomic xenon as the molecular probe, could be used to explore the geometries and dimensions of the pores and channels of zeolites and other microporous materials. In addition, the technique has evolved in order to provide characterization of catalytic sites

within the pores and channels of molecular solids of various functionalities.⁹⁻¹⁴ Although this information can be obtained through the use of thermally polarized ^{129}Xe NMR, that technique suffers from both low sensitivity of the ^{129}Xe signal and from long T_1 relaxation times.^{12,17,18} This combination of low signal intensities and long relaxation times limit the applicability of the ^{129}Xe NMR towards the characterization of solid materials. The shortcomings of thermally-polarized technique hinder the ability to monitor the short-term functional changes of the surfaces or structural changes of the host material by the responses of the ^{129}Xe chemical shifts, signal intensities and resonance line shapes.

It would not be until the 1990s that the combination of spin exchange optical pumping (SEOP) enhancement of the ^{129}Xe nuclear spin polarization and the use of atomic xenon as a molecular probe would be demonstrated as a highly sensitive, non-invasive technique for probing the surfaces and interiors of solid materials.¹⁹ The responsiveness of the ^{129}Xe NMR chemical shift and line shape to the dimensions of any molecular cavity or channel has allowed detailed exploration of the structural characteristics of the pores and channels of clathrasils,^{20,21} hydroquinone clathrates,^{22,23} and clathrate hydrates.^{12,13,15,16} The sensitivity of the ^{129}Xe NMR chemical shift is so remarkable, that even with the characteristic line-broadening observed for the static spectra of powdered solids, the resonances corresponding to xenon-occupied small and large cavities of the type I clathrate deuteriohydrate can be completely resolved.^{15,16,24} In 1981, Ripmeester and Davidson²⁴ first demonstrated the ability to distinguish the

resonances for the small and large cage guests of the type I xenon clathrate deuteriohydrate by thermally polarized ^{129}Xe NMR.

The xenon clathrate deuteriohydrate may be formed for ^{129}Xe NMR studies to reduce line broadening of the ^{129}Xe NMR resonances due to dipole-dipole interactions between the xenon atom and the protons of a clathrate hydrate lattice.²⁴ Significantly longer relaxation times, however, are observed for xenon enclathrated into the deuteriohydrates, impeding rapid acquisitions of ^{129}Xe NMR spectra. For example, the ^{129}Xe NMR spectrum prepared by Ripmeester and Davidson²⁴ required more than five hours to obtain spectra signal averaged over 24 FIDs. Since the formation of the xenon clathrate hydrate on the surfaces of ice crystals has been shown to proceed to completion on the timescale of minutes, and not hours, monitoring the formation by thermally polarized ^{129}Xe as the reaction proceeds is not possible.²⁵

In 1991, Raftery and co-workers¹⁹ reported the first attempt to overcome the low sensitivity of the conventional ^{129}Xe NMR experiment in a surface absorption study by using alkali metal-rare gas SEOP of the ^{129}Xe nuclei. Thus, in a single-pulse NMR experiment Raftery¹⁹ was able to acquire a ^{129}Xe NMR spectrum following the exposure of powdered benzantracene to spin-polarized xenon gas. Because of the four to five orders of magnitude enhancement of the ^{129}Xe NMR signal, and the use of small tip angles, multiple spectra could be acquired with a single spin polarized ^{129}Xe sample. Raftery's experiment showed that the investigation by ^{129}Xe NMR was no longer limited by low sensitivity of the NMR signal or by long relaxation times. With a single batch of spin-polarized ^{129}Xe , the investigator can now conduct time-resolved experiments having

short recycle delays, including those necessary for monitoring the formation of the type I xenon clathrate hydrate on the surfaces of ice crystals. Since ^{129}Xe NMR provides the ability to resolve individual cavity occupancies, this technique makes possible observation of the rates of formation of each cage type (5^{12} , $5^{12}6^2$ or $5^{12}6^4$) in real time, independently.^{12,16,22,24}

The solubility of xenon in plasma alone²⁶ could not explain the quantities of xenon that could be transported by whole blood, suggesting that xenon must bind directly to the components within the whole blood (presumably to myoglobin and hemoglobin molecules).²⁶ Once it was shown conclusively that xenon binds specifically to myoglobin, hemoglobin, and a variety of other proteins, it became common practice to use xenon-bound protein derivatives for phase determination in X-ray diffraction structure determinations.²⁶⁻²⁸ Since it has been suggested that the motions of the protein control the characteristics of xenon binding, it might also be possible to use bound xenon as a probe for studying protein dynamics.²⁸ Xenon-129 NMR spectra resulting from the adsorption of SEOP enhanced ^{129}Xe by the binding sites should, therefore, be a viable method for obtaining information about both specific and nonspecific binding interactions. Information about xenon-protein binding may also be obtained through the intensification of surface spins of the protein, or other nanocrystalline materials, using polarization transfer from adsorbed spin-polarized ^{129}Xe to surface nuclei.¹³

Dissertation Overview

Chapter 2 begins with a discussion of the general characteristics of ^{129}Xe NMR will be provided. Particular attention will be paid to the factors that directly pertain to the interactions of xenon with surfaces, and confined in the cavities and channels of microporous solids. The procedure for, and characteristics of, the Rb-Xe spin exchange enhancement of the ^{129}Xe nuclear polarization following the optical pumping of rubidium vapors is provided in Chapter 3. There have been recent advances in the use of nuclear spin-polarized ^{129}Xe NMR for exploring the surface characteristics and interiors of molecular solids, with particular interest in the consequences of cross relaxation from ^{129}Xe to surface nuclei. Chapter 4 presents a series of brief synopses of recent applications of SEOP enhanced ^{129}Xe NMR. Attention turns to clathrate hydrates starting with Chapter 5, where the general structural and thermodynamic characteristics are provided.

Mechanisms expressing the kinetics of the formation of simple type I clathrate hydrates are presented in Chapter 6. The relationships of these mechanisms to the time-resolved ^{129}Xe NMR data are presented in Chapter 7. Other studies have presented similar data for type I^{26,29} and type II^{30,31} xenon clathrate hydrates. Chapter 8 examines the use of spin-polarized ^{129}Xe for monitoring the enclathration of xenon into a preformed type II structure. Type II clathrate hydrate experiments provide insights into the rates of enclathration, and also into the disorder of host lattice water molecules as a function of the large cavity occupant. Chapter 9 deals with the application of SEOP

enhanced and thermally-polarized ^{129}Xe to the adsorption of xenon to four different proteins in their lyophilized and solution states. The ^{129}Xe NMR spectra provide information about both site-specific and nonspecific interactions of xenon with the proteins.

The appendices provide additional information on the development of the optical pumping spin exchange setups used for the experiments presented in this dissertation, as well the experimental procedures which were employed (Appendix I). A walkthrough of the calculation of the enhancement factor, and of the nuclear spin polarization, is included in Appendix II. Finally, the apparatus designed for measuring the pressure-time dependence during the formation of the simple type I xenon clathrate hydrate is available in Appendix III.

CHAPTER 2

CHARACTERIZATION OF MICROPOROUS MATERIALS WITH ^{129}Xe NMR

Introduction

Although ^{129}Xe and ^{13}C have similar gyromagnetic ratios (7.45 and $6.72 \times 10^7 \text{ rad T}^{-1} \text{ s}^{-1}$ for ^{129}Xe and ^{13}C , respectively), the ^{129}Xe NMR receptivity is 32.6 times higher than that of ^{13}C NMR.^{12,16,17,32} (The relative receptivity is the product of the NMR signal sensitivity and the natural abundance, each as compared to that of the reference nucleus, ^{13}C .) In practical terms, this greater receptivity means that a ^{129}Xe NMR resonance can be detected with a thermally equilibrated xenon gas sample at pressures of one atmosphere or slightly greater in a single FID acquisition at high magnetic fields (9.4 T, for example). In addition, the atomic polarizability of xenon makes it highly soluble in a wide range of solvents. Thus, the ^{129}Xe NMR resonance can also be observed easily for xenon gas dissolved in a variety of solvents. In fact, the solubility of xenon in most solvents can be up to two orders of magnitude higher than for other nonpolar gaseous molecules. Still, the high solubility does not guarantee sufficient signal intensity through acquisition of a single FID. In such cases, signal averaging over multiple FIDs can overcome this

problem. Long spin-lattice relaxation times for the spin $\frac{1}{2}$ isotope, however, can make this an unfeasible solution for experiments where short acquisition times are desired.

While quadrupolar mechanisms usually dominate in the spin lattice relaxation of ^{131}Xe , relaxation of ^{129}Xe may be dominated by mechanisms involving chemical shielding, spin-rotation or dipolar interactions.^{12,17,18} Thus, thermally-polarized ^{129}Xe NMR frequently suffers from long T_1 relaxation times.^{12,17} For xenon trapped in solid matrices, such as clathrates, relaxation times exceeding 20 minutes can be observed.¹⁶ Even when dissolved in protonated and polar solvents, the ^{129}Xe T_1 can be from tens of seconds to several hundred seconds.^{16,33} For example, the T_1 for ^{129}Xe dissolved in benzene has been reported to be 270 s, while in the fully deuterated benzene, it is 570 s.³³ Of course, the long spin relaxation times necessitate lengthy recycle delays, so that signal averaging can typically be performed only over small numbers of FID acquisitions. This fact eliminates the ability to monitor short-term changes in the ^{129}Xe signal intensity and line shape, as is required for chemical kinetics studies.

Applications of ^{129}Xe NMR to the Study of Microporous Materials

The use of atomic, gaseous xenon combined with ^{129}Xe NMR has advanced greatly in the past two decades as a means by which to investigate local chemical environments within microporous materials.⁹⁻¹⁵ In the 1980s, Fraissard and Ito⁹⁻¹¹ proposed that ^{129}Xe NMR of xenon gas adsorbed onto zeolite surfaces could be used to derive information concerning the pore and channel dimensions and to characterize the

hydrophilic and acidic nature of the pore surfaces. Their results prompted others to explore the use of ^{129}Xe NMR for studying the adsorption of gases into a wider variety of microporous materials. For example, Ripmeester *et al.*¹⁶ investigated the NMR characteristics of xenon trapped in various clathrates in an attempt to determine the factors directly influencing the shielding and relaxation of adsorbed xenon.

The sections that follow review some of the factors governing the value of the chemical shift of ^{129}Xe adsorbed or occluded into mesoporous and microporous materials. As was mentioned in Chapter 1, ^{129}Xe NMR chemical shift observed for atomic xenon is extraordinarily sensitive to the chemical and physical surroundings.^{12,16,34} The magnetic shielding of the ^{129}Xe nucleus can be written as the sum of several independent factors, represented in equation 2-1,^{34,35}

$$\sigma = \sigma_0 + \sigma_b + \sigma_a + \sigma_w + \sigma_{E1} + \sigma_{E2} + \sigma_{rep}, \quad (2-1)$$

where σ_0 is related to the shielding in the free atom. The term σ_b arises from the bulk susceptibility, and σ_a from the magnetic anisotropy of the neighboring molecules. A term that will become important when discussing the dependence of the chemical shift of adsorbed or enclathrated xenon on the pore diameter of a cavity is σ_w , which results from intermolecular van der Waals interactions with molecules of the solvent or with a solid substrate; σ_{rep} represents the repulsive part of the van der Waals interaction. Finally, σ_{E1} originates from the reaction field induced in the solvent by the permanent electric dipole of the solute, and σ_{E2} is the shielding contribution caused by the permanent electric dipole

of the solvent.^{17,18} Depending on the experimental conditions, different terms of equation 2-1 will dominate the effective shielding. For example, the ^{129}Xe NMR chemical shifts for xenon dissolved in nonpolar and magnetically isotropic solvents are highly dependent on the van der Waals term, thus making $\sigma_w \gg \sigma_{E1}$ or σ_{E2} . Conditions may be reversed when considering solvents of molecules with large permanent dipoles where the σ_{E2} term becomes significant.¹⁸ In the discussions that follow addressing chemical shifts for enclathrated gaseous xenon, the expression for σ will be simplified to those terms that relate the chemical shift to the properties of the pore and its surface properties. Although the effects of sample bulk susceptibility cannot be neglected in any detailed consideration of ^{129}Xe NMR of microporous materials, this discussion will focus on the sensitivity of the ^{129}Xe NMR chemical shift to the dimensions of the pore. Addressing the contributions to the shielding from van der Waals interactions with the host lattice will be important to the discussion of ^{129}Xe NMR of xenon enclathrated in to the clathrate hydrate structure.

Estimation of Pore Dimensions and the Determination of Cavity Symmetry

The magnetic shielding of xenon's highly polarizable electronic state has two contributions, a diamagnetic term and a paramagnetic term.¹² The diamagnetic term is dominated by contributions from the core electrons, and therefore is insensitive to changes of the external environment.^{12,16} The paramagnetic term, however, is associated with excitations of the *valence* electrons into higher energy levels, excitations that can be induced, for example, by the presence of applied magnetic fields.¹⁶ Therefore, the

paramagnetic term is primarily responsible for the sensitivity of the ^{129}Xe NMR chemical shift to the physical environment.

Several hypotheses have been proposed to explain the sensitivity of the ^{129}Xe NMR chemical shift to the dimensions of the pores.¹⁶ The interaction of the xenon atom with the walls of the cavity distorts the overall shape of xenon's electron cloud, and thereby alters the paramagnetic contribution to the magnetic shielding.^{12,16} Distortion of the electron cloud about the xenon nucleus produces a downfield shift of the ^{129}Xe resonance with respect to that of xenon in its free, gaseous state. The magnitude of the paramagnetic van der Waals term in equation 2-1 results from (1) the intrinsic polarizability of the guest molecule with respect to the nature of the host molecules and (2) the extrinsic curvature effects of the pore surface in association with the cavity dimensions. When studying analogous series of clathrate hydrates, where the chemical characteristics of the $(\text{H}_2\text{O})_n$ lattice are nearly the same, the intrinsic polarizability of the enclathrated xenon can be neglected in order to compare the effects of the cavity dimensions on the observed ^{129}Xe NMR chemical shift and line shape. Consider the relationship of the van der Waals interactions to the dimensions of the clathrate cavity. For a spherical cavity, the van der Waals interaction energy, W , due to the interaction between the guest and surrounding host molecules is given by equation 2-2,^{36,37}

$$W = -\left(\frac{C}{4d^3}\right)\left(1 - \frac{d}{2a}\right)^{-3} \quad (2-2)$$

where C is a molecular constant specific to the guest and the host lattice, d is the distance from the average position of the guest to the pore wall, and a is the pore radius. For a cylindrically shaped pore, equation 4-2 can be modified by substituting for the value of a an effective pore radius, $(3/2)^{1/3} r$, where r is the van der Waals crystallographic radius of curvature of the pore. Changes in the chemical shift, δ_W , will be directly proportional to the changes in the van der Waals interaction energy, W , by equation 2-3,³⁶

$$\delta_W = A \cdot W, \quad (2-3)$$

where A is a constant intrinsic to the observed nucleus. Where the dimensions of the cavity approach those of the guest molecule, the guest and host lattice are in constant contact. Thus, the smaller the cavity, the more effective is the perturbation of the electron distribution of the guest molecule.

For a pore size large enough to allow some amount of translational motion of the guest, the magnitude of the van der Waals interaction energy, and thus the magnitude of δ_S , is directly proportional to the duration of the time spent in "contact" with the surface of the cage. As a result, δ_W is directly proportional to the frequency of collisions between xenon and the atoms forming the cage.^{16,38} At constant temperature, the frequency of collisions of xenon with the host lattice is inversely proportional to the mean free path of xenon in the cavity. The mean free path is defined as the average distance traveled by a xenon atom between two successive collisions against the cavity walls.³⁸ When the surface chemical characteristics of the host lattice can be neglected, the relationship of

mean free path to the isotropic chemical shift of ^{129}Xe has proven to be linear, with a slope of $-5.147 \times 10^{-3} \text{ \AA ppm}^{-1}$.¹⁶ To date, attempts to explain the theoretical foundation for this linear relationship based on the combinations of simple binary interactions of the guest and host molecules have proven unsuccessful.¹⁶ A detailed analysis of the relationship, however, is beyond the scope of this introduction.

Clathrates are highly crystalline solids that provide well-defined cavities and surfaces with which to study the effects of enclathration on guest species. Because the guest molecules typically experience only weak interactions with the molecules of the host lattice, clathrates are the most appropriate materials with which to study the chemical shift-pore geometry relationship. Other materials, such as zeolites, might also provide uniform structures, however, but the situation is complicated by the presence of interconnected channels and pores, and their internal surfaces are not as well-characterized as those of hydrate clathrates, making them less than ideal for exploring the relationship of the ^{129}Xe NMR chemical shift to average cavity diameter. Xenon-129 NMR studies of Xe trapped in clathrasils,^{20,21} hydroquinone clathrates,^{22,23} and clathrate hydrates^{12,15,16} have demonstrated a direct correlation not only of the chemical shift to the average diameter of the cage, but, as will be discussed, have also been able to provide information concerning the actual shape of the cage.^{12,16}

Isotropic and Anisotropic ^{129}Xe NMR Line Shapes for Xenon Inclusion Compounds

As mentioned earlier in this chapter, the chemical shift of enclathrated ^{129}Xe with respect to that of the dilute gas sample is directly proportional to the frequency of the

collisions of xenon with the walls of the cavity.¹⁶ As the average radius of the cavity is decreased, the isotropic chemical shift migrates further downfield with respect to that of the dilute gas. Only for cavities of cubic symmetry, where the mobility of the guest atom is the same in all directions, are simple isotropic ^{129}Xe NMR chemical shifts observed. For xenon enclathrated into cavities sharing other symmetries, varying degrees of anisotropy and NMR line shape asymmetry are observed.¹⁶

While the isotropic value of the ^{129}Xe NMR signal is sensitive to the mean free diameter of the cavity, the NMR line shape is sensitive to the geometry and symmetry of the host structure. The ^{129}Xe NMR chemical shift tensor has been found to be axially symmetric for cavities possessing one unique axis of rotation, as is the case with oblate and prolate cavities.¹⁶ The ^{129}Xe NMR line shape for xenon enclathrated into an oblate cavity shows a clearly axially symmetric tensor with a positive anisotropy.¹⁶ Similarly, the ^{129}Xe NMR line shape for prolate cavities exhibits a negative anisotropy. The observed correlation of the anisotropy to the cavity geometry can be explained as an average tensor arising from motion of the xenon atom over the surface of cavity. For a xenon atom occupying a cavity of non-cubic symmetry, the equilibrium position of the xenon atom should not be depicted as a static placement at the center of the cage, but rather as the position averaged over the motion of xenon along the cavity surface.¹⁶ This model has been confirmed experimentally for diatomic molecules, such as nitrogen enclathrated in the type II clathrate hydrate and is supported by both molecular dynamic calculations and vibrational spectra.³⁹ Calculations comparing the hard-sphere contacts between xenon and the host molecules suggest that there is sufficient void space in the

cages of clathrate hydrates for the position of the xenon atom to oscillate.¹⁶ In addition, Lennard-Jones potential calculations performed for enclathrated xenon have demonstrated (1) that the position of minimum potential is not at the center of the cage for tetrakaidecahedral and hexakaidecahedral cavities, and (2) that for dodecahedral cavities, where the minimum is indeed at the center, displacements from the center position produce only small increases in the potential energy.¹⁶

For xenon an enclathrated xenon atom, it is assumed that its equilibrium position is actually averaged over the motion of the guest atom across the internal cavity surface. The location of the xenon atom at any given time is somewhere on the inner surface of the cavity with the σ_{zz} component normal to the surface of the cavity. The chemical-shift tensor for xenon at that position will be axial and will have specific anisotropy. The averaged tensor component, σ'_{zz} , will therefore be oriented along the unique symmetry axis of the cage. Thus, for xenon at a given position on the surface of the cavity there will be a non-zero static anisotropy, $\Delta\sigma$, and an angle β between the tensor axes σ_{zz} and σ'_{zz} .¹⁶ For all locations of the xenon atom where σ_{zz} makes the angle β with σ'_{zz} , there is a average anisotropy, $\Delta\sigma_{av}$, given by equation 2-6,^{16,40}

$$\Delta\sigma_{av} = \frac{\Delta\sigma}{2} (3 \cos^2 \beta - 1). \quad (2-6)$$

For an enclathrated xenon atom, the population weighted average, $\Delta\sigma'_{av}$, over all values of β for the given cavity type is given by equation 2-7,

$$\Delta\sigma'_{av} = \frac{\Delta\sigma}{2} \left(\frac{\sum_i (3\cos^2\beta_i - 1)W_i}{\sum_i W_i} \right), \quad (2-7)$$

where W_i is the population for β_i . A simple approximation for W_i is to equate it to the surface area for the element with β_i .¹⁶ Application of equation 2-7 is trivial when discussing cavities having cubic symmetries; in such cases, the anisotropies would average to zero. If a cavity is stretched along the principal axis, thus changing the populations W_i in such a manner as to prevent averaging to zero, and a negative anisotropy will result; when compressed along the same axis, the anisotropy values will again average to a nonzero value, resulting in a positive anisotropy.

¹²⁹Xe NMR Characteristics of Xenon Clathrate Hydrates

In many cases, the NMR resonances for xenon enclathrated in the small and large cavities can be completely resolved.^{15,16,24} Such well-resolved signals are readily integrated, and provide a quantitative determination of the amount of xenon enclathrated into each type of cavity of the hydrate. Ripmeester and Davidson²⁴ first demonstrated the ability to distinguish the resonances for the small and large cage guests of the type I xenon clathrate hydrate by thermally polarized ¹²⁹Xe NMR. The static spectrum has been provided in **Figure 2-1**. For these experiments, the clathrate *deuteriohydrate* was studied

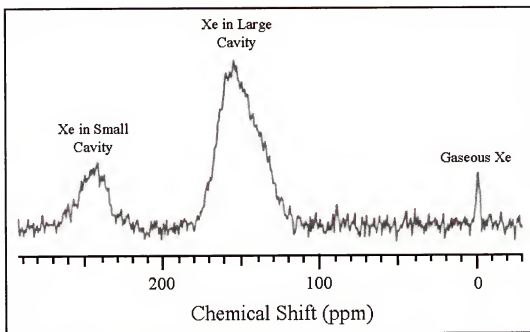


Figure 2-1. The thermally polarized ^{129}Xe NMR spectrum of the type I simple xenon clathrate deuteriohydrate is shown. The spectrum was acquired with 24 scans, and a recycle delay of 800 s. Adapted with permission from reference 24.

because the broadening effects caused by the dipole-dipole interactions of the guest with the of hydrate lattice protons is reduced. In the static ^{129}Xe NMR spectrum of the xenon type I clathrate hydrate, the ^{129}Xe NMR resonances are not resolved.

Long spin-lattice relaxation times for thermally polarized ^{129}Xe make monitoring progress of gas clathrate hydrate formations in supercooled water samples difficult,¹⁶ and on the surfaces of ice crystals (which display much more rapid rates of formation²⁵) all but impossible. The recycle delays necessary to obtain the ^{129}Xe NMR spectrum prepared by Ripmeester and Davidson²⁴ required more than five hours to obtain spectra signal averaged over 24 FIDs. The formation of the xenon clathrate hydrate on the surfaces of ice crystals, however, is known to proceed to completion on the timescale of minutes for

temperatures above ~200 K.²⁵ On this timescale, the ^{129}Xe NMR relaxation time would hinder attempts to monitor the formation in real time by thermally-polarized NMR techniques.

Chapter 3 will discuss the preparation and application of SEOP enhanced ^{129}Xe NMR for experiments where the spin lattice relaxation time and the duration of the reaction occur on similar timescales. With an enhancement of ^{129}Xe NMR signal by several orders of magnitude, there is no need for the signal averaging of large numbers of FIDs in to achieve sufficient signal:noise. Thus, SEOP enhanced ^{129}Xe NMR can be used to monitor the formation of the type I clathrate hydrate following the exposure of ice crystals to xenon gas in real time. Since ^{129}Xe NMR provides the ability to determine individual cavity occupancies for the xenon-occupied small and large cavities, this technique makes it possible to extract the rates of formation of each cage type (5^{12} , $5^{12}6^2$ or $5^{12}6^4$) independently.^{12,16,22,24,25}

^{129}Xe NMR Line Shapes for Occupied Small and Large Cavities of Clathrate Hydrates

In either the type I or the type II hydrate structure, there are only two types of cavities, and, therefore, there are only two discrete chemical environments experienced by enclathrated xenon atoms. Clathrate hydrate guest molecules are completely magnetically isolated from one another. Therefore, these systems are ideal with which to test the relationship between the observed ^{129}Xe NMR resonance and dimensions of the pore.⁴¹ For modeling purposes, the mean free path of the cavity depends on the

Table 2-1. Summary of Typical ^{129}Xe NMR Parameters for the Type I And Type II Gas Clathrate Hydrates.^{16,42}

Structure	Cage Type	Symmetry	$r_m / \text{\AA}$	σ_{Xe} (iso) (ppm)	$\Delta\sigma_{\text{Xe}}$ (ppm)
hydrate type I	5^{12}	$m\bar{3}$	2.50	-242	0
hydrate type I	$5^{12}6^2$	$42m$	2.93	-152	32
hydrate type II	5^{12}	$3m$	2.50	-225	18
hydrate type II	$5^{12}6^4$	$43m$	3.28	-80	0

orientation of each water molecule, and therefore, a proper model for the system cannot be constructed simply by specifying the locations of the oxygen atoms.¹²

Dodecahedral cavities are common to both the type I and type II structures. For the type I xenon hydrate structure, the 5^{12} cavities possess $m\bar{3}$ symmetry.^{12,43} **Table 2-1** provides a summary of symmetries of the cavities present in the hydrate structures I and II. The observed ^{129}Xe NMR line shapes correspond well to the isotropic signals expected for xenon in cavities of cubic symmetry.^{16,44} In the static spectrum of the $(\text{H}_2\text{O})_n$ hydrate, the NMR line shape for xenon-occupied dodecahedral cavities is broad, making it difficult to correlate the resonance line shape to cubic symmetry. It is, however, more clearly apparent in the more narrow line shapes observed in the ^1H decoupled ^{129}Xe NMR spectra, such as those presented by Davidson and Ripmeester,²² or in the spectra of the deuteriohydrate, where line broadening due to dipolar interactions are reduced. The larger cavities of the type I clathrate hydrate structure are the tetrakaidecahedral cavities. The two additional hexagonal faces of the tetrakaidecahedron are arranged opposite each other, forming a cage with oblate geometry. Motion along one of the axes is restricted so

that a positive chemical shift anisotropy is expected, and as a result, a $\Delta\sigma$ value of 32 ppm is observed.^{16,42}

The hexakaidecahedral cavity of type II clathrate hydrates, which is larger than the tetrakaidecahedral cavity, will accommodate significantly larger molecules. The four hexagonal faces of the hexakaidecahedral cavity of type II clathrate hydrates are arranged in such a manner that small guest molecules, like xenon, exhibit motion not unlike what they would experience in a cavity of true cubic symmetry. To accommodate the larger hexakaidecahedral cages in the unit cell, dodecahedral cavities are slightly distorted from their cubic symmetry. Xenon atoms enclathrated inside these smaller cavities exhibit anisotropic ^{129}Xe NMR line shapes, where the magnitude of the anisotropic shift is dependent on the actual size and shape of the large cavity guest. This characteristic of the ^{129}Xe NMR line shape will be demonstrated and discussed in more detail in Chapter 8. The expected characteristics of the ^{129}Xe NMR spectra for xenon enclathrated into the structure I and structure II hydrates are also provided in **Table 2-1**. Since xenon enclathrated inside hexakaidecahedral cavities has a greater range of motion, which is nearly isotropic, an observed isotropic NMR signal with a Gaussian line shape is observed, shifted upfield from the ^{129}Xe NMR signal for xenon enclathrated into dodecahedral cavities.

Summary

The use of ^{129}Xe NMR, with gaseous atomic xenon as the molecular probe, has become a popular technique for the investigation of local chemical environments within microporous materials. Although ^{129}Xe NMR is useful for studying the pore and surface properties of a variety of crystalline microporous materials, many of these substances have surface polarities and acidities that are as yet not well characterized. Zeolites are a class of microporous material which providing highly crystalline networks of pores of various sizes, but their pore and channel surfaces can vary in acidity and catalytic properties. Clathrate hydrates, on the other hand, are highly crystalline solids that provide well-characterized, well-defined cavities and surfaces. Thus, hydrate inclusion compounds are perhaps the most appropriate materials with which one can study the relationship between the ^{129}Xe NMR parameters and the pore dimensions. The high polarizability of xenon allows the ^{129}Xe NMR resonances corresponding to occupied dodecahedral, tetrakaidecahedral, and hexakaidecahedral cavities to be well resolved, even in the static spectrum. In the succeeding chapters, this study will demonstrate how SEOP ^{129}Xe NMR can be used to monitor the rates of xenon enclathration for each cavity type independently, and in real time.

CHAPTER 3

INTRODUCTION TO THE SPIN EXCHANGE OPTICAL PUMPING (SEOP) ENHANCEMENT OF THE ^{129}Xe NMR SIGNAL

Introduction

Chapter 2 introduced the two naturally occurring isotopes of xenon that exhibit nuclear spin, ^{129}Xe and ^{131}Xe , and it also addressed the high sensitivity of the ^{129}Xe and ^{131}Xe NMR chemical shifts to the chemical or physical environment.^{14,16,34} It has been shown that xenon in the solid state exhibits a shift of about 300 ppm from that of xenon in its gaseous state,¹⁴ and that xenon adsorbed or occluded in porous materials exhibits a chemical shift up to several hundred ppm downfield with respect to that of the dilute gas. Specifically, it is known that ^{129}Xe trapped or occluded into the void spaces of microporous materials,^{16-18,38,45} exhibits chemical shift (downfield from that of the free gas) that is proportional to the mean free diameter of the pores.^{16,38} This chemical shift-pore dimension relationship will be discussed in more detail in how it relates to the ^{129}Xe NMR studies of the simple and mixed xenon clathrate hydrates.

The ^{129}Xe NMR receptivity is 32.6 times higher than that of ^{13}C NMR, adding to the advantages of using atomic xenon over organic compounds as a molecular probe of local environments within microporous materials.^{12,16,17,46} In many applications, signal

averaging over multiple FIDs is necessary to overcome low signal intensities. The applicability of thermally polarized ^{129}Xe NMR to real time measurements in kinetics experiments, then, can be limited due to the long T_1 relaxation times that are commonly encountered.^{12,17,18} To counter the long relaxation times and relatively low receptivity in the conventional ^{129}Xe NMR experiment, techniques have been developed to enhance the ^{129}Xe nuclear spin polarization many times that observed at thermal equilibrium.

Non-Equilibrium Techniques for Enhancement of the ^{129}Xe NMR Signal

Figure 3-1 suggests how an enhancement of the NMR signal by several orders of magnitude can be used for real-time kinetics experiments. The use of small tip angles prevents rapid depletion of the magnetization reservoir, and allows a number of spectra to be acquired using a single batch of nuclear spin polarization enhanced xenon gas. The ^{129}Xe nuclear spin polarization of nuclear spins has been amplified through two non-equilibrium techniques, Hartmann-Hahn cross polarization (CP)¹⁶ and spin exchange optical pumping (SEOP) with alkali metal vapor.⁷

Hartmann-Hahn Cross Polarization

In general, cross polarization (CP) techniques are used to enhance the sensitivity of the solid-state NMR experiment, so that less signal averaging is necessary, and thus, acquisition time decreases. Hartmann-Hahn cross polarization (HH-CP) is a technique by which nuclear spin polarization can be transferred between two different groups of spins,

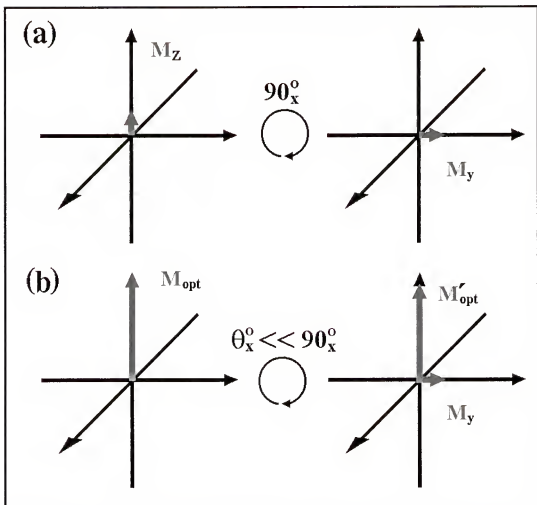


Figure 3-1. Enhancement of nuclear magnetization, M_z , may be accomplished through non-equilibrium techniques. (a) With magnetization resulting only through thermal equilibrium conditions, the maximum signal intensity that can be acquired results through application of a full 90° tip-angle pulse. In the case of ^{129}Xe , the time required to re-achieve thermal equilibrium is quite long, which can limit the number of scans possible for signal averaging. (b) Signal enhancement techniques such as alkali metal-noble gas SEOP increase the magnetization by several orders of magnitude, so that the same signal intensity (or greater) may be achieved with a smaller tip angle which does not deplete significantly the polarization reservoir.

I and S , through dipolar coupling. The direction of flow of nuclear spin polarization in HH-CP is dictated by the spin temperatures of I and S . The most abundant spins are

represented as the *I*-spin reservoir. The Curie Law specifies that the magnetization, M_0 (specified in amperes/meter), is related to the applied magnetic field, B_0 , provided in Tesla (or Gauss) and the absolute temperature, T (in Kelvin), by the relationship

$$M_0 = \frac{CB_0}{T}, \quad (3-1)$$

where C is a constant specific to a given type of spin. The abundant spins, I , are referred to as the spins of the *cold* reservoir. In cases of *I-S* pairs where I refers to ^1H spins and S refers to either ^{13}C or ^{129}Xe spins, HH-CP can enhance the NMR signal intensities by up to a factor of about four, which represents a potential 16-fold savings in time for signal-averaged experiments. Additionally, the I spins (e.g. ^1H) typically relax more rapidly than the S spins (e.g. ^{13}C or ^{129}Xe), so that CP signal enhancement can be repeated at a much faster rate than for the thermal equilibrium experiment.

The transfer of nuclear spin polarization from the cold I spins to the hot S spins requires that the spins have identical Larmor frequencies, which is accomplished in the doubly rotating frame. The HH-CP pulse sequence that brings the two reservoirs of the I and S spins into thermal contact is illustrated in **Figure 3-2**. The I spins are rotated to the y -axis by the application of a 90_x pulse and are then spin-locked along the y -axis by constant rf irradiation. The I spins are locked along the y -axis for a period of about 1–5 ms. As the I spins are locked along the y -axis, a second rf field is applied at the resonance frequency of the S spins. During the contact time, both the I and S magnetization vectors are effectively prevented from precessing in their respective rotating frames. Under these

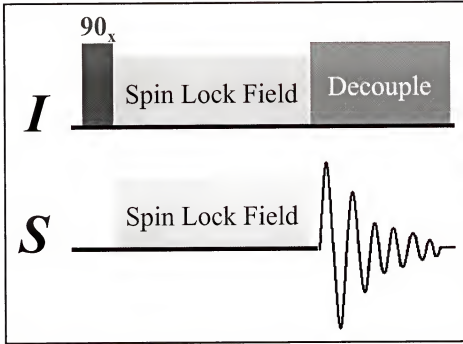


Figure 3-2. The Hartmann-Hahn cross polarization pulse sequence brings the two reservoirs of the I and S spins into thermal contact. The I spins are tipped along the y -axis by application of a 90_x pulse. These spins are spin-locked along the y -axis for a period of about 1–5 ms. A second rf pulse application, simultaneous with the I spin locking irradiation is applied at the resonance frequency of the S spins. During the resulting contact time, nuclear spin polarization is transferred from the ample I spins to the more rare S spins.

conditions, the dipolar coupling provides an efficient energy transfer mechanism, and net transfer of polarization from the I spin reservoir to the S spin reservoir occurs. This is called the Hartmann–Hahn matching condition, expressed as equation 3-2,

$$\gamma_I B_I = \gamma_S B_S, \quad (3-2)$$

where B_I and B_S are the spin locking fields for the I and S spins, respectively. The matching condition is typically achieved by adjusting the strength of the two spin locking

fields. As the spin temperatures equilibrate, the S spin magnetization grows in along the x -axis, while the I spin magnetization decreases. After the contact time, the S spin rf field is discontinued and the FID is acquired. The I spin rf field is applied throughout the acquisition in order to decouple the I and S spins.

To address the problem of the long spin-lattice relaxation times observed for ^{129}Xe , ^1H - ^{129}Xe Hartman-Hahn cross polarization with proton decoupling has been applied to studies of xenon clathrate hydrates.^{12,47} The magnetization observed for ^{129}Xe is derived from the magnetization of neighboring protons with an appreciable dipolar interaction with the ^{129}Xe atom, and, therefore, HH-CP provides an effective means of discriminating against bulk solid or liquid xenon signal. As mentioned previously, signal enhancements achieved through HH-CP are typically less than a factor of ten. Signal averaging for acquiring ^{129}Xe NMR spectra of the xenon clathrate hydrates must still be employed, making NMR acquisition times too long to permit time-resolved ^{129}Xe NMR measurements on the timescales on which the type I xenon clathrate hydrate forms on the surfaces of ice particles. In addition, the signal integrals depend on the CP dynamics and factors such as motion, spin diffusion, the number of neighboring protons and the magnitude of the dipolar couplings of the protons to the guest and to other protons of the host lattice.⁴⁸ Thus, the CP method does not necessarily yield accurate spin counting.

Alkali Metal-Noble Gas Spin Exchange Optical Pumping

The NMR signal intensities of noble gases such as ^3He or ^{129}Xe can be enhanced by three to four orders of magnitude, as compared to the thermal equilibrium values,

using alkali metal-rare gas spin exchange optical pumping (SEOP). There are two general steps to achieving signal enhancement in this manner. First, the alkali metal atom vapor must be optically pumped through an electronic excitation, for example at the D_1 or D_2 line of rubidium, with circularly polarized light. In the second step, the angular momentum of the electron of the alkali metal atom is transferred directly to the nucleus of the noble gas atom. Over the past two decades, SEOP techniques have evolved, providing more efficient polarization, transport, and storage of spin polarized gases.⁷

Optical Pumping of Rubidium Metal Vapor

The processes of spin exchange optical pumping have been studied and reviewed by many researchers.¹⁻⁷ In this section a brief, qualitative description of the spin exchange optical pumping process will be presented in order to provide the essential information necessary to understand SEOP enhancement of noble gas nuclear magnetization. In principle, any alkali metal can be used for enhancement of the nuclear spin polarization of noble gases through SEOP. Higher efficiencies of SEOP have been observed for some of the alkali metals, cesium in particular,⁴⁹ but the commercial availability of intense, tunable light sources (Titanium-Sapphire, dye, and diode lasers) at the wavelengths of the rubidium electronic transitions (D_1 line, 794.7 nm, in particular) is the primary reason for the more common use of rubidium.^{7,49,50} The low melting point and high vapor pressure of rubidium are also additional advantages; a rubidium vapor sample with an optical density close to unity can be produced at mild temperatures where the alkali metal will not attack the siloxane surface coating typically used to coat the borosilicate optical pumping cell or

the borosilicate glass surface itself.^{7,49} Rubidium has two naturally occurring isotopes, ⁸⁷Rb ($I = 5/2$ and a natural abundance of 72.2 %) and ⁸⁵Rb ($I = 3/2$ and natural abundance 27.8 %), either of which may be used in the SEOP experiment. For simplicity, the discussion that follows will refer specifically to processes involving ⁸⁷Rb.

In the typical optical pumping setup, several small droplets of the metal are added to the pumping cell and heated to a temperature of 80-150 °C (depending on the type of laser and the total pumping cell gas pressures being used), yielding a rubidium atom density of 10^{11} to 10^{14} per cm^3 .^{2,7,50} The rubidium density can be more precisely calculated from the empirical relation given by Killian,²

$$[Rb] = 10^{(10.55 - 4132/T)} / kT, \quad (3-3)$$

where T is the temperature, in Kelvin.

In the presence of a magnetic field B_0 applied along the z -axis of the laboratory-fixed coordinate system, the Hamiltonian representing the spin interactions of the alkali metal atom is given by expression 3-4,

$$H = A\vec{I} \cdot \vec{S} + g_S \mu S_z \cdot B_0 - \frac{\mu}{I_a} I_z \cdot B_0, \quad (3-4)$$

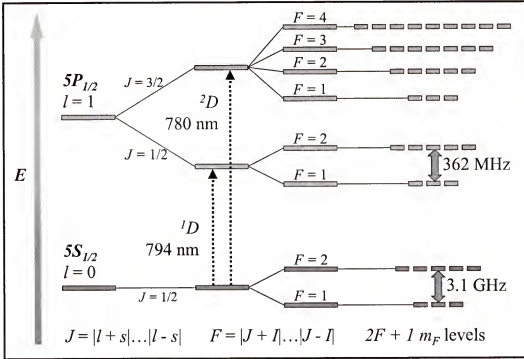


Figure 3-3. Energy Level Diagram for ^{87}Rb . At low pressures of gas in the pumping cell, the hyperfine structure of the ground state is resolved. Shown here are the resolved hyperfine structures for the both the D_1 and D_2 transitions in ^{87}Rb .

where the electron spin is denoted S and the alkali metal nuclear spin is denoted I_a .⁷ The first term represents the hyperfine interaction between the electron and the nucleus of the alkali metal atom, while the remaining two terms describe the interaction of the electron and nuclear moments with the external field. At the comparatively low magnetic fields strengths typically employed in spin exchange optical pumping, the hyperfine interaction dominates over the Zeeman interactions.⁷

The energy level diagram of atomic ^{87}Rb , including spin-orbit coupling and electron-nuclear hyperfine coupling, is shown in **Figure 3-3**. At low buffer and noble gas pressures, the hyperfine structure of the ground state is resolved, and depending on the

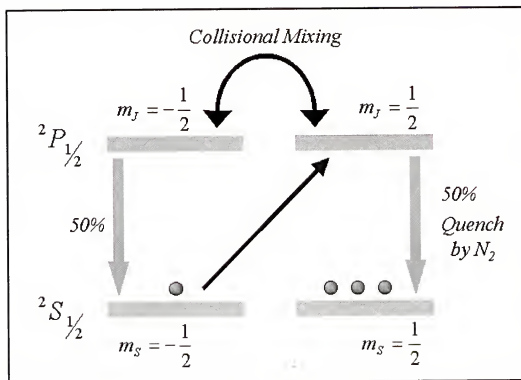


Figure 3-4. The physics of the optical pumping of an alkali metal vapor, where pressure broadening has made the fine structure irresolvable. The interaction of alkali atoms with left circularly ($\sigma+$) polarized light is depicted: (1) Excitation of the $^2S_{1/2}$, $m_s = -1/2$ state by the selection rule $\Delta m = +1$; (2) Collisional mixing equalizes the populations of the $^2P_{1/2}$ excited states; (3) Nitrogen rapidly quenches the excited state atoms, leaving the electronic spin intact.

laser tuning, the optical excitation and population build-up may occur in either the $F = 2$ or the $F = 3$ manifolds. When the pumping cell gas pressure exceeds 100 torr, the two hyperfine levels are no longer optically resolved due to collisional (or pressure) broadening, and the nuclear spin of the alkali atom may be neglected. The discussion of the optical pumping process is thus simplified to a four level system,⁷ as shown in **Figure 3-4**. Optical absorption of a left or right circularly polarized photon at the D_1 transition frequency (1.5 eV or 794.7 nm) imparts angular momentum to the valence electron of a

rubidium metal atom. The D_1 transition refers to the transition from the $^2S_{1/2}$ ground state of the alkali metal atom to the lowest excited $^2P_{1/2}$ state.^{7,51,52} For the excitation of the electron, the selection rule $\Delta m_F = \pm 1$ applies and the value of Δm_F depends solely on the helicity (left, σ^+ , or right, σ^-) of the circularly polarized photon. For example, σ^+ polarized light will excite atoms from the spin down ($m_F = -1/2$) sublevel of the ground state to the spin up ($m_F = +1/2$) sublevel of the excited state.

The spin orientation of the ground state electrons that will be excited is therefore determined by the helicity of the circular polarization of the incident beam. For example, left circularly polarized light (σ^+) excites only atoms from the spin-down sublevel ($m_S = -1/2$) of the $^2S_{1/2}$ state to the spin-up ($m_S = 1/2$) sublevel of the $^2P_{1/2}$ state.⁷ Following the electronic excitation, collisions of the excited alkali metal atoms with the other gas atoms of the pumping cell rapidly equalize the sublevel populations of the excited state. The excited state atoms, of all sublevels, collide with “quenching gas” molecules, typically nitrogen molecules, which serve to relax rubidium atoms back to the $^2S_{1/2}$ ground state with the electronic spin polarization conserved.^{51,52}

Nitrogen at pressures of a few torr to tens of torr is commonly used as the quenching gas because it efficiently relaxes the excited state rubidium atoms back to the ground state by non-radiative pathways. While quenching cross sections for rubidium with the noble gases range from 3.0×10^{-15} to 5.0×10^{-15} cm², the cross section for nitrogen is 10.5×10^{-15} cm², indicating that nitrogen is substantially more efficient for quenching the excited electronic state of rubidium.⁵² Non-radiative quenching of the excited rubidium atoms minimizes the problem of “radiation trapping”, where the

emission of light from excited atoms in all directions is followed by the re-absorption of the photon by other atoms in the vapor.^{7,53} Since the optical polarization of an emitted photon depends on the direction of emission, radiation-trapping can reduce the total accumulated polarization of the alkali metal atom vapor.^{51,53} Multiple emission/re-absorption events can further significantly reduce the rubidium atom polarization.⁷ The duration of the interaction of excited rubidium and nitrogen is short compared to the fine structure period (1.4×10^{-13} s), so that angular momentum imparted through the optical pumping process is preserved.⁵¹⁻⁵³

In practice, experimental conditions (*i.e.*, temperature, total gas pressure, buffer gas composition) are adjusted so that the rates of optical pumping and excited state quenching are high compared to the rate of electron spin relaxation. Assuming a uniform laser profile through the pumping cell, the steady state rubidium polarization, P_{Rb} , is given by equation 3-5,

$$P_{Rb} = \frac{\gamma_{opt}}{\gamma_{opt} + \Gamma_{SD}}, \quad (3-5)$$

where γ_{opt} is the rate of optical pumping, and Γ_{SD} refers to the “spin destruction” rate.^{50,54,55} Within the illuminated region, rubidium polarizations of up to 95% have been observed.^{50,54,56}

In addition to the role it serves as a quenching agent, diatomic nitrogen is also necessary for formation and subsequent dissociation of Rb-Xe van der Waals molecules at low pressure. The process may be described by the expression,^{7,53}



The formation of van der Waals complexes results from the inelastic collision between a noble gas atom and an alkali metal atom, and molecular nitrogen absorbs kinetic energy from both noble gas and alkali metal atoms, allowing for the inelasticity of the collision. Following transfer of the angular momentum to the nucleus of the noble gas atom, a collision with a second nitrogen molecule dissociates the van der Waals molecule.⁷ The van der Waals molecules are so weakly bound together, that nearly every collision with a quenching *or* buffer gas molecule results in dissociation. The role of the van der Waals molecules in the spin-exchange enhancement of the ¹²⁹Xe nuclear spin is discussed in more detail in the following section.

Rubidium-Xenon Spin Exchange Through Collisional Processes

The transfer of angular momentum from the alkali metal valence electron to the nucleus of a rare gas atom can occur either while the atoms are bound together as short-lived van der Waals molecules or through simple binary collisions, as depicted in **Figure 3-5**.^{1,2,7,57} In the case of the smaller noble gases, such as ³He, spin exchange is primarily the result of binary collisions of the alkali metal vapor and noble gas. The lifetime of the

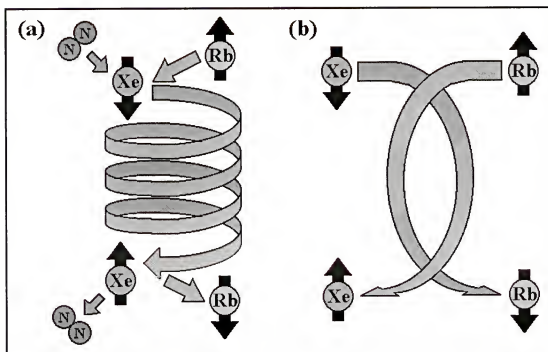


Figure 3-5. Mechanisms for spin exchange of optically pumped alkali metal vapor with a noble gas. (a) Polarization transfer can be accomplished through the formation and break-up of an alkali metal/noble gas van der Waals molecule. Collisions with a third-body participant, typically nitrogen, are necessary at both the formation and the destruction of the Rb-Xe molecule. (b) Binary collisions of the alkali metal and noble gas molecules will also induce a polarization transfer, but the efficiency is significantly lower transfer through the Rb-Xe van der Waals molecule.

binary collision typically lasts for only a few picoseconds, short compared to the timescale of the spin evolution under the alkali atom electronic-noble gas nuclear hyperfine interaction.⁷ Thus, higher efficiencies of spin exchange are achieved resulting through the formations of van der Waals molecules. Spin exchange proceeding through the formations of van der Waals molecules is best achieved at low pressures (< 350 torr), and is the dominant mechanism by which nuclear spin can be enhanced for the heavier noble gases, such as ^{129}Xe . The Rb-Xe van der Waals molecule provides the appropriate

interatomic distance and contact time (a lifetime of up to tens of nanoseconds) for the angular momentum to be efficiently exchanged to the noble gas nucleus.⁷ At pumping cell pressures above approximately 350 torr, the rate of spin exchange through binary collisions begins to exceed that through the formation of van der Waals molecules.^{1,2,7,57}

At equilibrium, the rate of formation of the van der Waals molecules, $1/T_K$, and their mean molecular lifetime, τ , are related by the simple expression,

$$\frac{[^{129}\text{Xe}]}{T_K} = \frac{[\text{Rb}^{129}\text{Xe}]}{\tau}, \quad (3-7)$$

and are coupled to a pressure-independent rate constant Z through the relationship,^{2,53,57}

$$\frac{[\text{Rb}^{129}\text{Xe}]}{\tau} = Z[\text{Rb}][^{129}\text{Xe}][X]. \quad (3-8)$$

Note that $[^{129}\text{Xe}]$ in this expression takes into account the rate of formation of the Rb- ^{129}Xe van der Waals molecules, while $[X]$ is the third body density.² The quantity $[X]$ must include all other species, including other xenon isotopes, quenching gas, and buffer gas densities.

The spin exchange process involves the transfer of angular momentum from the electron spin \vec{S} of the alkali metal, to the nuclear spin \vec{K} of the noble gas. As mentioned earlier, the competing interaction involves the spin-dependent process coupling \vec{S} with

the rotational angular momentum \vec{N} of the van der Waals molecule.^{2,3,56} The magnitude of the spin-rotation interaction term determines the extent by which spin relaxation occurs though the rotational motion of the van der Waals molecule and, therefore, the efficiency of the spin exchange to the nucleus of the noble gas.⁵³ For magnitudes of B_0 in the ranges of tens to hundreds of Gauss, the term $g\mu\vec{S} \cdot \vec{B}_0$ has the effect of suppressing the relaxation processes involving rotation of the van der Waals molecule ($\gamma\vec{S} \cdot \vec{N}$), thereby allowing more efficient transfer to the nucleus of the noble gas.⁵⁸

The Rb-¹²⁹Xe spin-exchange rate can be defined by the overall rate expression, equation 3-9,

$$\gamma_{SE} = \kappa_{SE} [Rb], \quad (3-9)$$

where κ_{SE} is the velocity-averaged binary spin exchange cross section $((3.7 \pm 0.6) \times 10^{-16} \text{ cm}^3 \text{ s}^{-1})$ and $[Rb]$ the density of polarized rubidium atoms.⁵⁵ The efficiency for transfer of angular momentum from a Rb in a collision with a ¹²⁹Xe atom has been estimated at approximately 10%,² with most of the remaining angular momentum lost through the coupling to the rotation of the van der Waals molecule. The build-up of the ¹²⁹Xe nuclear-spin polarization as a function of the polarizing time t is given by equation 3-10,

$$P_{Xe}(t) = \frac{\gamma_{SE}}{\gamma_{SE} + \Gamma} P_{Rb} \left(1 - e^{-(\gamma_{SE} + \Gamma)t} \right), \quad (3-10)$$

where Γ is the rate of ^{129}Xe nuclear spin relaxation.^{3,50,55} It has been shown that the magnitude of Γ results primarily from surface-induced relaxation pathways.⁵¹ These relaxation processes substantially limit the spin-lattice relaxation time T_1 , thereby limiting the efficiency of spin exchange optical pumping.

Reducing the rate of Nuclear Spin Relaxation Due to Wall Interactions

It has been shown,^{51,59} that the coating of the pumping cell walls with high molecular mass waxes or with siliconizing agents can substantially reduce the value of the spin relaxation, Γ . With the improvement, $\gamma_{SE} \gg \Gamma$,⁵¹ equation 3-10 reduces to

$$P_{Xe}(t) = P_{Rb} \left(1 - e^{-\gamma_{SE} t} \right), \quad (3-11)$$

indicating that a reduction in Γ can substantially increase the theoretical maximum polarization enhancement attainable for ^{129}Xe . The most common coating used by the noble gas SEOP community is a commercial siliconizing agent known as Surfasil (Pierce Scientific).^{51,59} Surfasil is composed primarily of octamethyldichlorotetrasiloxane and through silanol condensation with surface hydroxyls becomes covalently bonded to the cell walls. Typically, this coating can increase the ^{129}Xe nuclear spin relaxation time from tens or hundreds of seconds to the scale of thousands of seconds.⁵⁹ Note that although other coatings, such as those presented in **Table 3-1** can provide longer nuclear spin relaxation times, Surfasil and other siloxane coatings have the advantages that they are

Table 3-1. Measured ^{129}Xe T_1 Values for SEOP Enhancement of ^{129}Xe With Optically-Pumped Rubidium Vapor In Coated and Uncoated Cells. Replicate relaxation time measurements were taken for cells coated using identical procedures for the selected coatings indicated below.⁵⁹

	T_1 (s)			
	Cell 1	Cell 2	Cell 3	Cell 4
Uncoated Pyrex	1300±40	2900±30	2600±40	2300±50
Surfrasil	10800±90	10300±90	9900±120	9400±200
Dotriacontane	12300±140	10010±70	12430±710	11808±570
Dotriacontane- <i>d</i>	13040±170	14270±220	12600±160	13970±270
Polyethylene	13700±700	12200±400
Polyethylene- <i>d</i>	11700±800	11800±900

chemically bonded to the surface of the pumping cell and that coating of uniform thickness can be easily applied.

Summary

The use of atomic xenon as a molecular probe, with ^{129}Xe NMR as the detection method, has become a highly popular technique in recent years. In general, this is a noninvasive technique, and chemical characteristics of xenon make it appropriate for use in a wide range of applications, biological studies in particular. Unfortunately, the ^{129}Xe isotope lacks efficient spin-lattice relaxation mechanisms,^{12,17} making signal averaging to obtain increased signal:noise very time consuming. This chapter has discussed the application of alkali metal-noble gas spin exchange optical pumping (SEOP) to enhance the nuclear spin polarization beyond that achieved at thermal equilibrium by several

orders of magnitude. In subsequent chapters, the specific parameters used for the generation of SEOP enhanced ^{129}Xe to complete each experiment will be provided. For a general discussion of the SEOP experiment and apparatus, Appendix I provides diagrams of the SEOP apparatus, and Appendix II discusses calculation of the enhancement factor of the ^{129}Xe NMR signal.

CHAPTER 4

RECENT APPLICATIONS OF SEOP ENHANCED ^{129}Xe NMR

Introduction

In general, NMR is the most suitable technique for probing local chemical environments in solution, or within microporous materials, because it can be used to investigate the electronic perturbations in rapidly moving molecules.³⁸ It provides information on both molecular structure and on chemical dynamics. Direct NMR detection of the nuclei of solid materials, however, suffers from two disadvantages. The first is the inability to distinguish between bulk spins and surface spins, the latter being most important when investigating, for example, catalytic properties. The second is the low sensitivity of surface spins to direct NMR detection. To probe internal structures, channels and pores, molecular probes have been used to investigate more closely the chemical environments in proximity to adsorption sites on the surfaces of solids, or of macromolecules in solution. ^{129}Xe NMR, using atomic xenon as the molecular probe, has been widely used to probe porous materials. Atomic xenon is chemically inert, thus remaining as noninvasive to the sample as direct detection techniques, and is often site-selective, due to the hydrophobic nature of xenon. The high polarizability of the electron cloud of xenon ensures that the ^{129}Xe NMR chemical shift and line shape are particularly

sensitive to environmental factors, to physical interactions with other chemical species, and to the nature of adsorption sites. Investigations of xenon binding in solution and to solid surfaces with ^{129}Xe NMR have demonstrated the ability to extract not only the dimensions, symmetries, of pores and channels, but also the dynamics of xenon binding to the surfaces.^{14,16} Prior to 1990, only conventional ^{129}Xe NMR techniques had been adapted to investigate the chemical environments of a number of microporous materials; notable among those were zeolites^{9-11,14,60-63} and clathrates.^{12,15,16,23}

Although these studies were successful in extracting much structural and chemical information, the low sensitivity provided by thermally polarized ^{129}Xe limited the applications. In the thermally equilibrated NMR experiment, low detection sensitivity can be overcome through the signal averaging of multiple FID acquisitions. A material for which dissolved or adsorbed atomic xenon exhibits rapid ^{129}Xe spin-lattice relaxation can best be investigated using the signal-averaged experiment. In these instances, the time necessary for obtaining spectra having desirable signal:noise values typically does not diminish the effectiveness of the experiment. However, for situations when long relaxation times are observed for ^{129}Xe , the investigation is best accomplished through the application of the SEOP ^{129}Xe NMR experiment.¹⁴ This chapter will provide examples of applications for which the use of the SEOP ^{129}Xe NMR experiment has proven to be remarkably advantageous, and often necessary. The examples were selected with the objective of demonstrating abilities of SEOP ^{129}Xe NMR that would be important for the success of the studies proposed in this dissertation: (1) detection of the adsorption of spin-polarized gas to a solid surface; (2) determination of cavity and

channel dimensions of porous materials of void spaces occupied by xenon gas; (3) the transfer of polarization from spin-polarized xenon to desired nuclei of the host structure; (4) detection of the site-selective adsorption of xenon to solid surfaces or to molecules in solution; and finally (5) monitoring the progress of reactions *in situ*, in real time. A discussion of the applications of SEOP ^{129}Xe NMR specifically to studies of clathrate hydrates has been accommodated in other sections of this dissertation.

Selected Applications

Applications of SEOP Enhanced ^{129}Xe NMR to Surface Adsorption Studies

In 1991, Raftery and co-workers¹⁹ reported the first attempt to overcome the low sensitivity of the conventional ^{129}Xe NMR experiment in a surface absorption study by using alkali metal-rare gas spin exchange optical pumping to enhance the polarization of the ^{129}Xe nuclei by several orders of magnitude. The resulting ^{129}Xe NMR single-scan spectra for the exposure of powdered benzantracene (surface area, $\sim 0.5 \text{ m}^2/\text{g}$) to spin-polarized xenon gas indicated a distinct resonance associated with xenon adsorbed onto the powder surfaces. Thus, Raftery *et al.*¹⁹ demonstrated that the low sensitivity of adsorbed species, even for microporous solids with low surface areas, could quite easily be overcome by the enhancement of the ^{129}Xe NMR signal through SEOP techniques. At 158 K, the xenon resonance for gas adsorbed to the benzantracene surfaces was observed shifted downfield 10 ppm from that of the free gas.¹⁹ At 153 K, the ^{129}Xe resonance shifted to 32 ppm relative to the free gas, and exhibited a clearly asymmetric

line shape, an indication of the distortion of the electron cloud xenon exhibits as it is adsorbed onto the surface of the benzantracene.

Two years later, Raftery, *et al.*⁶⁴ exploited the technique for materials with much larger surface areas, such as polyacrylic acid, which has a surface area thirty times that of benzantracene. The high sensitivity of the enhanced NMR signal meant that smaller quantities of xenon could be used and still provide spectra with desirable signal:noise. With such a wide range of probe gas pressures now applicable, the pressure dependence of the chemical shift of adsorbed xenon could be explored. The chemical shift observed for xenon adsorbed onto the surfaces of molecular crystals like polyacrylic acid results from the xenon-surface interaction and the xenon-xenon interactions.^{14,19} For monolayer coverage of the sample, represented by θ , the resulting chemical shift can be represented as a virial expansion similar to that for the free gas,

$$\delta(T, \theta) = P_s \sigma_{0s}(T) + (P_s)^2 \sigma_{1s}(T) \theta + (P_s)^3 \sigma_{2s}(T) \theta^2 + \dots \quad (4-1)$$

where P_s is the probability of finding the xenon at the surface, and $\sigma_{0s}(T)$ and $\sigma_{1s}(T)$ are the temperature dependent coefficients describing the xenon-xenon interactions and xenon-surface interactions, respectively.¹⁴ Since Raftery, *et al.*¹⁹ observed linear responses of the chemical shift associated with changes in the xenon pressure, the higher order terms may be neglected; the chemical shifts observed are due primarily to xenon-surface interactions, and not xenon-xenon collisions. This is consistent with the fact that only low xenon loading pressures, typically less than 200 torr, were employed.

Investigating Local Environments in Microporous Materials: Zeolites

After Fraissard and co-workers⁹⁻¹¹ first proposed that ^{129}Xe NMR could be used to characterize the surfaces and interiors of zeolites and related materials, the use of ^{129}Xe NMR to investigate pore and channel dimensions, active site acidity, and diffusion characteristics of various microporous silicates has become a routine technique.^{9-11,14,16,60-}

⁶³ With the recent development of apparati that would supply continuous streams of spin-polarized ^{129}Xe gas, the design of Driehuys *et al.*⁵⁰ being the mostly widely reproduced, investigators have begun to take advantage of the remarkable sensitivity afforded by spin-polarized ^{129}Xe NMR.^{65,66}

Terskikh, *et al.*,⁶⁶ in 2001, employed the use of continuous flow spin-polarized ^{129}Xe in order to acquire spectra for single crystals of silicalite, an aluminum-free version of the synthetic zeolite ZSM-5.^{67,68} Even with the increased sensitivity, each spectrum required signal averaging of 512 scans, taken with $\pi/2$ pulses, 5-s delay between FID acquisitions. It was estimated that obtaining spectra with similar quality through thermally polarized ^{129}Xe NMR would have taken 800-2000 times longer.⁶⁶ Enhancement of the ^{129}Xe NMR signal meant that much lower partial pressures of xenon could be employed. In turn, the reduced pressures ensured that xenon-surface interactions, and not xenon-xenon interactions, would be the dominant factors determining the chemical shielding tensor for ^{129}Xe . The low partial xenon pressures also minimized the exchange of xenon with the gas phase.⁶⁶ A temperature dependence study, carried out from 295 K down to 140 K, revealed that the chemical shift anisotropy expected from xenon interacting with the walls generally elliptical voids within the crystals became visible

only as the temperatures was reduced. The channels of silicalite have roughly elliptical free-space cross sections with axes ranging 5.2-5.8 Å.⁶⁸

Two separate NMR resonances are observed for each orthogonal orientation of the silicalite crystals, indicating an exchange of xenon between two microscopically different regions, a fact that is not readily obvious through crystallographic studies of silicalite crystals. It is known that single crystals of orthorhombic silicalite transform reversibly at 340 K into equal quantities of similar monoclinic crystals, a process referred to as “twinning”. One of the ^{129}Xe NMR resonances correspond to a second series of layers of the silicalite crystal, identical in structure to the (001) layers, but turned 90° about the z axis, so that the two ^{129}Xe resonances would have a 90° phase difference. This is consistent with the experimental observations, particularly the convergence of the two ^{129}Xe NMR resonances at a crystal orientation of 45°.

Terskikh, *et al.*⁶⁶ have demonstrated that the SEOP enhancement of the ^{129}Xe NMR signal makes possible studies of low surface area, and single crystals of, materials for which the low NMR sensitivity would make such studies unfeasible. Taken with the spin-polarized xenon, a single spectrum required an acquisition time of 43 minutes; in accordance with their lower estimate, the acquisition of a spectrum of similar quality, without the use of spin-polarized noble gas, would have taken 24 days.⁶⁶

Polarization Transfer Techniques

The transfer of magnetization from a spin-polarized ^{129}Xe reservoir to the thermally equilibrated spins of a solid surface, or of a molecule in dilute solution, offers

the possibility for great increases in the NMR detection sensitivity. Signal enhancements in the NMR spectra of recipient nuclei (most commonly ^1H , ^{13}C or ^{29}Si) have been observed from techniques that have exploited the Overhauser effect,⁶⁹⁻⁷¹ low field mixing,⁷² and direct cross-polarization (Hartmann-Hahn) techniques.^{73,74}

In the most simple of the polarization transfer techniques, the exchange of polarization from spin-polarized ^{129}Xe to a spin system of interest can be accomplished by taking advantage of the "spin polarization-induced nuclear Overhauser effect", or SPINOE.⁷¹ SPINOE enhancement of ^1H NMR signals was first observed resulting from cross-relaxation from laser-polarized ^{129}Xe dissolved in fully deuterated benzene to $\text{C}_6\text{D}_5\text{H}$ solute molecules.⁷¹ Although the ^{129}Xe was spin-polarized several orders of magnitude beyond the Boltzmann polarization, only a fifty percent increase in the ^1H NMR signal intensity was achieved for the protons of $\text{C}_6\text{D}_5\text{H}$.⁷¹ This low SPINOE enhancement demonstrated that a SPINOE enhancement of the signal was indeed achieved, but that the technique suffers from inefficient transfer of nuclear spin magnetization.

Song *et al.*⁷⁰ found that spin-polarized xenon selectively bound itself to the hydrophobic pocket of the α -cyclodextrin in solution. ^1H NMR signals from protons of the cyclic oligosaccharide were enhanced according to their proximity to the binding site for xenon, thereby providing an opportunity not only to improve the sensitivity of NMR detection for α -cyclodextrin, but also to extrapolate dynamic and conformational information about the solute species in solution. The dipolar relaxation is sensitive to the

distance between xenon and the recipient nucleus, and varies with a $1/r^6$ relationship,⁷⁵ so that accurate estimates of interatomic distances can be determined.

For SPINOE to be most successful, the spin-polarized rare gas atoms must be brought into direct dipolar contact with the high temperature spins. Since the formation rate, and lifetime of, the xenon-solute pair determines the effectiveness of the ^{129}Xe - ^1H transfer of polarization, dramatic increases in NMR sensitivity for the spins of solute molecules in dilute solutions will likely not be realized. Increases in NMR sensitivity are best achieved when the xenon atom is strongly bound to the host in close proximity to the spins of interest, which suggests that more effective enhancements will be observed for xenon adsorbed to solid surfaces. The dependence of ^1H NMR signal enhancements to the binding site proximity suggested that SPINOE experiments could be used to identify adsorption sites and provide structural characterizations of larger macromolecules.

Bowers *et al.*⁷² first demonstrated that magnetization could be transferred from spin-polarized ^{129}Xe to another spin system via thermal mixing at low magnetic fields. The molecular species of interest, in this case isotopically enriched $^{13}\text{CO}_2$, was condensed into a solid matrix of laser-polarized xenon, at a field of ~ 150 G. Then the spin temperatures of the abundant and rare spins were allowed to equilibrate at low field, up to a few tens of Gauss. After the desired mixing time, the sample was transferred to a high field (4.2 T) for detection of the ^{13}C signal. ^{13}C NMR signal enhancements as high as 200 have been achieved using the thermal mixing technique.

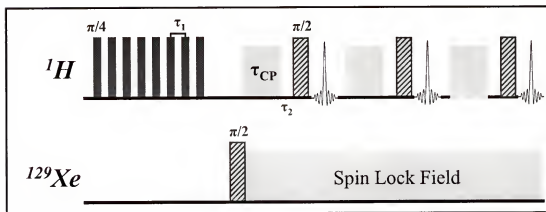


Figure 4-1. The pulse sequence employed by Long and co-workers⁷⁴ to transfer nuclear spin polarization from a reservoir of laser-polarized ^{129}Xe to the protons on the surface of poly(triarylcarbonyl) at 213 K is presented above. Proton spins of the sample were saturated using a train of eight 45° rf pulses ($\tau_1 = 1$ ms). Spin polarization is transferred to the surface protons by repeated cycles of Hartmann-Hahn matching ($\tau_{\text{CP}} = 200$ μs) to the ^{129}Xe spins. Detection of the ^1H spins was made using a dipolar echo to reduce the effects of spectrometer dead time. The delay between Hartmann-Hahn matching and the acquisition pulse is $\tau_2 = 200$ μs .

The low fields employed for thermal mixing, however, cause the technique to suffer from shorter spin relaxation times due to the low applied fields, and the sample must still be returned to high field for detection of the NMR resonance. In addition, the cross-relaxation is nonselective in the enhancement of solute or surface spins. Selective polarization transfer may be achieved by high field methods, such as Hartmann-Hahn matching of the spin-polarized ^{129}Xe to the nuclei of interest. In 1993, Long and co-workers⁷⁴ demonstrated that the nuclear spin from laser-polarized ^{129}Xe could be transferred directly, and selectively, to the protons on the surface of poly(triarylcarbonyl) at 213 K. The CP pulse sequence is depicted in **Figure 4-1**. Eight 45° pulses employed in rapid succession ($\tau_1 = 1$ ms) saturate the proton spins of the sample and destroy the thermal polarization of the ^1H spins. The protons spins are then cross polarized by

repeated cycles of Hartmann-Hahn matching to the ^{129}Xe spins with contact periods each of 200 μs . Detection of the ^1H spins was made using a dipolar echo to reduce the effects of spectrometer dead time. Enhancements of the surface spins by excess of 70 were estimated. At current, this is the only reported case where the selective cross-polarization from spin-polarized ^{129}Xe to surface nuclei employing Hartmann-Hahn matching has been successfully achieved. It is believed, however, that this technique could work just as well for selective cross-relaxation from ^{129}Xe to ^{13}C and to ^{29}Si surface nuclei.

Selective Binding of Xenon In Inclusion Compounds: Cryptophane-A

Xenon has demonstrated selective binding to a variety of inclusion compounds, notably α -cyclodextrin,^{16,70} hemicarcerands,^{76,77} and self-assembling dimers.⁷⁸ The term “binding of xenon” for the association of xenon to a solute molecule suggests that the association of the xenon-solute pair occurs on a timescale long enough for the pair to be considered a supramolecule.⁷⁹ In 1999, Luhmer *et al.*⁷⁹ successfully investigated the *in-solution* binding of SEOP enhanced ^{129}Xe to cryptophane-A. The cryptophane-A molecule is spherical in shape, comprised of two bowl-shaped cyclotrimeratrylene structures that are bridged at three positions by $\text{OCH}_2\text{CH}_2\text{O}$ spacers.⁷⁹⁻⁸¹ The hollow sphere of cryptophane-A serves as host to a range of small molecules, particularly xenon. In fact, xenon binds reversibly to the hydrophobic interior of cryptophane-A forming a 1 to 1 guest-host complex with an association constant greater than 3000 M^{-1} at 278 K.^{79,80} Xenon bound to the hydrophobic cavity of cryptophane-A exhibits a ^{129}Xe NMR

resonance 62.3 ppm downfield from that of a free gas reference, ~160 ppm upfield from that of xenon dissolved in (CDCl₂)₂ solvent.

First, Luhmer *et al.*⁷⁹ demonstrated that an SEOP ¹²⁹Xe NMR spectrum of xenon bound to the hydrophobic cavity of cryptophane-A could be acquired from application of a single, small tip angle (~2.5°) rf pulse. The comparative broadness of the resonance could be used as an indication of the rate of chemical exchange with fresh xenon in solution. With a recycle time of 60 s, a spectrum acquired from a thermally polarized sample with comparable signal to noise would have required hours of signal averaging.⁷⁹ (The T₁ for bound xenon is quite short, so that a recycle delay of only 6 s was necessary in their prior study to acquire a signal for bound xenon in the conventional ¹²⁹Xe NMR experiment.⁸⁰ The T₁ for unbound xenon, dissolved in (CDCl₂)₂, however, is much longer, so that the spectra obtained using the recycle delay of 6 s do not yield quantitative relationships.) Spin-lattice relaxation times were also able to be determined in single-batch SEOP ¹²⁹Xe NMR experiments, since such small tip angles were employed.

In addition, Luhmer *et al.*⁷⁹ were able to measure SPINOE enhancements to the various ¹H NMR resonances observed for cryptophane-A. Steric hindrances in hemicarcerands impede the escape of guest molecules, however, binding of xenon to cryptophane-A suffers from no such restrictions of guest migration, so that residence times for xenon are on the timescale of milliseconds.^{79,80} This relatively short residence time may be advantageous for observing the SPINOE; multiple interactions of the binding site nuclei with fresh spin-polarized xenon may enhance the signal more so. ¹H NMR signal enhancements ranged from 13 % for protons of the OCH₂CH₂O bridges, to

less than 3 % for equatorial protons on the exterior of cryptophane-A. The observed selective ^1H enhancements allowed xenon-proton inter-nuclear distances to be estimated.⁷⁹ The assessment of SPINOE enhancements and ^1H - ^{129}Xe cross-relaxation rates can be used to directly probe molecular structure and dynamics in solution.

Using SEOP ^{129}Xe NMR, Lumher *et al.*⁷⁹ were able to demonstrate the ability to obtain single-scan, small tip angle spectra of xenon bound to the hydrophobic center of cryptophane-A. Acquisitions on the timescale of hours would be necessary to obtain comparable signal:noise values using thermally polarized ^{129}Xe NMR techniques. In an earlier study,⁸⁰ equilibrium constants, but not rate constants, for the competitive binding of xenon versus chloroform were determined. Using SEOP ^{129}Xe NMR in the time-resolved experiment, it would be possible to determine not only the rates of exchange of xenon for chloroform (which has demonstrated a lower association constant), but also the direct rate of formation of the xenon-cryptophane-A complex.

Time-Resolved Experiments Using SEOP Enhanced ^{129}Xe NMR

The SEOP enhancement of the ^{129}Xe nuclear spin polarization by several orders of magnitude, and the application of small tip angles for detection of the NMR signal which minimizes the depletion of the polarization reservoir, has allowed for the development of time-resolved ^{129}Xe NMR experiments having very short recycle times. Applications have included SEOP ^{129}Xe NMR monitoring of reactions with xenon *in situ*, and the determinations of diffusion constants through porous materials,⁸²⁻⁸⁵ particularly with the development of *in situ* continuous flow methods.^{22,86,87}

In 2001, Nossov *et al.*⁸⁸ performed the SEOP ^{129}Xe continuous flow, *in situ* experiment to monitor the transformation of the solid $[\text{CuL}_2]$ complex (where $\text{L} = \text{CF}_3\text{COCHCOC}(\text{OCH}_3)(\text{CH}_3)_2$) from its open β form, or its more dense α form. Only the open β form has channels and is capable of allowing passage of guest molecules through the solid, and thus is characterized as a sorbent material; a molecular-level isomerization to the more dense, α form, can be induced by the presence certain organic agents.⁸⁸⁻⁹⁰ Thus, the solid $[\text{CuL}_2]$ complex is considered have switchable “sorbent functionality”. When the complex is fully transformed to its β form, xenon gas is allowed to pass through the narrow channels of the solid, and a ^{129}Xe NMR resonance is revealed shifted 109.7 ppm (in the presence of 300 torr of methylene chloride to induce transformation to the β form) ppm downfield from that of the free gas, remarkably narrow despite the presence of paramagnetic $\text{Cu}(\text{II})$ centers.⁸⁸

By mixing methylene chloride into the spin-polarized xenon gas flow (30 cm^3/min total flow, 300 torr methylene chloride over a 1 hour period), Nossov and co-workers⁸⁸ were able to induce the gradual transformation of dense α - $[\text{CuL}_2]$ complex to its β form. Spectra were acquired every 15 s, and demonstrated a time-dependent downfield shift of the ^{129}Xe NMR resonance with a maximum at ~ 116 ppm at the start of the experiment, and ending at ~ 95 ppm, as referenced to the free gas signal. However, at 343 K the β - $[\text{CuL}_2]$ complex is transformed back to the α form exhibiting a time independent ^{129}Xe NMR chemical shift. Perhaps, for the transformation to the more dense form to occur, xenon must be expelled prior to the start of conformational changes necessary to prepare the α form of the solid complex.

Summary

It has been just over a decade¹⁹ since the first successful application of optical pumping for enhancing the ^{129}Xe high-field NMR signal of xenon physisorbed onto the surface of a molecular solid. Since that time, the expansion of ideas into applications for spin-polarized ^{129}Xe has been far from linear. SEOP ^{129}Xe NMR has been exploited to investigate the active sites of porous solids, to explore the various dimensions and symmetries of cavities and channels in solids and in biological macromolecules, and to enhance the NMR sensitivity of surface spins in both solid and liquid states. The more challenging experiments will involve the cross-polarization to surface nuclei, and will necessarily require the development of new techniques that will localize the xenon atoms more strongly on the surface. Initial attempts have been successful in transferring fractional amounts of the xenon polarization to other nuclei, particularly in cases where there are site-specific adsorptions of xenon. With maximum enhancements of ~ 200 for the NMR signals of ^1H , ^{13}C and ^{29}Si , however, and ^{129}Xe polarization enhancements of up to 18,000, the development of CP techniques must now concentrate on the improvement of the efficiencies of polarization transfers.

CHAPTER 5

STRUCTURES AND THERMODYNAMICS OF GAS CLATHRATE HYDRATES

Introduction

Gas clathrate hydrates are nonstoichiometric compounds in which small gaseous guest molecules are entrapped, or enclathrated, into a crystalline $(\text{H}_2\text{O})_n$ lattice. To accommodate the guest molecules into the structure, hydrogen-bonded water molecules of the lattice reorient to form a three-dimensional network of cavities (dodecahedral, tetrakaidecahedral, and hexakaidecahedral). Formations of clathrate hydrates have been observed on surfaces of ice particles and in supercooled liquid water, wherever water molecules have the freedom to reorient themselves to form these cage structures. When the cages form without the inclusion of a guest molecule, the structures are unstable, collapsing under the strong hydrogen-bonding forces bridging opposing cavity walls. Enclathration of a guest molecule prevents collapse of the $(\text{H}_2\text{O})_n$ cage so long as it experiences only weak interactions (limited mostly to van der Waals forces) with the host lattice. Strong intermolecular interactions between guest and host lattice may actually contribute to buckling of the cage and its eventual collapse.^{12,44,91,92}

Before a discussion of the application of SEOP enhanced ^{129}Xe NMR to the structural and dynamical studies of xenon gas clathrates hydrates, some important

historical developments in the field of hydrate clathrates chemistry will be reviewed. This will be followed by an overview of the current state of knowledge of these materials.

Historical Perspective

The first known clathrate was the chlorine gas clathrates hydrate discovered by Sir Humphrey Davy in 1811.⁴² Chemical analyses led to the characterization of this hydrate as a true chemical compound, and not an inclusion compound.^{42,91,92} Characterization of clathrate hydrates as chemical compounds was accepted until 1823, when Faraday's more detailed analysis of the chlorine gas hydrate revealed that the substance was a nonstoichiometric inclusion compound.^{42,92} Similar studies of gas hydrates considered the clathrates to be curiosities, and not until the early 1900's were practical applications for gas clathrates hydrates realized. Between 1880 and 1930, Villard^{91,93,94} and de Forcrand^{42,91,95,96} pioneered preparation techniques for a selection of gas hydrates and, in particular, were successful in manufacturing in a laboratory setting the clathrate hydrates of the noble gases argon, krypton, and xenon. Soon after, researchers discovered the existence of clathrate hydrates of natural gases and of a variety of other organic molecules. Early literature on these compounds addressed the determination of the chemical compositions and on their collective and individual thermodynamic properties.⁴² Very little literature of the time discussed the mechanisms or rates of clathrate hydrate formation.

In the 1930s, researchers more thoroughly explored the practical implications for gas clathrate hydrates. Natural gas hydrate crystals were discovered forming in gas lines at temperatures well above water's freezing point,⁴² making it more difficult to pinpoint the locations that were more susceptible to blockage. In response, research was directed towards better understanding the mechanism of gas hydrate crystallization, and on means to inhibit their formation. In particular, these studies focused on the formations of various hydrocarbon hydrates. A new reason to study the thermodynamics and the kinetics of formation came about in 1942, when several commonly used refrigerant gases were found to effectively form clathrate hydrates.⁹² Due to the non-toxic and inert properties of these substances, and the ease with which the clathrate hydrates of these gases could be prepared, novel water desalination technologies involving purification through gas clathrate hydrate formation were proposed. Development of methods for water desalination was vigorously pursued far into the 1960s, until the public concern about the availability of fresh water subsided.⁹²

In more recent decades, significant quantities of natural gas hydrates have been discovered in the Arctic and Antarctic permafrost, and in marine sedimentary deposits. With the discoveries of these naturally occurring hydrate reservoirs, in combination with the growing concerns over the availability of fossil fuels, there has been a reemergence of interest in understanding the hydrates at the levels of structure, thermodynamics, and kinetics, and as well the environmental and economic conditions.

Structural Properties of the Gas Clathrate Hydrates

The two most common crystal structures observed for gas clathrate hydrates were elucidated first through X-ray diffraction measurements performed by three research groups: by Claussen; by Pauling and Marsh; and by von Stackelberg and Müller.⁹⁴ The two most commonly observed are referred to simply as type I and type II structures. By 1984, approximately 110 simple clathrate hydrates had been discovered and structurally characterized according to these two proposed crystal structures.⁹¹ Approximately forty of these were determined to be of the type I variety, and most of the remaining were classified as type II. Hydrate guest molecules have ranged in size and shape from the smaller noble gas atoms such as argon to larger heterocyclic molecules such as dioxane. Various noble gases, diatomic molecules and triatomic compounds, inorganic polyatomic molecules, and an assortment of hydrocarbons, ketones, and amines have been enclathrated.⁹²

The Type I and Type II Clathrate Hydrate Structures

For two-dimensional water clusters, pentagonal and hexagonal structures are the most stable. This rule of thumb for the stability of water clusters extends into three dimensions, where the enclathration of a small guest molecule into an $(\text{H}_2\text{O})_n$ cage typically results in one of three common structures containing only pentagonal and hexagonal faces. The dodecahedron, tetrakaidecahedron, and hexakaidecahedron (**Figure 5-1**) are the most commonly observed among the hydrate cage structures. These three cavity types combine to form the two common crystal structures, type I and type II.^{42,91}

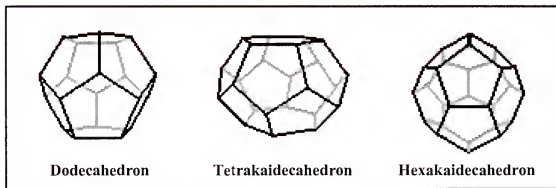


Figure 5-1. Three of the most common cavity types found in clathrate hydrates. The (a) dodecahedron has the smallest internal cavity, with twelve pentagonal faces; the (b) tetrakaidecahedron consists of twelve pentagonal faces and two hexagonal faces; the (c) hexakaidecahedron has two hexagonal faces in addition to the faces of the tetrakaidecahedron.

Thorough discussions of clathrate hydrate structures using Euclidean geometrical terminology (*i.e.* - dodecahedron, tetrakaidecahedron, and hexakaidecahedron) became tedious. Thus, in 1984, Jeffrey⁹² suggested employing a shorthand notation for identifying the cavities of the clathrate hydrates by specifying only the numbers of pentagonal and hexagonal faces in the polyhedron. In this system of nomenclature, each cavity type would have the representation of $n_i^{m_i}$, where n_i refers to the number of edges in the polygon face of type i ($n_i = 5$ for pentagonal, $n_i = 6$ for hexagonal); m_i refers to the number of faces of that type, i , in the entire polyhedron. For example, there are twelve pentagonal faces comprising a dodecahedral cage; thus, the dodecahedron has values $n_i = 5$ and $m_i = 12$, providing a representation of 5^{12} for the polyhedron. It follows that the tetrakaidecahedral and hexakaidecahedral cages will have representations $5^{12}6^2$ and $5^{12}6^4$, respectively.^{42,92}

Table 5-1. A Summary of Physical Characteristics of the Type I and Type II Gas Hydrate Clathrates.⁴²

Hydrate Crystal Structure	Type I		Type II	
	Small	Large	Small	Large
Cage Size	5 ¹²	5 ¹² 6 ²	5 ¹²	5 ¹² 6 ⁴
Cage Representation				
Number of Cages/Unit Cell	2	6	16	8
Average Cavity Radius, Å	3.91	4.33	3.902	4.683
Coordination Number	20	24	20	28
Crystal System	Cubic		Cubic	
Space Group	Pm3n		Fd3m	
Lattice Description	Body Centered		Diamond	
Lattice Parameter, Å	12		17.3	
Ideal Unit Cell Formula	6L·2S·46H ₂ O		8L·16S·136H ₂ O	

The type I gas hydrate clathrate unit cell contains 46 host water molecules, arranged to form two pentagonal dodecahedral cavities (**Figure 5-1a**) and six tetrakaidecahedral cavities. The smaller dodecahedral cavities (**Figure 5-1b**) are comprised of twenty water molecules forming polyhedra with twelve pentagonal faces, and having an average cavity radius of 3.91 Å. **Table 5-1** summarizes these structural characteristics, and **Figure 5-2** illustrates the structure of the type I hydrate crystal. The larger tetrakaidecahedral cages have two hexagonal faces in addition to a set of twelve pentagonal faces requiring the arrangement of 24 water molecules.^{12,97} Cavities of the type I clathrate hydrate will accommodate guest molecules with maximum van der Waals diameters of about 5.8 Å.^{94,97} Based on the diameters of guest molecules which have been successfully enclathrated, maximum free diameters of 5.2 Å and 5.8 Å have been assigned to smaller and larger cages of the type I clathrate hydrate, respectively.^{16,98} (A different literature source has reported values of 5.0 Å and 6.7 Å,⁹¹ so the diameters of

the clathrate hydrate cavities are somewhat flexible.) The unit cell lattice parameter for the hydrate structure of the type I variety, as established through X-ray diffraction techniques, was determined to be $11.84 \pm 0.02 \text{ \AA}$ (at 100 K).^{24,47,94}

The type II clathrate hydrate unit cell consists of 136 water molecules, hydrogen-bonded to form sixteen dodecahedral cavities and eight large hexakaidecahedral cavities (**Figure 5-1c**).^{12,94,97,99} The dodecahedral cages of the type II structure are nearly identical to those found in the type I hydrate, but often with slight distortions from the regular polyhedron. Hexakaidecahedral cavities are larger than the tetrakaidecahedral of the type I clathrate hydrate, containing a similar full set of twelve pentagonal faces but also four hexagonal faces. Measured average cavity radii and unit cell characteristics for all three major cavity types are summarized in **Table 5-1**.^{12,94,97,99} Thermodynamic stability of the clathrate hydrate crystal determines the preferential formation of either the type II or type I structure. Typically, the type II structure will result from enclathration of guest molecules too large to occupy the tetrakaidecahedral cavities of the type I structure. In such cases, stability of the hydrate may require the presence of a help gas occupying the smaller dodecahedral cavities. Under high pressures of very small hydrate forming molecules, such as krypton and argon, and even nitrogen, a type II clathrate hydrate will form. The ability of hydrate former to stabilize the type I or the type II structure depends on both the size and shape of the guest molecule, and must be determined empirically, or by thorough molecular dynamics calculations.

Over the past few decades there have been many additions to the list of known hydrate forming molecules. **Figure 5-3** provides a list of some of the more commonly

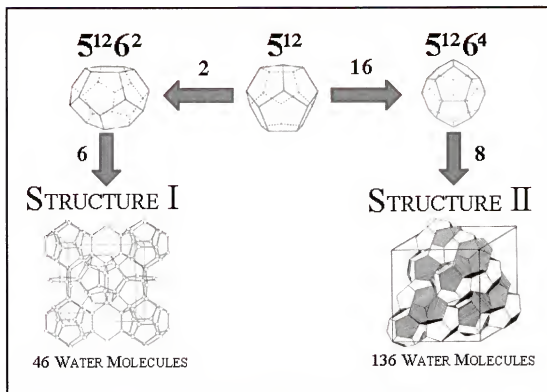


Figure 5-2. Clathrate hydrates are crystalline substances in which the hydrogen bonding of water molecules forms large, distinct cages. Both the type I and the type II structures contain dodecahedral cages and a cavity of a larger inner diameter.⁹²

known clathrate hydrate guest molecules that suggests the ranges of sizes and geometries possible for hydrate formers. In addition, **Figure 5-3** also indicates that in some circumstances the guest preferentially occupies one of the cavity types available in a given hydrate structure. This preferential occupation of cavities can be useful when cage occupancies are to be determined. For example, we know that molecules of diameters in the range up to about 5.0 Å fit easily into even the smaller dodecahedral cavities and therefore will occupy both cavity types available. Type I hydrate-directing molecules of the range 5.0 to 5.6 Å, however, are expected to occupy primarily the tetrakaidecahedral,

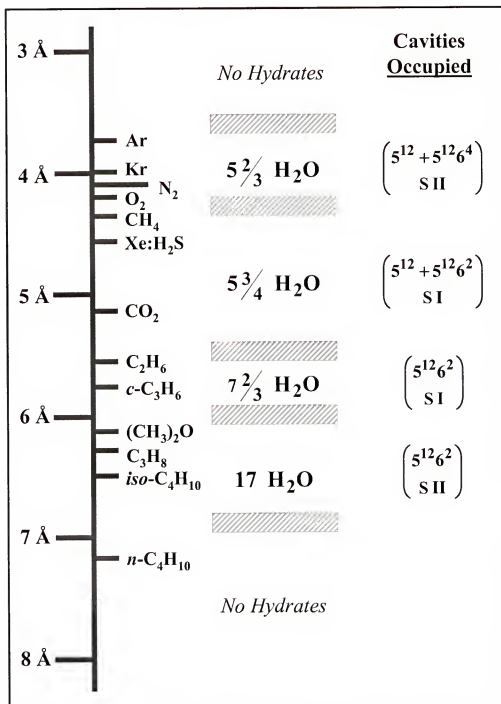


Figure 5-3. Clathrate hydrate forming capabilities of selected gases. Average van der Waals diameters are presented to the left side of the figure; the hydration numbers (center) are also denoted. Cavity occupation by the specified guest molecule is presented on the far right side of the figure. (Adapted from Ref. 42)

and not the dodecahedral, cavities. Thus, it becomes possible to determine the occupancy of the large cages directly through bulk physical techniques (such as isotherm and gas uptake measurements).

In comparison to the H-O-H bond angles of normal I_h ice, the pentagonal and hexagonal lattice arrangements of the clathrate hydrate structures permit H-O-H bond angles closer to the ideal 109.5° of a tetrahedral arrangement.⁹² The solid water structure of a clathrate hydrate should, therefore, be more stable than that of normal I_h ice. The clathrate hydrate, however, cannot exist as a pure $(\text{H}_2\text{O})_n$ lattice because the strong attractive hydrogen-bonding forces between opposing walls of each individual cavity cause the structure to buckle and collapse. The diameter of even the smallest of the cavities, the dodecahedron, is large enough that the masses of the water molecules themselves are insufficient to prevent the collapse of the structure.^{42,92} To stabilize the cage, occupation of the void by a small, relatively nonpolar guest molecule is required. The size and geometry of the guest molecule, rather than its propensity to form polar or hydrogen bonds with the lattice, prevents the cavity from collapsing.⁹¹

Thermodynamics of Gas Clathrate Hydrates

Thermodynamic expressions governing the equilibrium structure of gas clathrate hydrates will be discussed in this section. Recall that the ideal compositions were presented in **Table 5-1** and additionally in **Figure 5-3**.⁴² Typically the simple clathrates hydrates typically have higher host:guest ratios than would be expected assuming ideal

Table 5-2. Occupancies of the Cavities of Type I Simple Clathrate Hydrates, at the Dissociation Pressure and 0 °C, as Calculated Through Both Experiment and Theory.⁹⁹

Gas	θ_S	θ_L	θ_S/θ_L
H ₂ S	0.940	0.940	1.00
Xe	0.651	0.966	0.67
SO ₂	0.255	0.974	0.26
Cl ₂	0.140	0.975	0.14
CH ₃ Cl	0.052	0.976	0.053
CH ₃ Br	0.0090	0.976	0.009
CHClF ₂	0.0050	0.976	0.005

composition. Expressions for changes in the enthalpy and the entropy of the gas clathrate hydrates of either the type I or type II varieties can be written as functions of fractional occupancy, θ_i , for each cage of type i . The fractional occupancy is defined as the ratio of the number of occupied cages to the number of theoretically available cages based on the ideal hydrate composition. Typically, the fractional occupancies for the small and large cavities are denoted θ_S and θ_L , respectively. The values of θ_S and θ_L are rarely equivalent, and therefore, are treated as independent variables. The occupancy of each type of cavity is highly sensitive to the equilibrium conditions. For example, under moderate pressures (a few atmospheres) the dodecahedral cavities of the type I xenon hydrate can have fractional occupancies in the range 0.7 to 0.9.^{24,42,47} Fractional occupancies for selected simple clathrate hydrates of the type I variety are enumerated in **Table 5-2** for conditions of 273 K and the equilibrium pressure (*i.e.*, dissociation pressure) P_0 at that temperature.⁹⁹ At pressure P_0 , equilibrium exists between ice and crystalline clathrates hydrate.

As discussed earlier in this chapter, occupation of an individual (H₂O)_{*n*} cage by a small nonpolar guest molecule is necessary to stabilize the structure. The clathrate

hydrate unit cell, however, consists of a number of interlocking cages, sharing either edges (or vertices) and faces with a number of surrounding cages. A hydrate unit cell having a certain number of unoccupied cavities may still be thermodynamically stable. This then, is the reason why θ_i values may vary significantly between two or more different types of cages in the same clathrate hydrate.^{24,47,99} **Table 5-2** provides additional occupancy values. Conventional methods such as gas uptake measurements cannot generally be used to determine thermodynamic or structural characteristics of the small and large cages independently. Very few analytical techniques are capable of providing values for θ_s and θ_L independently. Selective enclathration of guest molecules, however, can be used to modify the gas uptake experiment, for example, so that an individual occupancy, θ_s or θ_L can be determined.^{100,101} Barrer and Edge¹⁰⁰ selectively filled the hexakaidecahedral cavities of the type II hydrate with chloroform. They then monitored the absorption of smaller, monatomic gas species (such as argon or krypton) into the dodecahedral cavities. Values determined for θ_s depended, of course, on the assumption that occupation of the large cages with chloroform was fairly complete. Similarly, Dharmawardhana *et al.*,¹⁰² determined values for θ_L for selected mixed clathrate hydrates by using a variety of guest molecules assumed to be too large to occupy any of the small cavities.

When the guest molecule necessarily occupies both the large and small cavities to some extent, conventional techniques will not be applicable. Under these conditions, direct measurements of fractional occupancy values are possible using NMR techniques. Ripmeester and Davison,^{24,42} first employed ¹²⁹Xe NMR signal intensities to obtain

relative cavity occupancies for the small and large cages of the type I xenon clathrate deuteriohydrate at 275 K, as was shown previously in **Figure 2-1**. Recall that the highly polarizable electron cloud of atomic xenon leads to a confinement-dependent shielding of the nucleus, which can be observed as a shift of the ^{129}Xe NMR resonance frequency. The shift in the resonance frequency for ^{129}Xe enclathrated into the different cavity types is greater than the shift anisotropy and other line broadening contributions, so that the ^{129}Xe NMR lines are completely resolved at high magnetic field. Based on the signals integrations, the ratio of occupied large cages to small cages was found to be 3.90 ± 0.10 , showing a clear deviation from the ideal ratio of 3.00:1. This value of θ_L/θ_S corresponds well to those reported elsewhere for identical experimental conditions.^{24,47,99}

Applying the Solid-Solution Model to Gas Clathrate Hydrate Thermodynamics

The xenon and krypton clathrate hydrates provide the simplest examples of the type I and type II hydrate structures, respectively.¹⁰³ As a matter of clathrate stability, enclathration of the guest species causes only negligible distortion of the cavity dimensions from those of a pure $(\text{H}_2\text{O})_n$ lattice. Because of the snug fit of the enclathrated species, guest molecules experience only small translational displacements. The xenon clathrates hydrate exhibits a relatively low dissociation pressures (1.55 bar at 273 K),¹² and at such pressures, compressibility of the hydrate forming gas effects may be ignored. That is, thermodynamic properties and formation kinetics of the xenon clathrate hydrate may be related directly to the pressure of xenon. For monitoring the formation of clathrate hydrates *in situ*, low dissociation pressures mean that measurable quantities of

Table 5-3. Ratios of Molecular Diameters To Cavity Diameters for Selected Type I Gas Hydrate-Forming Molecules.⁴²

Molecule	Guest Diameter (Å)	Molecular Diameter/Cavity Diameter For Each Cavity			
		Structure I		Structure II	
		5 ¹²	5 ¹² 6 ²	5 ¹²	5 ¹² 6 ⁴
Ar	3.8	0.772	0.660	0.775	0.599
Kr	4.0	0.813	0.694	0.816	0.619
N ₂	4.1	0.833	0.712	0.836	0.634
O ₂	4.2	0.853	0.729	0.856	0.649
<i>CH₄</i>	<i>4.36</i>	<i>0.886</i>	<i>0.757</i>	<i>0.889</i>	<i>0.675</i>
<i>Xe</i>	<i>4.58</i>	<i>0.931</i>	<i>0.795</i>	<i>0.934</i>	<i>0.708</i>
H ₂ S	4.58	0.931	0.795	0.934	0.708
CO ₂	5.12	1.041	0.889	1.044	0.792

the hydrate can be formed without resorting to the use of high-pressure reaction vessels.⁴² Studies of the xenon clathrate hydrate have additional advantages. Direct analogies may be drawn between xenon and methane in terms of structural symmetry and van der Waals diameters. Both xenon and methane are nonpolar spherically shaped species, with van der Waals radii of 4.58 Å and 4.36 Å, respectively. **Table 5-3** summarizes the relationship between the van der Waals diameter and the cavity diameter for selected hydrate formers and their associated type I and type II hydrate structures. Based on these relationships, expressions modeling the thermodynamic properties of the xenon clathrate hydrate, and as well any proposed formation mechanisms, are expected to be directly applicable to the natural gas hydrate.⁴²

The fractional occupancy, θ , for each cavity has been found to be highly dependent on the applied pressure of the guest species. In most cases, particularly that of xenon, compressibility factors of the guest molecules may be neglected and the fugacity,

f_i may be simplified to the equilibrium pressure, P , at relatively low pressures. Under equilibrium conditions, a solid-solution model can be applied for the description of the xenon and krypton hydrate clathrates.^{99,103}

In the solid-solution model it is assumed that the degree of occupancy of each cage of type i , signified by θ_i , is directly proportional to the fugacity, f_i , of the gas species.²⁴ With the simplification that $f \approx P$, θ_i can be expressed in the form of the Langmuir equation,²⁴

$$\theta_i = \frac{C_i P}{1 + C_i P}, \quad (5-1)$$

where C_i is the Langmuir constant of each type i cavity, and P is the applied equilibrium pressure. The second assumption relates the potential energy of the water molecules in the hydrate lattice directly to the degrees of occupancy of both the small and large cages.²⁴ If guest-guest interactions and lattice distortions away from cubic symmetry are negligible, the chemical potential of the type I hydrate is given by equation 5-2,^{12,42}

$$\mu_w(h) - \mu_w^O(h) = \frac{kT}{23} [\ln(1 - \theta_s) + 3 \ln(1 - \theta_L)], \quad (5-2)$$

where $\mu_w^O(h)$ is the chemical potential of the clathrate lattice in the absence of guest molecules. The factor of 3 on the term $3 \ln(1 - \theta_L)$ arises from the occurrence of three

times as many tetrakaidecahedral cavities as dodecahedral cavities in the type I clathrate hydrate unit cell, while the factor of 1/23 is to account for the fact that only 23 of the 46 water molecules the unit cell are associated with the cage structures entrapping the 4 total guest molecules being considered in equation 5-2. Similarly, for the type II structure, where there are twice the number of dodecahedral as hexakaidecahedral cavities, and 17 of the 136 water molecules in the unit cell are involved in the cage structures entrapping the 3 guest molecules being considered in equation 5-3, the chemical potential for the hydrate may be estimated by^{12,42}

$$\mu_w(h) - \mu_w^O(h) = \frac{kT}{17} [2 \ln(1 - \theta_s) + \ln(1 - \theta_L)]. \quad (5-3)$$

Combining equations 5-2 and 5-3 with the Langmuir equations for the small and large cavities, the chemical potentials of the type I and type II clathrate hydrates may be expressed by equations 5-4 and 5-5,

$$\mu_w(I) - \mu_w^O(I) = \frac{kT}{23} [\ln((1 + C_s(I)P) + 3 \ln(1 + C_L(I)P))], \quad (5-4)$$

$$\mu_w(II) - \mu_w^O(II) = \frac{kT}{17} [2 \ln((1 + C_s(II)P) + \ln(1 + C_L(II)P))], \quad (5-5)$$

where $C_i(I)$ and $C_i(II)$ represent the Langmuir constants for the cavity structure i of each hydrate of the type I and II varieties, respectively.^{12,24,42,104}

Once accurate values for θ_s and θ_L have been determined, equilibrium constants for each cavity type, K_s and K_L , may also be determined using equations 5-6 and 5-7,¹⁰⁰

$$K_s = \frac{1}{P} \left(\frac{\theta_s}{1 - \theta_s} \right), \quad (5-6)$$

$$K_L = \frac{1}{P} \left(\frac{\theta_L}{1 - \theta_L} \right). \quad (5-7)$$

Since the type I hydrate unit cell has a 3:1 ratio of small (5^{12}) to large ($5^{12}6^2$) cavities, the total quantity of guest molecules enclathrated and the quantity of ice available to be enclathrated can be determined from Langmuir isotherm adsorption experiments. From these, one can determine overall occupancy for the gas hydrate, through equation 5-8:²⁴

$$\frac{\text{Equilibrium Amount of Inert Gas Sorbed}}{\text{Theoretical Maximum Sorption of Inert Gas}} = \frac{1}{4}\theta_s + \frac{3}{4}\theta_L \quad (5-8)$$

Inserting equations 5-6 and 5-7 results in equation 5-9,

$$\frac{\text{Equilibrium Amount of Inert Gas Sorbed}}{\text{Theoretical Maximum Sorption of Inert Gas}} = \frac{P}{4} \left(\frac{K_s}{1 + K_s P} + \frac{3K_L}{1 + K_L P} \right), \quad (5-9)$$

which relates the occupancy of the hydrate to the equilibrium pressure of the clathrate, a directly measurable quantity.²⁴

Accurate values for the fractional occupancies for the small and large cavities are necessary for determining of the hydration numbers, n_h , for each clathrate hydrate structure, type I or type II. The hydration number is perhaps most useful for the simple hydrates, where a single hydrate forming molecule is being considered.¹⁰⁵ For the type I clathrate hydrate, there are 23 individual water molecules associated with the enclathration of $3\theta_L$ and θ_S guest molecules, so that using **Table 5-2**, the hydration number may be determined by equation 5-10,

$$n_h = \frac{23}{3\theta_L + \theta_S}, \quad (5-10)$$

For the type II clathrate hydrate structure, there are 17 water molecules associated with the enclathration of θ_L and $2\theta_S$ guest molecules, providing a hydration number,

$$n_h = \frac{17}{\theta_L + 2\theta_S}. \quad (5-11)$$

Thus, for mixed or double hydrate clathrates, determination of the hydration number can only be accomplished if accurate occupancies for both the small and large cages are known.

Summary

In the past few decades, for a variety of reasons alluded to earlier in this chapter, interest in the thermodynamics and kinetics of formation of methane gas hydrate has grown tremendously. None of the techniques exploited prior to the use ^{129}Xe NMR, and perhaps more recently, Raman spectroscopy, have been able to elucidate fully the details of the mechanisms of clathrate hydrate formation. Only NMR and Raman spectroscopies have allowed for the determination of relative guest-occupancies of the cavities, and as well the monitoring of the enclathrations of xenon atoms into the small and large cavities of clathrate hydrates *in situ*.

The type I clathrate hydrate, having dodecahedral and tetrakaidecahedral cavities, can accommodate guest molecules with diameters up to 5.8 Å. Both xenon and methane, having similar diameters, occupy the small and large cavities of the type I hydrate. With similarities in size and symmetry of the guest species, the xenon clathrate hydrate serves as an appropriate model for the natural gas hydrate. In the latter case, the investigator can take advantage of the high sensitivity of the ^{129}Xe NMR chemical shift to allow full resolution of the resonances corresponding to occupied large and small cavities. Based on the ^{129}Xe NMR signals integrations, the ratio of occupied large cages to small cages was found to be 3.90 ± 0.10 . With the signal enhancement afforded by SEOP enhanced ^{129}Xe NMR, the changes in the occupancy ratios can be monitored in real time throughout the formation of the clathrate hydrate to determine how the values deviate from the ideal ratio of 3.00:1. ^{129}Xe NMR may also be used to investigate type II clathrate hydrates in which xenon primarily occupies the dodecahedral cavities. The type II clathrate hydrate

maintains sixteen dodecahedral cavities and eight hexakaidecahedral cavities, where each of the latter is larger than a tetrakaidecahedral cavity, and a ^{129}Xe NMR resonance even further upfield is expected.

In Chapter 6 kinetics schemes relating to the formation of the simple type I clathrate will be discussed. Several schemes previously suggested will be addressed, as well as two original proposed mechanisms. The mechanisms are consistent with the time-resolved ^{129}Xe NMR data available in Chapter 7. Finally, spin-polarized ^{129}Xe has been used to monitor the enclathration of xenon into a pre-initiated type II structure, with either SF_6 or acetone- d_6 as the primary large cavity occupant. The type I and type II clathrate hydrate experiments will be used to explore the rates of xenon enclathration, and guest-host lattice dynamics as functions of temperature and of the size and symmetry large cavity occupant.

CHAPTER 6

PROPOSED MECHANISMS AND KINETICS OF TYPE I XENON CLATHRATE HYDRATE FORMATION

Introduction

The processes of classification and characterization of the clathrate hydrates, and of development of applications for these nonstoichiometric compounds, occurred in three stages.⁴² Initially, research addressed primarily determination of the conditions leading to the synthesis and the formation of clathrate hydrates through precise control of the various laboratory conditions. Characterizations of these manufactured hydrates were often speculative, so that reported ideal compositions varied significantly with minor differences in the laboratory conditions. In the second wave of research, practical applications for clathrate hydrates became most important. Precise determination of the composition of the clathrates became necessary, and characterization techniques greatly improved. The third wave of research, partly resulting from an increased demand to explore other fossil fuel resources, addresses the kinetics of formation of clathrate hydrates, and as well on the possible inhibition under conditions where their formation would be undesirable. A number of kinetics schemes have been proposed to describe the formation of simple type I clathrate hydrates. To date, however, no single model has

sufficiently explained all of the characteristics of hydrate crystal formations that have been observed experimentally.

Despite differences observed for the rates of nucleation and of crystal growth between clathrate hydrates formed on ice surfaces and in supercooled liquid water, the mechanism of nucleation for both conditions is expected to be similar to that for the nucleation of sugar crystals in supersaturated solutions in the absence of seed crystals.⁴² The development of clathrate hydrate crystals involves the initial formation of only tens to hundreds of nucleation sites. This small number of sites makes the nucleation of hydrate crystals a microscopic process that is difficult to observe experimentally.⁴² The rapid formation and transformation of intermediate species, and the short time dependence of the formation kinetics, further complicate determination of the rates and characteristics of clathrate hydrate nucleation. Experimental data detailing nucleation is scarce, and so, models of this stage of hydrate formation have often been speculative. Understanding the occurrences of nucleation sites during the induction period of the gas hydrate clathrate formation is essential for development of an all-inclusive formation kinetics scheme.

Proposed Models for Gas Clathrate Hydrate Nucleation

Induction Periods Observed for Selected Simple Gas Hydrate Clathrates

Barrer and Edge^{42,100} pioneered pressure-time dependence measurements of the conversion of ice crystals into gas clathrate hydrates. The experimental apparatus of

Barrer and Edge¹⁰⁰ continuously ground the ice/hydrate mixture in order to provide fresh surfaces throughout the duration of the experiment. Their meticulously taken data suggested that argon and xenon formed simple gas clathrate hydrates formed rapidly, with little or no observable induction periods. The smaller noble gas, krypton, however, exhibited a lengthy period during which the rate of enclathration of gas was nearly negligible. This long induction period noted for the simple krypton clathrate hydrate was attributed to slow formation of nucleation sites, a result of the low stability of these clathrate precursors afforded by the small krypton atoms. Rapid hydrate crystallization following the induction period slowed only when the availability of fresh ice surfaces was exhausted. From the direct comparison of the noble gases argon, xenon, and krypton, Barrer and Edge¹⁰⁰ proposed that the length of the induction period, and therefore the stability of the clathrate precursor, depended strongly on the van der Waals diameter of the guest molecule.

Although in general, this proposed explanation for the observed characteristics of the induction period has indeed proven to be correct, it should be noted that the argon and xenon clathrate hydrates are structure I hydrates, and the krypton hydrate exhibits structure II. Slight differences in molecular size can also determine if a structure I or a structure II hydrate will form. For example,⁴² xenon has a van der Waals diameter within 0.5 % of the average free diameter of the regular dodecahedral cavity, and is enclathrated into a type I simple clathrate hydrate structure. Krypton, a slightly smaller guest molecule (4.04 Å diameter), more effectively stabilizes the slightly distorted dodecahedral cages of the *type II* clathrate. The research of Barrer and Edge¹⁰⁰ demonstrated that krypton,

forming its type II structure on the surfaces of ice crystals, can have an induction period duration of over an hour, whereas xenon begins more rapid crystal growth of the type I clathrate hydrate immediately following exposure. Similar results presented by Falabella,^{106,107} in 1975, also indicated clear and measurable induction periods for certain guest molecules, notably methane and krypton.

Even after fully dissociating the guest molecules from the host lattice (for example, by application of high vacuum), there is some residual crystal-like network in the liquid-water that remains for samples maintained below about 300 K.⁴² A second exposure of the ice to the hydrate-directing guest molecule demonstrates a reduction in the length of the induction period. The lingering existence of nucleation sites gives subsequent exposures to the hydrate-former a head start on achieving the critical nucleation size necessary for beginning more rapid crystal growth. These “memory effects” observed in clathrate-hydrate systems were first noted in the temperature dependence studies of Makogon.¹⁰⁸ The molecular dynamic studies of Chen¹⁰⁹ confirmed Makogon’s observations, and Chen added the speculation that residual pentagonal and dodecahedral structures remained stable up to 315 K. Hydrate decompositions performed above this temperature indicated almost complete erosion of the residual network. Additional studies have confirmed the memory effect for a variety of hydrate systems, notably for the methane¹¹⁰ and carbon dioxide¹¹¹ simple clathrate hydrates. It is believed that research into the conditions allowing for the observed memory effect will lead to greater understanding of the nucleation of clathrate hydrate crystals.

The purpose of this research into the simple type I clathrate hydrates was to develop a more complete understanding of the formation kinetics using data acquired through monitoring the in situ formation of the type I xenon clathrate hydrate, by time-resolved SEOP enhanced ^{129}Xe NMR and pressure-time dependence measurements. The relevance of this research rests on the applicability of the kinetics model proposed for the formation of the xenon gas clathrate hydrate to that of the methane hydrate, that latter of which is of both ecological and industrial importance. Applicability of the model is expected given that methane and xenon are both spherically symmetric molecules with very similar van der Waals diameters, as **Table 5-3** previously indicated. Differences in the length of the induction period, and in the rates of larger crystal growth, will be highly dependent on even the minor differences between the two guest molecules. Still, the mechanism proposed for type I xenon clathrate hydrate formation is expected to be universally applicable to the formations of gas clathrate hydrates.

Differences in the Observed Induction Periods

With one approach, type I and type II clathrate hydrate structures may be distinguished using a description of how dodecahedral cavities are attached. That is, if adjacent dodecahedral cages share vertices, a type I structure will form; the sharing of faces will produce a type II clathrate hydrate.⁴² With this system of identification in mind, a model for the nucleation of clathrate hydrate crystals has been developed involving the formation of occupied dodecahedral cavities. For simple gas clathrate hydrates like those of xenon or of methane, occupied cavities will continue to form until a critical number of

sites is reached, necessary for more rapid crystal growth. As this critical number is achieved, the dodecahedral cages will reorient themselves to form macromolecular clusters that oscillate in their attachment of dodecahedron vertices or faces. Final determination as being of the hydrate as a structure I or as a structure II variety is dependent on the ability of the guest molecule to stabilize the larger cavities ($5^{12}6^2$ or $5^{12}6^4$) result through the attachment of dodecahedra.^{16,42} Ripmeester *et al.*¹⁶ had suggested, for example, that the stability of the $5^{12}6^2$ cavity occupied by methane was greater than for a $5^{12}6^4$ cavity occupied by the same guest, thus directing the formation of a type I methane gas clathrate hydrate. Having a similar van der Waals diameter, xenon also guides the formation of a type I clathrate hydrate. Because xenon is slightly larger than methane and more completely fills the cavities of dodecahedral and tetrakaidecahedral cavities,⁴² the resulting noble gas clathrate hydrate structure is more stable than that of the natural gas hydrate. As a result, formation of the xenon clathrate hydrate exhibits a measurably shorter induction period,^{16,42} and, as well, much lower dissociation pressures than its natural gas counterpart.

The stability of the clathrate hydrate depends on the amount of strain introduced through occupation of the cavities by guest molecules. Following the induction period, additional guest molecules will be enclathrated into both the small and large cavities.⁴² Thus, the rates of nucleation and of bulk crystal formation will be dependent on the amount of the strain resulting from the enclathration of guest species. Enclathration resulting in the formation of a stable clathrate hydrate structure requires a net dissipation of heat energy.

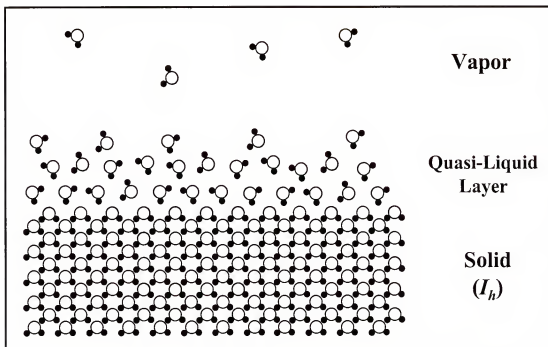


Figure 6-1. The quasi-liquid layer covers the surfaces of ice crystals and may be a few molecular layers to nanometers thick, depending on the temperature. Water molecules in this layer have mobility and hydrogen bonding characteristics similar to water molecules under bulk liquid conditions.

Modeling Gas Clathrate Hydrate Crystal Growth Following the Induction Period

It has been demonstrated^{25,42,100} that gas hydrate clathrates form on the surfaces of ice crystals much more rapidly than they form in supercooled water. Barrer and Edge¹⁰⁰ had postulated that the mechanism for crystal growth of clathrate hydrates on ice particles involved the transport of water molecules in the gas phase from one position to another on the surfaces of the ice crystals. Falabella,^{106,107} however, had noted that the rate of sublimation of water molecules from the ice surface was insufficient to sustain the observed rates of hydrate crystal growth. In recent years, new mechanisms for the formation of hydrate crystals involved the diffusion of water molecules across a quasi-

liquid layer maintained on the surfaces of ice crystals (**Figure 6-1**). The current understanding of the dynamics of water molecules on the surfaces of ice crystals is that the top layers of molecules exist in a *quasi-liquid* state. The thickness of this quasi-liquid layer is highly dependent on the temperature, and can be a few molecular layers to several angstroms thick. Water molecules in the quasi-liquid state exhibit much higher rates of diffusion than from other means that would accommodate the rates of hydrate crystal growth observed on the ice surfaces.

Hwang *et al.*¹¹² had monitored the formation of hydrates on the surfaces of melting ice crystals. Their data suggested that the surface of the melting ice provided an efficient template for the gas clathrate hydrate formation. As a protective film of clathrate hydrate formed on the ice crystal surfaces, a rapid decline in the rate of guest molecule enclathration was observed. This suggested that the thermodynamically stable gas hydrate clathrate retarded further melting of the ice. The researchers noted that proposed mechanisms for the hydrate formations observed might be specific to their experimental conditions and may not apply directly to crystal growth observed at much lower temperatures or in bulk water conditions.

Barrer and Ruzicka^{113,114} studied the rate of crystal growth of double hydrates, using argon as the help gas to occupy the smaller dodecahedral cavities. The rate expression applies directly to clathrate hydrate crystallizations performed in supercooled water or on the surfaces of ice crystals. The formation of the clathrate hydrate can be generalized in terms of the transport of guest molecules from bulk medium to the H₂O-

clathrate interface. The model evolves through alteration of Fick's second law to produce equation 6-1,

$$\frac{dn}{dt} = AD \frac{\Delta C}{\delta}, \quad (6-1)$$

where dn/dt represents the rate of hydrate growth, A is the surface area of the ice particle, D is the diffusion coefficient of the guest through the bulk medium, ΔC is the difference in concentration of the guest species across the boundary layer, and δ is the thickness of the quasi-liquid layer.

Miller and Smythe¹¹⁵ obtained kinetics data on formation of the carbon dioxide clathrate hydrate. The isothermal hydrate growth rate was determined by monitoring the decrease in the pressure of carbon dioxide as a function of time, and the rate of formation of hydrate was modeled as a simple exponential. The solution with respect to time for this rate expression provides the time dependence of the carbon dioxide pressure as

$$\ln \left[\frac{P_o - P_\infty}{P(t) - P_\infty} \right] = kt, \quad (6-2)$$

where P_o , P_∞ , and $P(t)$ denote the initial pressure, the equilibrium pressure, and the pressure at time t (in units of hours), respectively. Obviously, neither of these expressions includes mathematical modeling of clathrate hydrate nucleation.

By neglecting consideration of the induction period, Falabella^{42,106,107} was able to provide a second order kinetics model that satisfactorily fit both his data and data that had been published earlier by Barrer and Edge.^{42,100} The kinetics scheme is based upon isothermal-isobaric fractional conversion of ice crystals, and determines the mole fraction of ice that has been converted to hydrate, denoted by X . For the constant pressure experiment, we have

$$\frac{d(1-X)}{dt} = -k(1-X)^2, \quad (6-3)$$

which has the following general solution for the mole fraction X :

$$\frac{X}{(1-X)} = -kt. \quad (6-4)$$

Incorporating the factor $(P - P_\infty)^{1/2}$ into expression 6-4 can accommodate the variations of pressure with the reaction time. The resulting model is expressed as equation 6-5,

$$\frac{d(1-X)}{dt} = -k(1-X)^2(P(t) - P_\infty)^{1/2}, \quad (6-5)$$

where P is the time-dependent value for the pressure of the hydrate former. As mentioned previously, these models have not addressed clathrate nucleation, which in many cases

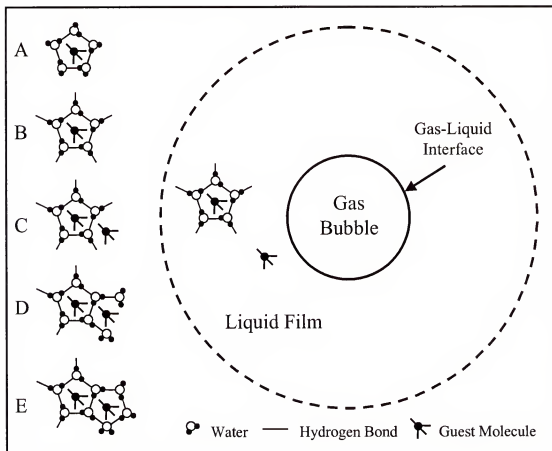


Figure 6-2. Above is depicted a pictorial representation of the Ullerich-Selim-Sloan kinetics scheme, which models clathrate hydrate formation as a four-step scheme, involving three independent rate constants, k_1 , k_2 , and k_3 .¹¹⁶

cannot be neglected. A kinetic scheme considering all stages of clathrate hydrate formation on a molecular level would be necessary for development of a universally applicable model.

Modeling Gas Clathrate Hydrate Formations at the Molecular Level

Development of much more complex, multi-step schemes has been necessary in order to address the nucleation of clathrate hydrate crystals and to account for the more

subtle nuances observed in the kinetics data. In 1987, Ullerich, Selim and Sloan¹¹⁶ proposed a four-step mechanism for hydrates at a gas-liquid-solid interface as depicted in **Figure 6-2**. Application of the model begins at the gas-liquid interface where a number of nucleation sites, denoted by the quantity A , have already formed at the interface. The experimental data provided to support the following model was acquired for hydrate growth in the liquid state. The model should, however, apply as well to the formation of hydrate on ice surfaces, since the exchange of guest molecules at the quasi-liquid layer interface can just as easily be described as a gas-liquid equilibrium.

The first step of the kinetics scheme involves diffusion of water molecules to sites of A , and, subsequently, reorientation to form additional partial cages in the liquid or quasi-liquid interface. Water molecules continue to arrange until more fully enclosed structures, B , form. This process occurs under rate constant k_1 , so that



In the second step, guest molecules adsorb onto the surfaces of these new structures, and the water molecules of the cages reorient rapidly to entrap the guests, forming the structures C . Once the guest molecule is secured, the water molecules of C arrange themselves more slowly to form a more complete cage D , which develops under rate the constant k_2 as



With the diffusion of a few additional water molecules to D , the guest molecule becomes fully enclathrated and the structure E , a tetrakaidecahedral, hexakaidecahedral or dodecahedral cavity, results. Final enclathration proceeds under rate constant k_3 as



The mechanism provides the following set of expressions for the formation of the hydrate clathrate using the concentrations of species A , B , C , D , and E :

$$\frac{d[A]}{dt} = -k_1[A] \quad (6-9)$$

$$\frac{d[B]}{dt} = k_1[A] - k_2[B] \quad (6-10)$$

$$\frac{d[D]}{dt} = k_2[B] - k_3[D] \quad (6-11)$$

$$\frac{d[E]}{dt} = k_3[D] - k_1[E] \quad (6-12)$$

Development of multi-step kinetic schemes, with attention paid to hydrate nucleation, have become necessary, particularly as detection methods have become more capable of observing these kinetic processes on a microscopic level.

There have been, of course, other attempts to model the formation of simple gas clathrate hydrates on molecular levels. For example, the scheme proposed by Vsyniauskas, Bishnoi, *et al.*¹¹⁷ was similar to that of Ullrich, Selim and Sloan¹¹⁶ but simplified clathrate hydrate formation into a two-step process. A multi-step scheme

proposed by Englezos, *et al.*¹¹⁸ attempted to address all aspects of clathrate crystal formation. In an attempt to simplify the expressions, vigorous shaking of the reaction vessel was employed so that the rate of diffusion of guest molecules to the gas-liquid interface could be ignored. Additionally, the model proposed by Englezos, *et al.*¹¹⁸ suggested that for a mixture of hydrate forming guest molecules, the rate of clathrate formation could be represented as a linear combination of the rates of formation of the hydrates of each gas. Experimental conditions provided time-resolved pressure measurements that could be fit well to a single exponential rate expression.

The Use SEOP Enhanced ^{129}Xe NMR to Monitor Clathrate Hydrate Formation

In 1995, Pietraß *et al.*²⁵ first monitored the formation of the simple xenon type I clathrate deuteriohydrate by time-resolved SEOP enhanced ^{129}Xe NMR. The advantage to using time-resolved ^{129}Xe NMR is that it allows determination of the occupancy ratios for each cage type, as a function of the reaction time. Type I xenon clathrate hydrates were formed on the surfaces of ice crystals at reaction temperatures in the range 195 to 233 K. SEOP enhanced ^{129}Xe was collected in a sidearm of the NMR tube, allowing the ice to be maintained at the desired sample equilibrium temperature. Sublimation of xenon from the sidearm supplied gas to the undisturbed finely powdered ice. An excess of xenon gas throughout the formation process was assumed.

The scheme used to describe their observations neglected the nucleation process. This decision to do so was based, in part, on the experiments of Barrer and Edge,¹⁰⁰ and of Falabella,^{106,107} who had reported previously that the formation of the type I xenon

clathrate hydrate exhibited no measurable induction period. The kinetics of hydrate formation could then be simplified to a two-step process. In the first step, the gas is adsorbed to the surfaces of the ice crystals, and a number of water molecules diffuse to the adsorption site to entrap the xenon atom in a partial cage. The concentration of the entrapped species is given by Xe_{ads} . Xenon adsorption is a reversible process, with two independent rate constants for the adsorption and dissociation processes, given by k_{ads} and k_d , respectively.



The second step in xenon enclathration occurs when a critical value for the Xe_{ads} sites is achieved. At that time, irreversible enclathration of the adsorbed species occurs through reorientation of water molecules under the rate constant k , to form Xe_{Clath} .



A stoichiometric excess of available Xe would justify the assumption that Xe_{ads} remained constant throughout the experiment and the concentration of the intermediate species was dependent solely on the pressure of xenon. Thus, simplifying relationships 6-15 and 6-16 may be employed.

$$\frac{d[Xe_{ads}]}{dt} = 0 \quad (6-15)$$

$$[Xe_{ads}] = \frac{k_{ads}}{k + k_d} [Xe] \quad (6-16)$$

Irreversible enclathration of the intermediate species, Xe_{ads} , provides the direct proportionality of the rate of enclathration to the ambient xenon pressure,

$$\frac{d[Xe_{Clath}]}{dt} = k[Xe_{ads}] = \frac{k \cdot k_{ads}}{k + k_d} [Xe] = k_{eff} [Xe], \quad (6-17)$$

for which an effective rate constant, k_{eff} , may be defined.

Since the rate of xenon enclathration was determined by monitoring the SEOP enhanced ^{129}Xe NMR signals, fitting the NMR data to the kinetics model required that the time-dependence of the depletion of the ^{129}Xe magnetization be considered. The ^{129}Xe NMR signals decay in accordance with spin lattice relaxation, and through successive NMR rf pulses. Pietraß *et al.*²⁵ adjusted for these sources of spin polarization depletion of ^{129}Xe by utilizing an overall time constant T_{kill} , so that the time-dependent integrated signal intensity for xenon-occupied cavities is represented by an exponential of $-t/T_{kill}$, where t is the time of the spectrum acquisition. Pietraß *et al.*²⁵ were able to fit data at three temperatures, 195, 217, and 233 K, and to determine effective rate constants for small and large cage signals at each of these temperatures. At all temperatures, the effective rate constants, k_{eff} , and overall time constants, T_{kill} , were distinctly different for

enclathration of xenon into the small and into the large cavities. In addition, a plot of the ratio of ^{129}Xe NMR signals for the large to small cavities revealed a value less than 3.0 in the early stages of clathrate hydrate formation observed at 233 K. This would suggest that a surplus of occupied small cavities at the onset of clathrate crystallization.

Summary of Prior Work

At present, detailed thermodynamic characteristics are available for clathrate hydrates of both the type I and type II varieties, and using a variety of guest molecules. The surface has only been scratched, however, as to the kinetics of their formations and decompositions. A mechanism describing the formation of clathrate hydrates will only be universally applicable when both the characteristics of hydrate nucleation and of more rapid growth of the crystals have been accommodated. Presented in the earlier sections of this chapter were several kinetics schemes that are directly applicable to the formation of clathrate hydrates on the surfaces of ice crystals. In the final sections, two original mechanistic schemes are introduced.

This research has undertaken the task of elucidating further the hydrate formation mechanism through the combination of pressure measurements and time-resolved SEOP enhanced ^{129}Xe NMR. Pietraß *et al.*²⁵ presented preliminary work that monitored the formations of the type I simple xenon clathrate hydrate at selected temperatures. In their proposed formation mechanism, the full schematic of which is provided in **Figure 6-3**, adsorption of xenon to the surface of the ice crystal is included. The slow accumulation

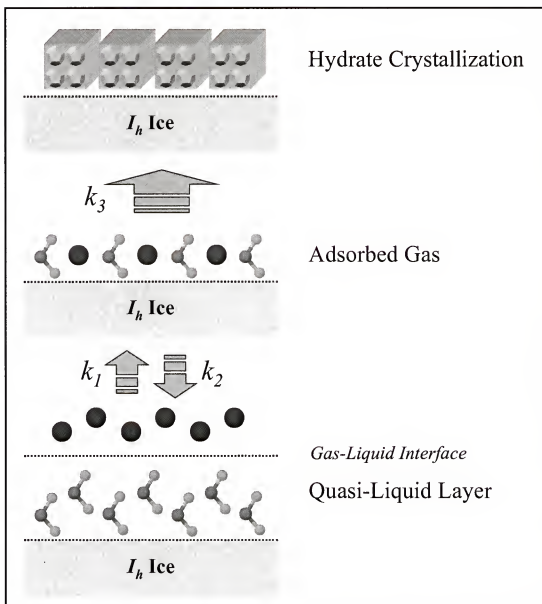


Figure 6-3. Pictorial representation of the kinetics scheme proposed by Pietrass and co-workers.²⁵ The first step is the reversible formation of an intermediate species, Xe_{ads} , the concentration of which depends solely on the Xe pressure. The second step involved an irreversible enclathration to form Xe_{Clath} .

of nucleation sites, however, is neglected in the development of the kinetics expressions.

The time required to achieve a critical number of nucleation sites for the simple type I

xenon hydrate is much reduced compared to that of krypton. A measurable induction period, however, is evident from the time-resolved SEOP enhanced ^{129}Xe NMR data.

Pietraß *et al.*²⁵ also modeled the decay of the ^{129}Xe NMR signal using the single exponential of the time constant, T_{kill} . From the original data acquired for this thesis, as will be presented in subsequent chapters, the T_I for xenon enclathrated in the deuteriohydrate was determined to be on the scale of tens of minutes, far longer than the time required for hydrate formation to achieve completion under experimental conditions similar to those of Pietraß and co-workers.²⁵ Therefore, the dominant mechanism for depletion of the ^{129}Xe polarization reservoir would appear to be successive NMR rf pulses, and not through natural relaxation processes.

On a final note concerning prior work on the type I xenon deuteriohydrates,^{25,29} the plots of the ratio of large cage signals to those of the small cages revealed values less than 3.0 at early reaction times. Several integration ratios were determined to be below that which was expected based on the clathrate hydrate ideal composition. In the previous studies,^{25,29} however, the occupancy ratios were determined at stages in the reaction at which the signal intensities attributed to enclathrated xenon could not be measured reliably. In those first acquired spectra, integrations of the signals corresponding to enclathrated xenon are subject to phasing errors. This fact was not hidden, but actually discussed by the investigators.²⁵ Because the specific occupancy ratios less than 3.0 may have been determined under unreliable conditions, it may be safer to cite the steady increases in the occupancy ratios in the early portions of induction as “proof” of the antecedent enclathration of xenon into dodecahedral cavities. In combination with the

experiments presented here, an attempt has been made to improve the results of prior reports and to confirm or refute ambiguous speculations as to the nature of the nucleation process of clathrate hydrate formation.

In the sections which follow, two schemes are proposed in attempts to more accurately describe the formation of the simple type I gas clathrate hydrate, and inevitably to fit each model to the available time-resolved SEOP ^{129}Xe NMR data. Attempts to directly model the data revealed that determination of one of the remaining independent variables was necessary for the fitting of the model to provide a unique set of solutions for each set of experimental conditions. The experimental system could be redesigned, for example, to monitor the pressure simultaneously with the acquisition of ^{129}Xe NMR spectra, which would remove the piecewise modeling of the sublimation and consumption of xenon gas through enclathration processes.

Original Proposed Kinetics Models for the Formation of the Type I Clathrate Hydrate

Model I: Interdependency of Cavity Formation

In accordance with the microscopic mechanism of type I clathrate hydrate nucleation proposed by Sloan and Fleyfel¹¹⁹ and others,^{42,113-115} it will be assumed in the development of the original scheme that the basic building block of each hydrate structure is the formation of an occupied dodecahedral (5^{12}) cavity. The reported ratio of the van der Waals diameter of the xenon atom to dodecahedral cavity diameter in the type I structure is 0.931 (**Table 5-3**), suggesting than an occupied dodecahedral cage provides

the most stable structure possible as a nucleation center. In the formulation of this kinetic model it is also hypothesized that the existence of one or more nearby 5^{12} cages stabilizes the formation of the tetrakaidecahedral ($5^{12}6^2$) cavity. In the crystal growth phase of the kinetic mechanism, the formation of additional small cages will be proportional to the density of the larger cages, and similarly, the formation of additional larger cages is proportional to the density of the smaller cages. This simple autocatalytic mechanism incorporates the following observations and considerations:

1. The primary nucleation step proceeds according to a pseudo first order rate law with rate constant k_3 . Growth of the gas hydrate crystals can only occur subsequent to the formation of a critical number of nucleation sites.
2. The *S*-shaped time dependence observed for the gas uptake experiment, which will be discussed in Chapter 7, is indicative of a positive feedback (i.e. - autocatalytic) mechanism for the crystal growth. With the critical number of nucleation sites formed, the large and small cages can form around them at rates k_1 and k_2 , respectively. The rate law for formation of small cages [*S*] is first order with respect to xenon, [*Xe*], and also first order in the number of large cages present, [*L*] (second order overall). Analogously, the rate law for formation of the large cages is also second order, proceeding at a rate $k_2[Xe][S]$. Thus, overall rates of formation of large and small cages are therefore interdependent.
3. The *L:S* ratio initially increases with time before reaching a final ratio of 3.75. This observation could be accounted for if the nucleation sites are assumed to be single small cage sites, a picture consistent with molecular dynamics simulations of the process and previously reported kinetic formulations.¹²⁰

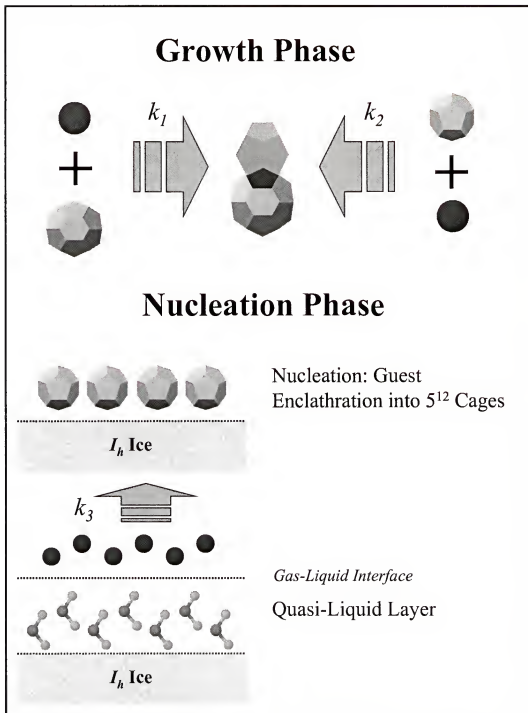


Figure 6-4. Pictorial representation of a proposed mechanism for the formation of the simple type I clathrate hydrate, involving the interdependency of the formations of the small and large cavities. Based on the mechanism proposed by Sloan and Fleyfel.¹¹⁹

4. The final pressure of xenon gas over the ice crystals under the given conditions corresponds to the dissociation pressure. The termination of the hydrate formation corresponds to the time at which the dissociation pressure is observed.
5. The nuclear spin relaxation rates of enclathrated ^{129}Xe in the large and small cages are given by $\Gamma^L = 1/T_L^L$ and $\Gamma^S = 1/T_L^S$ which need not be equal. In fact, the experimental data will show that $\Gamma^L > \Gamma^S$ which is probably due to a contribution by chemical shielding anisotropy to the relaxation rate in the large cage.

The complete proposed mechanism, which incorporates all of the above considerations with a minimum of free parameters, is presented in **Figure 6-4**. This lead to six rate equations, three in chemical concentration of the gas, small and large cages,

$$\frac{d[Xe]}{dt} = (-k_1[L] - k_2[S] - k_3)([Xe] - [Xe]_{eq}) \quad (6-18)$$

$$\frac{d[S]}{dt} = (k_1[L] + k_3)([Xe] - [Xe]_{eq}) \quad (6-19)$$

$$\frac{d[L]}{dt} = k_2[S]([Xe] - [Xe]_{eq}) \quad (6-20)$$

where $[Xe]_{eq}$ refers to the equilibrium xenon pressure, corresponding to the dissociation pressure at that temperature. These equations lead to three modified Bloch equations describing the nuclear magnetization of the three species

$$\frac{dM^{Xe}}{dt} = (-k_1[L] - k_2[S] - k_3)M_0^{Xe}([L]([Xe] - [Xe]_{eq}) - \Gamma^{Xe} M^{Xe}), \quad (6-21)$$

$$\frac{dM^S}{dt} = (k_1[L] + k_3)M_0^{Xe}([Xe] - [Xe]_{eq}) - \Gamma^S M^S, \quad (6-22)$$

$$\frac{dM^L}{dt} = k_2[S]M_0^{Xe}([Xe] - [Xe]_{eq}) - \Gamma^L M^L, \quad (6-23)$$

where $M_0^{Xe} = M_0/[Xe]_0$ is the initial molal magnetization of polarized ^{129}Xe . In the modified Bloch equations, thermal equilibrium nuclear spin polarization has been neglected, since it is undetectable in a single NMR scan. This reduces the number of unknown parameters from six to five.

A slight modification of the model is necessary to account for the fact that the sublimation of the solid xenon is not instantaneous, but rather occurs over a period of 30 to 60 s. In the ideal stopped-flow kinetics experiment, the xenon concentration would suddenly rise from zero to the value $[Xe]_0$. This is a limitation in the procedure that could be circumvented by expansion of the fully sublimed xenon gas into the ice sample. An apparatus to conduct the kinetics runs in this manner is presently being developed in our laboratory. To better approximate the data obtained by the sublimation method at short reaction times, for simplicity we will model the sublimation as a linear increase in $[Xe]$ at a rate k_{sub} over a period t_{sub} at which time no solid Xe remains. The rate of growth of ^{129}Xe gas magnetization due to sublimation at the beginning of the kinetic run is $k_{sub}M^{Xe}$. Modifying equations 6-18 and 6-21,

$$\frac{d[Xe]}{dt} = (k_{sub} - k_1[L] - k_2[S] - k_3)([Xe] - [Xe]_{eq}) \quad (6-24)$$

$$\frac{dM^{Xe}}{dt} = (k_{sub} - k_1[L] - k_2[S] - k_3)M_0^{Xe}[L]([Xe] - [Xe]_{eq}) - \Gamma^{Xe}M^{Xe} \quad (6-25)$$

where the conditions for the rate constant for sublimation, k_{sub} , are specified by

$$k_{sub} = \begin{cases} \frac{[Xe]_0}{t_{sub}} & \text{if } t \leq t_{sub} \\ 0 & \text{if } t > t_{sub} \end{cases} \quad (6-26)$$

The sublimation time t_{sub} was taken as a fitted parameter. Two additional parameters, for example k_1 and k_2 , would necessarily be fixed in order to apply a least squares fitting of the model to the experimental time dependence of the ^{129}Xe NMR signals of the large and small cages.

Model II: Two-Step Guest Enclathration

In the second proposed model, xenon gas is assumed to be in rapid exchange with the xenon adsorbed onto the ice crystal surfaces. As the concentration on the surface exceeds a critical value, $[Xe_{ads}]^{crit}$, the hydrate crystals grow. The overall kinetic scheme is identical to that which has been depicted in **Figure 6-3**, however, the only assumption taken is that the concentration of xenon adsorbed to the surfaces of the ice particles is in direct proportion to the gas pressure; that is, $[Xe_{ads}] = K[Xe]$, for some constant, K . Thus, the rate equations for the model are as follows:

$$\frac{d}{dt}[Xe] = -k_1[Xe] + k_2[Xe]_{ads} \quad (6-27)$$

$$\frac{d}{dt}[Xe]_{ads} = k_1[Xe] - k_2[Xe]_{clath} - k_3([Xe]_{ads} - [Xe]_{ads}^{eq}) \quad (6-28)$$

$$\frac{d}{dt}[Xe]_{clath} = k_3([Xe]_{ads} - [Xe]_{ads}^{eq}) \quad (6-29)$$

The assumption that $[Xe_{ads}] = K[Xe]$, for some constant K , suggests that at equilibrium, $[Xe]_{ads}^{eq} = K[Xe]^{eq}$. At equilibrium (or as reaction time approaches infinity), both conditions 6-30 and 6-31 exist.

$$\frac{d[Xe]}{dt} = 0 \quad (6-30)$$

$$\frac{d[Xe]_{ads}}{dt} = 0 \quad (6-31)$$

Therefore, one parameter can be eliminated by allowing

$$[Xe]_{ads}^{eq} = \frac{k_1}{k_2}[Xe]^{eq} \quad (6-32)$$

The modified the modified Bloch equations are then determined as

$$\frac{d}{dt}M^{[Xe]} = -k_1M^{[Xe]} + k_2M^{[Xe]_{ads}}, \quad (6-33)$$

$$\frac{d}{dt}M^{[Xe]_{\text{ads}}} = k_1 M^{[Xe]} - k_2 M^{[Xe]_{\text{clath}}} - k_3 ([Xe]_{\text{ads}} - [Xe]_{\text{ads}}^{\text{eq}}) \frac{M^{[Xe]_{\text{ads}}}}{[Xe]_{\text{ads}}} - \frac{M^{[Xe]_{\text{ads}}}}{T_1^{\text{ads}}}, \quad (6-34)$$

$$\frac{d}{dt}M^{[Xe]_{\text{clath}}} = k_3 ([Xe]_{\text{ads}} - [Xe]_{\text{ads}}^{\text{eq}}) \frac{M^{[Xe]_{\text{ads}}}}{[Xe]_{\text{ads}}} - \frac{M^{[Xe]_{\text{clath}}}}{T_1^{\text{clath}}}, \quad (6-35)$$

Once again, a slight modification of the model is necessary to account for the sublimation of the solid xenon over a period of 30-60 s. The sublimation was modeled as a linear increase in $[Xe]$ at a rate k_{sub} over a period t_{sub} at which time no solid xenon remains. The rate of growth of ^{129}Xe gas magnetization due to sublimation at the beginning of the kinetic run is $k_{\text{sub}} M^{Xe}$. Modification of equations 6-27 and 6-33 provides

$$\frac{d}{dt}[Xe] = -k_1 [Xe] + k_2 [Xe]_{\text{ads}} + k_{\text{sub}}, \quad (6-36)$$

$$\frac{d}{dt}M^{[Xe]} = -k_1 M^{[Xe]} + k_2 M^{[Xe]_{\text{ads}}} + k_{\text{sub}} \frac{M_0}{[Xe]_0}, \quad (6-37)$$

where the conditions for the rate constant for sublimation, k_{sub} , are the same as was specified in equation 6-26.

CHAPTER 7

MONITORING XENON CLATHRATE HYDRATE FORMATION THROUGH GAS UPTAKE MEASUREMENTS AND SEOP ENHANCEMENT OF ^{129}Xe NMR SIGNAL

Introduction

The guest-host and hydrogen bonding interactions, and the kinetics and mechanisms of formation of gas clathrate hydrates are of particular interest to researchers. Conventional (thermally polarized) ^{129}Xe NMR studies of *simple* type I xenon clathrate hydrate^{16,24} have complemented X-ray diffraction studies by providing information about the symmetry of the cages, cage occupancies, equilibrium dynamics of the host lattice, and energetics of the guest-host interactions. The ^{129}Xe NMR spectra show two well-resolved signals due to xenon trapped in the small *dodecahedral* (5^{12} , *S*) and the larger *tetrakaidecahedral* ($5^{12}6^2$, *L*) cavities. There are six large and two small cavities per unit cell, so that the ideal composition is $5.75 \text{ D}_2\text{O} \cdot \text{Xe}$ for the fully occupied case. The isotropic ^{129}Xe NMR chemical shifts for xenon enclathrated into the large and small cavities are located 152 ppm and 242 ppm, respectively.^{16,24,42}

Although the equilibrium thermodynamic and structural properties of the gas hydrates have been thoroughly studied for over 60 years,⁴² a complete understanding and modeling of the formation kinetics and molecular level mechanism has yet to be

achieved. The crystallization of gas clathrate hydrates is thought to occur in two mechanistic regimes, which has been most evidently demonstrated in time-resolved measurements of the pressure,¹⁰⁰ turbidity (for bulk water conditions),^{108,109} and NMR.^{16,24,25,42,121,122} Crystallization processes usually require that a number of nucleation sites form prior to more rapid rates of crystal growth. It has been suggested^{25,42,119,121} that in the case of clathrate hydrates, a critical number of individual occupied *dodecahedral* cavities must form prior to this period of more rapid enclathration. The nucleation process proceeds leisurely in comparison to the more rapid clathrate hydrate crystal growth, and thus creates a stage of gas hydrate formation referred to as the induction period.^{42,100} In the crystal growth regime that follows nucleation, the size of the crystallites increases monotonically and rapidly with time. The rate at which the seeding of crystallites proceeds depends on the ability of the guest species at stabilizing dodecahedral cages against the strong hydrogen bonding forces bridging the cavity. The xenon diameter:cavity diameter ratio⁴² approaches unity, so that the xenon atom provides adequate stabilization of the dodecahedral cavities; in turn, this permits more rapid nucleation in comparison to, for example, argon, whose atomic diameter:cavity diameter ratio deviates more significantly from unity.^{42,100} Although pressure-time dependence measurements¹⁰⁰ are capable of following the progress of clathrate hydrate formation, they lack the ability to monitor the enclathration of the guest species into each of the cavity types. This is particularly important for the confirmation that the mechanism of nucleation involves the formation of occupied dodecahedral cages. Although ¹²⁹Xe NMR of the xenon deuteriohydrate, even with a static spectrum, has the capability to resolve

resonances for xenon-occupied small and large cavities, the monitoring of clathrate hydrate crystallization on the surfaces of ice crystals is not accessible by conventional ^{129}Xe NMR is not possible due to the low sensitivity and long spin-lattice relaxation times.¹¹⁷

Providing up to a five orders of magnitude increase in the NMR sensitivity, spin exchange optical pumping (SEOP) enhancement of the ^{129}Xe NMR signal is an ideal means by which to study the kinetics of formation of xenon clathrates.^{25,121,122} The physics of optical pumping was presented more fully in Chapter 3. For the experiments presented here, a ^{129}Xe NMR enhancement on the order of 2,000-4,000 was typically attained. The utility of SEOP NMR to kinetics stems from the sensitivity enhancement that circumvents the need for signal averaging to acquire spectra with desirable signal:noise. The combination of high sensitivity, time resolution and high chemical shift dispersion makes SEOP ^{129}Xe NMR a particularly attractive technique for the study of xenon hydrate clathrate formation. The ability to use SEOP ^{129}Xe NMR to monitor the formation of type I xenon clathrate hydrate, and type II clathrate hydrates as well, in real time has been previously demonstrated,^{25,121,122} but not fully explored. This study has undertaken the task of elucidating further the hydrate formation mechanism through the combination of pressure-time dependence measurements and time-resolved SEOP enhanced ^{129}Xe NMR. These experiments endeavor to improve the results of previously reported experiments and to confirm or refute unambiguously speculations as to the nature of the nucleation process of clathrate hydrate formation.

Experimental

Preparation of D₂O Ice

In all of the experiments presented here, powdered D₂O was prepared and transferred to a 10 mm O.D. medium-wall NMR tube using the procedure that follows. First, small D₂O ice pellets were produced by dripping approximately 2 mL D₂O with a syringe into a porcelain mortar filled with liquid nitrogen. The pellets were then pulverized into a fine powder with a pre-cooled pestle while keeping the mortar filled with liquid nitrogen. The pulverized D₂O-N₂ mixture was quickly transferred into the NMR tube that was also immersed in liquid nitrogen. The liquid nitrogen was allowed to slowly boil out of the tube, and then the tube evacuated for at least one hour while immersed in liquid nitrogen until a stable pressure below 10^{-5} torr was achieved. The sample was further evacuated at a temperature matching the value at which hydrate formation was to be monitored by *in situ* NMR.

Time-Resolved Pressure Measurements for Clathrate Hydrate Formation

The quantity of powdered ice was determined so that xenon would be the limiting reagent for most of these experiments. The validity of this supposition is confirmed through the time dependence of the xenon gas uptake by the pulverized ice crystals, which were prepared in the same manner as for the NMR experiments. **Figure 7-2** shows the results of gas uptake experiments on a 1.8-g sample of pulverized D₂O ice in a 10 mm NMR tube. The freshly prepared ice was maintained at 223 K with a dry ice/isopropyl

alcohol bath while being evacuated to a pressure below 5.0×10^{-6} torr for 15 minutes. The solid symbols of **Figure 7-2** show the time dependence of the pressure after the sample was suddenly exposed to 600 μmol xenon gas at an initial pressure of 690 torr, measured at 298 K. Following equilibration to a final pressure of 170 torr, which corresponds to the expected dissociation pressure at 223 K, xenon was removed from the sample tube by evacuation to better than 5.0×10^{-6} torr, maintained for a period 30 minutes. The same ice sample was subjected to a second exposure of an identical quantity of xenon gas, at initial pressure of 690 torr (298 K). The time dependence of the pressure is shown by the open symbols. Despite previous reports^{25,100} that formation of the xenon type I hydrate clathrate exhibits no signs of an induction period, the existence of an initial period of limited, protracted growth of the xenon deuteriohydrate is evident from the comparison of the two gas uptake curves. In addition, the rate of uptake following the induction period is higher for the freshly prepared ice. In all experimental runs the final pressure above the hydrate, corrected for the temperature difference between the volume at the sample and the volume at room temperature, closely agree with the literature value for the dissociation pressure of $P_0 = 176.11$ for the xenon hydrate at 233 K.

Spin Exchange Optical Pumping of ^{129}Xe

The rubidium-xenon spin exchange optical pumping system used for this set of experiments consists of a cylindrical borosilicate glass pumping cell with a total volume of 77.6 ± 0.2 mL. The pumping cell was coated with Surfasil (Pierce Scientific), a silicizing agent that is known to increase the ^{129}Xe nuclear spin-lattice relaxation time

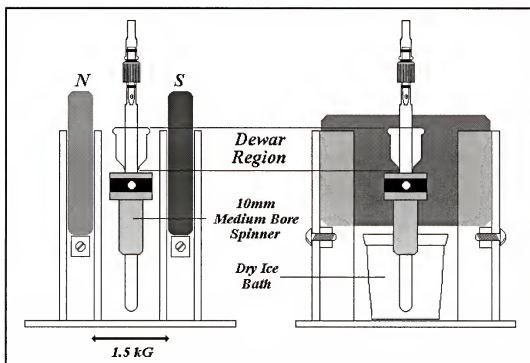


Figure 7-1. 10 mm O.D. medium wall NMR tube modified for the type I clathrate hydrate formation. The tube has been modified with a 28 mm O.D. dewar in the upper region of the tube. Xenon may be condensed in its solid form above the sample, which itself can be maintained at the desired sample and NMR probe temperature until insertion into the spectrometer.

several hundredfold. In a typical experiment, approximately 200 torr of natural isotopic abundance xenon gas (Isotec, 99.995 % purity) was loaded into the pumping cell at 298 K. The pumping cell temperature was raised to, and maintained at, 373 K in a field of about 0.01 T. Although pumping times varying from 30 to 60 minutes were used depending on experimental conditions, a typical optical pumping period of 30 minutes was employed. Following the spin exchange optical pumping stage, the pumping cell was cooled below 60 °C to re-condense the rubidium metal vapor before the extraction of the xenon gas.

Providing SEOP Enhanced ^{129}Xe to a Finely Powdered Ice Sample

Following the SEOP procedure, the polarization-enhanced xenon was condensed in solid form into the upper dewared region of a specially modified 10 mm medium wall NMR tube, shown in **Figure 7-1**. This permitted the xenon to be condensed in its solid form into the upper portion of the tube while the ice crystals at the bottom were maintained at the temperature of interest by a dry ice slush bath. A stopcock at the entrance to the tube allowed for transport from the optical pumping apparatus to the spectrometer. To avoid substantial loss of polarization during transport to the spectrometer, the solid xenon was stored in a magnetic field of 0.15 T produced by barium iron oxide permanent magnets, also shown in **Figure 7-1**. The permanent magnet assembly was transported to a Varian Unity 500 MHz (^1H frequency) NMR spectrometer equipped with a 10 mm direct observe high resolution probe. Additional experiments were conducted using a 10mm high-resolution probe installed in a Bruker Avance 400 MHz spectrometer. In either case, the sample tube was quickly removed from the permanent magnet system and inserted into the pre-cooled, pre-tuned probe. The sublimation of the xenon was followed by the sudden appearance of a gaseous ^{129}Xe signal. The sublimation was complete after a period of about 30 s. Spectra were recorded every 5-15 s during the first 4800 s of the experiment.

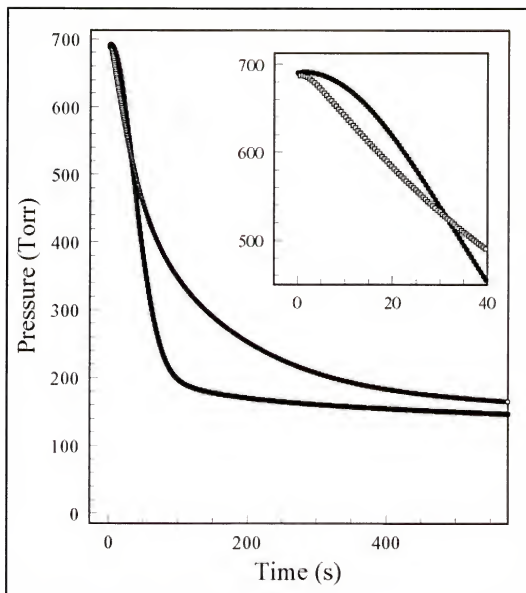


Figure 7-2. Monitoring the enclathration of xenon gas as a function of pressure. Initially, 1.8 g of freshly crushed D₂O (filled symbols) are maintained at 223 K and exposed to 600 μ mol of xenon gas, with a starting pressure of 690 torr (measured at 298 K); thorough evacuation of the sample and a subsequent exposure to an equivalent amount of xenon gas is also shown (open symbols).

Results and Discussion

Gas Uptake Data, Pressure-Time Dependence Measurements

A close examination of the first 40 s of the pressure data of **Figure 7-2** indicates that a clearly defined induction period can indeed be observed for the type I xenon clathrate hydrate. The upper portion of the S-shaped curve for the freshly powdered and exposed ice (filled symbols) is indicative of an induction period, and the distinctly different curves observed for freshly pulverized and reused ice (open symbols) verifies that the proposed induction regime is not the result of pressure transducer hysteresis. The gas uptake experiments clearly reveal that the rate of enclathration differs drastically when the ice is reused after the first exposure to xenon. This suggests that, even when the sample is evacuated under high vacuum for extended periods of time, the structural changes associated with hydrate formation are not completely reversible. A number of nucleation sites must remain on the surfaces of the ice particles, thereby reducing the time necessary to achieve the critical number of these sites.^{29,129} This “memory effect” of clathrate hydrates for successive exposures to hydrate forming molecules is not altogether unknown, but demonstration of this effect has previously been confined to clathrate formations which exhibit more prominent induction periods.^{42,110,111} It has been hypothesized that the residual nucleation sites on the surfaces of the ice particles are actually occupied *small* cages, based on their relative stability compared to the large cages.

The reversibility of the reaction equilibrium was demonstrated by observing the change in the equilibrium pressure following a temperature change of the sample. The gas pressure above the ice reversibly followed the dissociation pressure over a wide range of temperatures. Furthermore, the xenon pressure was found to return to the dissociation pressure for that temperature even after briefly opening the sample tube valve to vacuum. These observations clearly indicate that the amount of ice accessible to the xenon was in stoichiometric excess in comparison to the 600 micromoles of xenon. Full occupancy of the ice by this quantity of gas would require 3 millimoles of D_2O , yet 100 millimoles of ice are present.

Finally, the gas uptake data indicates that under the experimental conditions of temperature and pressure employed, enclathration of xenon into the clathrate hydrate structure achieves completion within approximately 10 minutes. Thus, the xenon deuteriohydrate is fully formed within a fraction of the T_I observed for xenon enclathrated inside the cavities of the type I deuteriohydrate.^{29,129}

Temperature Dependence of ^{129}Xe NMR Line Shape

Figure 7-3 presents ^{129}Xe NMR spectra of the type I xenon clathrate hydrate at a series of temperatures between 203 K to above 300 K. To obtain this series of spectra at different temperatures, the xenon hydrate clathrate was initially formed at 233 K and spectra were subsequently recorded at each of the temperatures indicated. Two exposures of the ice to SEOP enhanced ^{129}Xe were necessary to cover the temperature range while maintaining acceptable signal intensities. A period of at least 420 s was allowed at each

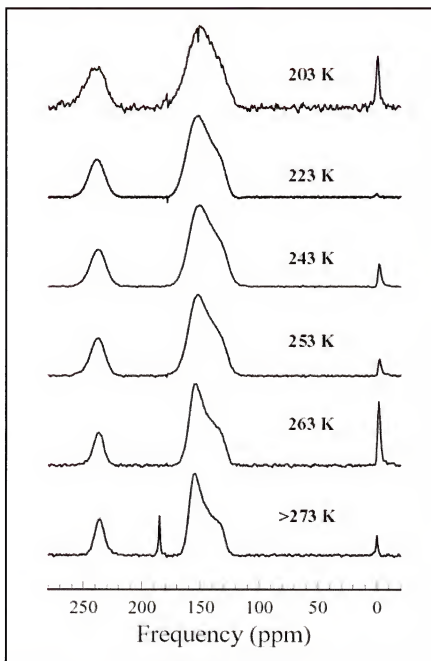


Figure 7-3. SEOP enhanced ^{129}Xe NMR spectra of the xenon type I hydrate clathrate at selected temperatures between 203 and 300 K. Initially, 1.8 g of crushed D_2O are exposed to 600 μmol of SEOP enhanced ^{129}Xe gas at 223 K; time is allowed (8 minutes) for complete formation of the clathrate hydrate and temperature equilibration. Spectra were acquired at each additional temperature after a minimum of 420 s of temperature equilibration, and with a 6 μs pulse (tip angle, 20°). A sharp signal observed at ~ 185 ppm for temperatures above 273 K indicates the dissolution of SEOP enhanced ^{129}Xe into liquid water.

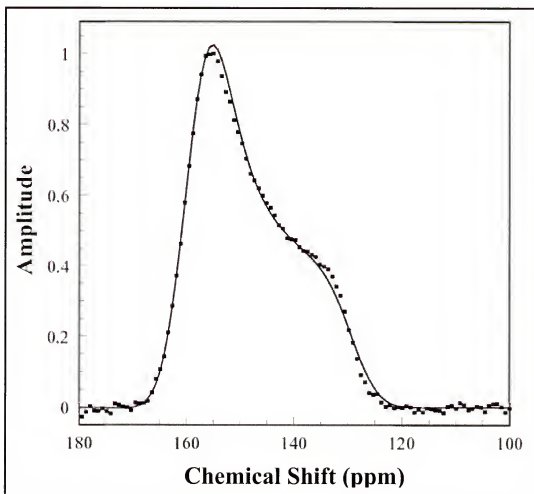


Figure 7-4. Theoretical fit of the CSA for the SEOP enhanced ^{129}Xe NMR spectrum of the xenon type I hydrate clathrate at 253 K. 1.8 g of crushed D_2O are exposed to 600 μmol of SEOP enhanced ^{129}Xe gas at 223 K. Spectra were acquired after a minimum of 420 s of temperature equilibration, and with a 6 μs pulse (tip angle, 20°).

temperature for sample equilibration prior to acquisition of the free induction decay with a single 6 μs pulse, which corresponds to a tip angle of 20° . The variation of the isotropic shifts over this range of temperatures, as referenced to the free gas peak, was found to be negligible. However, substantial changes in the broadening and line shape of both the small and large cage line shapes are clearly apparent.

Attempts to fit the line shape of xenon enclathrated into the large cavity to a cylindrically symmetric chemical shift powder pattern did not yield a good match at temperatures below 253 K, where line broadening obscures the chemical shift anisotropy (CSA). Good correspondence of the theoretical fit to the observed CSA was obtained at temperatures of 253 K or greater, as shown in **Figure 7-4**. At these higher temperatures, the ^{129}Xe NMR line shape from the large cavity enclathrated xenon is well described by a cylindrically symmetric chemical shielding powder pattern. A least squares fit of the theoretical line shape is superimposed on the experimental line from the spectrum acquired. The cylindrically symmetric chemical shielding tensor was determined, with $\delta_{\text{iso}} = 147.6$ ppm and $\Delta\delta = -29.1 \pm 2$ ppm, with respect to the gaseous ^{129}Xe NMR signal, and with a fitted Gaussian line broadening of 1416 Hz.

As mentioned previously, the ^{129}Xe NMR line shape of the signal acquired at a lower temperature cannot be adequately fitted to a single chemical shift powder pattern. Ripmeester and co-workers^{12,24} have suggested that the most likely cause of this additional broadening is the dipolar coupling with the deuterium nuclei comprising the cage. The six-fold disorder in the orientations of the water molecules is frozen in at temperatures less than about 253 K and the spectrum results from the statistical superposition of spectra resulting from all possible configurations. Over the temperature range from 203 to 273 K, the line width of the small cage doubles from 1.0 to 2.1 kHz and is satisfactorily described as Gaussian. Generally, the dodecahedral cage provides a void space of cubic symmetry; therefore, a line shape with the fairly Gaussian appearance is indeed expected in the ^{129}Xe NMR spectrum for xenon enclathrated in these smaller

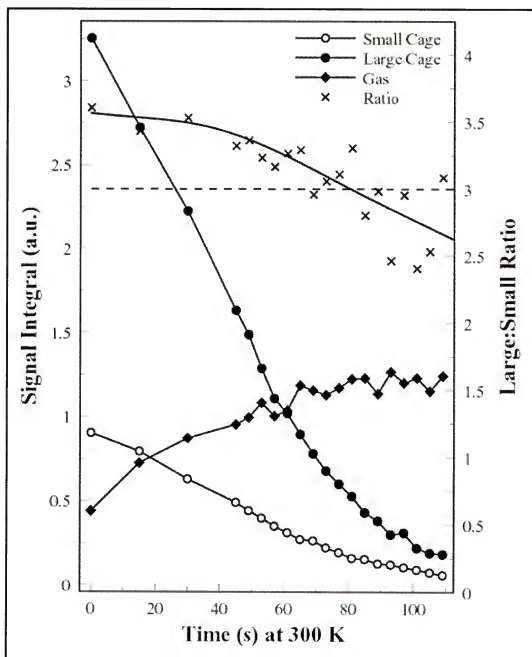


Figure 7-5. SEOP enhanced ^{129}Xe NMR spectrum of the xenon type I hydrate clathrate taken to 300 K, after formation at 223 K. 1.8 g of crushed D_2O are exposed to 600 μmol of SEOP enhanced ^{129}Xe gas at 223 K. Spectra were acquired every 15 seconds for the first 45 seconds, then every 3.3 s thereafter, with a 6 μs pulse (tip angle, 20°).

cavities.^{12,16,24,42} It appears that rapid molecular reorientation of the water molecules leads to at least partial averaging of the dipolar coupling. This observation establishes an upper limit on the correlation time of the water motion of 500 μ s at a temperature of 250 K. More detailed NMR line shape simulations would be required to quantitatively determine the value of this correlation time and the activation energy for the motion.

The spectrum acquired at the highest temperature of 300 K in **Figure 7-3** shows a peak in addition to the those of the free gas and the small and large cavities 185 ppm. This ^{129}Xe NMR resonance corresponds to ^{129}Xe dissolved in liquid D_2O at that temperature. To observe how the small and large cage, and the dissolved xenon, ^{129}Xe resonances change with time as the sample warms to 300 K, a time-resolved SEOP ^{129}Xe NMR melting experiment was conducted. The maximum gaseous xenon pressure, assuming complete reversibility of the enclathration, in the tube was well below the dissociation pressure of the hydrate at this temperature, thereby ensuring that complete melting would be inevitable. The line shapes and isotropic ^{129}Xe NMR frequencies of the large and small enclathrated xenon signals remained essentially unchanged as the spectra were recorded as a function of time over 1200 s at 300 K. As shown in **Figure 7-5**, the signal intensity of the large and small cages decayed, the gas peak intensity increased, and the L:S signal integral ratio decreased from 3.5 to a value slightly less than 3.0. No coalescence of the large and small signals, or of the dissolved signal, was observed in the process of melting. Higher xenon pressures could be employed in future studies to stabilize the clathrate at these elevated temperatures.

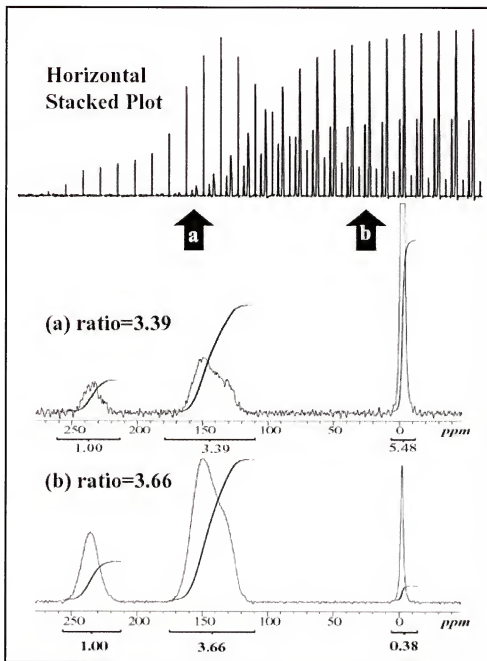


Figure 7-6. Hyperpolarized ^{129}Xe NMR spectra acquired as a function of time following insertion of the NMR tube containing pulverized D_2O ice and spin-polarized ^{129}Xe into the NMR probe at 223 K. (Top) Summary plots of the ^{129}Xe NMR integrals for the 5^{12} and $5^{12}6^2$ peaks of the type I clathrate hydrate and the gas peak. Individual spectra selected from part (a) acquired at the reaction times indicated by the arrows labeled “a” and “b”. The integrals of the $5^{12}6^2$ and 5^{12} peaks show that the occupancy ratio increases from a minimum of 3.1 at the earliest reaction time that yielded adequate signal to a steady-state value of 3.9.

Time-Resolved SEOP Enhanced ^{129}Xe NMR Spectra

Horizontally stacked plots of the SEOP ^{129}Xe NMR spectra obtained at 15-s intervals following insertion of the NMR tube containing solid SEOP enhanced ^{129}Xe and pulverized ice crystals into a probe maintained at 233 K is shown in **Figure 7-6**. The spectra presented in **Figures 7-6a** and **7-6b** were recorded at point “a” and “b” during the kinetics run. The conditions in the early stages of enclathration are dependent on the rate of sublimation of the solid xenon. A rapid increase of the free gas resonance intensity is observed initially, but then the signal monotonically decreases in intensity with time due to the uptake of the xenon by the ice. Simultaneously, ^{129}Xe signals of the large and small cages grow in. The high quality of these spectra permit accurate integration of the peak areas as well as the $L:S$ signal ratio. At neither early stages in the xenon enclathration (**Figure 7-6a**) nor at later stages in the clathrate hydrate growth (**Figure 7-6b**) does the ratio $L:S$ fall below the ideal value of 3:1. If dodecahedral cages become occupied initially as part of the nucleation process, then at some point a value below that expected from ideal composition should be observed. However, nucleation is a microscopic process, involving what might be considered a relatively small number of sites, and thus may, even with the enhancement of ^{129}Xe NMR signal, fall below the sensitivity of the technique.

A complete summary of this data is shown in **Figure 7-7a** and the experimental $L:S$ ratios are provided in **Figure 7-7b**. The collection of spectra was acquired using a single batch of spin-polarized ^{129}Xe , and with a tip angle of 6° , which corresponds to a loss of $\sim 0.5\%$ of the total magnetization following the application of each pulse. The total

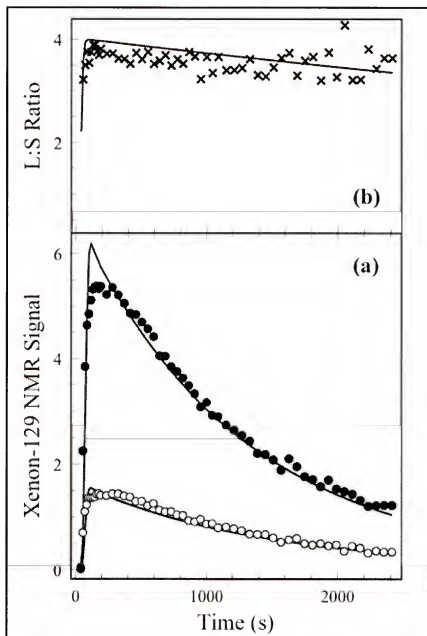


Figure 7-7. Summary plot for time-resolved ^{129}Xe NMR detection of the exposure of pulverized D_2O ice to SEOP ^{129}Xe NMR at a probe temperature of 233 K: (a) summary plot of the integrations of the 5^{12} , $5^{12}6^2$, and free gas signals as a function of reaction time; (b) a plot of the ratio of the integrations of the ^{129}Xe NMR integrals for occupied $5^{12}6^2$ cavities to those of the 5^{12} cavities as a function of reaction time.

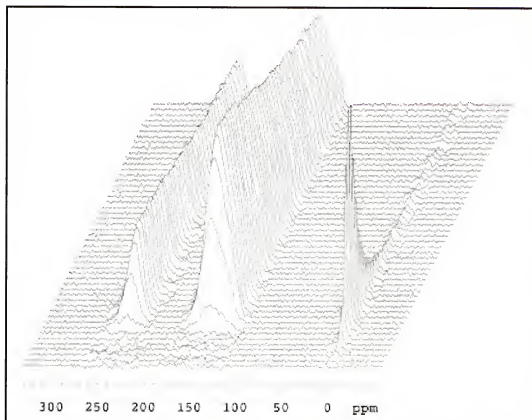


Figure 7-8. Vertically stacked plot for time-resolved ^{129}Xe NMR detection of the exposure of pulverized D_2O ice to SEOP enhanced ^{129}Xe NMR at a probe temperature of 223 K.

time of the experiment is approximately 40 minutes. Although loss of ^{129}Xe nuclear spin polarization through relaxation processes cannot be neglected over the entire of the experiment, the empirically determined T_1 for ^{129}Xe enclathrated in the cavities of the type I deuteriohydrate is on the timescale of tens of minutes.^{24,42} There are just over 5 minutes of acquisition time between the start of the experiment and position “b” in **Figure 7-6**. A further demonstration of the capabilities of the single-batch experiment is shown in **Figure-7-8**, which provides a vertical stacking of the spectra for the formation of the xenon deuteriohydrate taken at 223 K. The sinusoidal shape of the growth curves

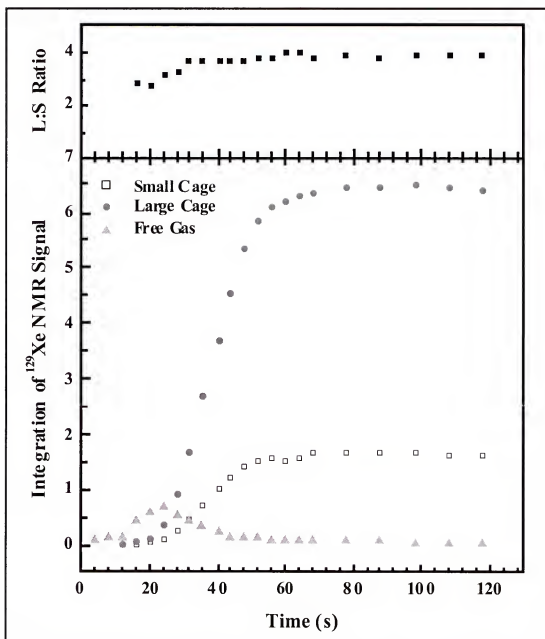


Figure 7-9. Summary plot for time-resolved ^{129}Xe NMR detection of the exposure of pulverized D_2O ice to hyperpolarized ^{129}Xe NMR at a probe temperature of 223 K: (top) a plot of the ratio of the integrations of the ^{129}Xe NMR integrals for occupied $5^{12}6^2$ cavities to those of the 5^{12} cavities as a function of reaction time; (bottom) summary plot of the integrations of the 5^{12} , $5^{12}6^2$, and free gas signals as a function of reaction time. The ratios of the integrals of the $5^{12}6^2$ and 5^{12} peaks show that the occupancy ratio increases from a minimum of ~ 3.1 at the earliest reaction time (demonstrating reliable signal intensity measurements) to a steady-state value of ~ 3.9 .

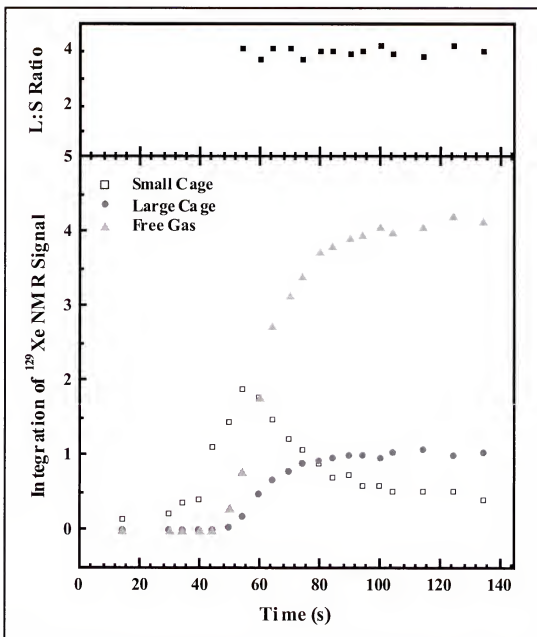


Figure 7-10. Summary plot for time-resolved ^{129}Xe NMR detection of the exposure of pulverized D_2O ice to hyperpolarized ^{129}Xe NMR at a probe temperature of 233 K: (top) a plot of the ratio of the integrations of the ^{129}Xe NMR integrals for occupied $5^{12}6^2$ cavities to those of the 5^{12} cavities as a function of reaction time; (bottom) summary plot of the integrations of the 5^{12} , $5^{12}6^2$, and free gas signals as a function of reaction time. The ratios of the integrals of the $5^{12}6^2$ and 5^{12} peaks show that the occupancy ratio increases from a minimum of ~ 3.1 at the earliest reaction time (demonstrating reliable signal intensity measurements) to a steady-state value of ~ 3.9 .

for the occupation of dodecahedral and tetrakaidecahedral cavities are consistent with the understanding that an induction period is present during the initial stages of xenon enclathration.¹²¹

Brief summaries of early exposure times for the formations of xenon deuteriohydrates at temperatures, 223 K and 233 K are provided as **Figures 7-9** and **7-10**, respectively. Presented in these figures are the NMR signal intensities corresponding those of the free gas and of xenon-occupied small and large cavities, and as well the *L:S* ratios as a function of reaction time. Note that at no point during the reaction, at either temperature, does the value of *L:S* fall below that of ideal composition.

Conclusions

In summary, presented here is a high field ^{129}Xe NMR study of the formation, melting, and equilibrium cage water reorientation using the alkali metal-noble gas spin exchange optical pumping method to enhance the ^{129}Xe NMR signal. The quality of these spectra, in terms of signal-to-noise and line shape, permit the equilibrium cage reorientation dynamics to be studied at temperatures from 203 K to above 273 K. Because of the long T_1 of the enclathrated xenon, the SEOP enhanced ^{129}Xe NMR could be used to monitor melting of the clathrate deuteriohydrate at about 300 K. In contrast to the previous work on the type I clathrate,²⁵ wherein no clathrate formation was observed at temperatures above 233 K, this research has revealed formation at temperatures as high as 263 K. Furthermore, the xenon signal from the tetrakaidecahedral cage of the

deuteriohydrate yields a pronounced chemical shift anisotropy that is well described by the theoretical chemical shift powder pattern at temperatures >253 K. The disorder in the orientations of the water molecules is frozen in at temperatures less than about 253 K and the spectrum results from the statistical superposition of all possible configurations. The temperature variation of the ^{129}Xe NMR line shape is interpreted in terms of averaging of ^{129}Xe - ^2H dipolar couplings due to reorientation of the water molecules. At a field of 11.74 T and at temperatures below 253 K, the non-decoupled ^{129}Xe line shape from the tetrakaidecahedral cage reflects the disorder in the orientations of the D_2O molecules comprising the cage. At higher temperatures, however, motional averaging of the cage D_2O molecules yields a line shape that is well represented by a theoretical powder pattern due to a single cylindrically symmetric chemical shielding tensor. It appears that rapid molecular reorientation of the water molecules leads to at least partial time averaging of the dipolar coupling at higher temperatures.

The observation that the ratio of large to small cage xenon signals remains unchanged during the melting of the hydrate clathrate is in contrast to the observation that the ratio sharply increases at early times of formation at 233 K. This implies that the melting process under the conditions here may not be simply viewed as the reverse of the formation mechanism. In addition, it is noted that at no point during the formations of the xenon deuteriohydrate did the $L:S$ ratio fall below the value 3:1, and therefore does not provide an indication of the formation of occupied dodecahedral cavities as part of the nucleation process. This information, however, does not contradict the proposed formation of occupied dodecahedra as seed crystals in the formation of the clathrate

hydrate. This step in the nucleation process may have escaped detection due to the sensitivity of the technique and the microscopic nature of nucleation.

There are two immediate improvements to the technique used here that would greatly enhance its capabilities. The first would be adding the ability to monitor the pressure simultaneously as the NMR spectra are acquired. That addition would reduce the number of unknowns necessary for the modeling of the kinetic schemes to the current data. The second would be altering the apparatus such that the ice surfaces would be exposed to the spin-polarized gas after the sublimation has completed. The sublimation of xenon can be a complicated process, and, when the correct pressure is reached, can involve a phase change to liquid form in the process. Directly introducing spin-polarized xenon in its gaseous form to the ice crystals circumvents the problem of modeling the rate of exposure of the ice to the guest species. In addition, with maximum pressure achieved at the start of the exposure, nucleation sites may appear more rapidly, increasing the chances of early detection of the formation of full-occupied dodecahedral cavities. An optical pumping system that addresses these concerns has been developed, at the schematics of the Stopped-Flow Apparatus are provided in Appendix I. Although the system has been tested and preliminary experiments conducted, the system has not yet been utilized to its fullest capabilities.

CHAPTER 8
SEOP ENHANCED ^{129}Xe NMR SPECTROSCOPY OF SF_6/Xe AND
ACETONE- d_6/Xe MIXED TYPE II CLATHRATE HYDRATES

Introduction

The dimensions and the symmetries of the cavities of clathrate hydrates influence the motions as well as the electronic environments of guest molecules, and consequently, NMR properties of the guest molecules such as chemical shifts and spin relaxation times can be used to characterize guest-host lattice interactions.^{12,24,44,123-126} For example, the ^{13}C MAS NMR spectra of natural gas hydrate samples obtained from marine sediment of the Gulf of Mexico revealed two resonance lines for methane gas occupying the small and large cavities in a clathrate hydrate structure.¹²³ By comparing the frequencies of the ^{13}C NMR resonances of the sediment sample to the Larmor frequencies observed for a standard sample of the type I methane clathrate hydrate, Ripmeester and Ratcliffe¹²³ confirmed that the hydrate was not of the type I variety, but of the type II. Previously, the type II structure had only been determined only by X-ray powder diffraction.^{127,128} Ripmeester and Ratcliffe¹²³ proposed that the natural gas hydrate had formed by the enclathration of propane solely into the $5^{12}6^4$ cavities, and that methane was confined primarily to the 5^{12} cavities.

In previous chapters, the NMR properties of ^{129}Xe that make this isotope attractive for gas clathrate studies have been thoroughly discussed. The ^{129}Xe chemical shift and line shape are more sensitive than for ^{13}C of methane to the cavity size and shape. The magnitude of the shift of the ^{129}Xe NMR resonance downfield from that of the free gas is inversely proportional to the mean free path in the cavity, and subsequently, the appearance of a chemical shift powder pattern for enclathrated ^{129}Xe reveals details of both the dimensions and symmetry of the occupied cavities. The usefulness of ^{129}Xe NMR for investigating the relative dimensions and symmetries of the cavities of the type I xenon deuteriohydrate has been well explored. Ripmeester and Davidson²⁴ were the first to observe well-resolved resonance lines for ^{129}Xe as the guest in the small and large cavities of the type I xenon deuteriohydrate, with a separation of over 150 ppm between the ^{129}Xe resonances of the occupied 5^{12} and $5^{12}6^2$ cavities.^{24,47,123,124} Analysis of the ^{129}Xe chemical shift powder pattern reveals that the $5^{12}6^2$ cavities have axial symmetry, whereas the symmetrical, Gaussian line shape for xenon enclathrated in the smaller 5^{12} cavities is indicative of an undistorted cubic symmetry.

Notwithstanding the advantages of ^{129}Xe as a probe of local structure in clathrate studies, there is a serious practical difficulty owing to the long spin-lattice relaxation times that are typically encountered for xenon as the guest in inclusion compounds. The ^{129}Xe T_1 in the clathrate deuteriohydrate is on the order of several tens of minutes,^{24,129} so that achieving adequate signal to noise in a thermally polarized ^{129}Xe NMR spectrum involves lengthy acquisition times. To address this problem, ^1H - ^{129}Xe Hartman-Hahn cross polarization (CP) with proton decoupling has been employed in ^{129}Xe NMR studies

of xenon hydrate.^{12,47} Yet even with signal enhancement achieved through CP techniques, the NMR acquisition times are still too long to permit time-resolved ^{129}Xe NMR on the timescales on which the type I xenon clathrate hydrate formed on ice crystals at temperatures above 173 K. A further limitation is that the CP method does not necessarily yield analytical information about cavity occupancy ratios, since the signal integrals depend on the CP dynamics and other factors such as motion, spin diffusion, the number of neighboring water protons and the magnitude of the dipolar couplings of the water protons to the guest and to other protons of the host lattice.¹³⁰

The advent of SEOP enhancement of ^{129}Xe nuclear polarization^{19,56,58,131} has extended the applicability of high field ^{129}Xe NMR spectroscopy to a wide range of solid state materials, including polymers,⁶⁴ zeolites,¹³² nanocrystals,¹³³ and proteins.¹³⁴ Pietrass *et al.*²⁵ first demonstrated that spin exchange optical pumping could be used to enhance the ^{129}Xe NMR signals of the type I deuteriohydrate, and this method was employed to monitor the formation of the xenon clathrate hydrate in real time. With SEOP enhanced ^{129}Xe NMR, a spectrum with satisfactory signal-to-noise can be acquired in a single scan due to $\sim 10^3$ - 10^4 fold signal enhancement.^{14,129} There is minimal depletion of the reservoir of ^{129}Xe polarization if small tip angles are employed, thereby permitting multiple spectra to be acquired in an *in situ* stopped-flow style kinetics experiment using a single batch of spin polarized xenon gas. The use of SEOP enhanced ^{129}Xe NMR circumvents the need for long delays to accommodate the spin lattice relaxation between successive signal acquisitions, as is necessary in conventional NMR derived from the thermal polarization of nuclear spins

Here, SEOP enhancement of ^{129}Xe NMR has been used to investigate xenon enclathration into two different type II mixed clathrate hydrate structures. The results provide information about (1) relative cavity occupancies of these nonstoichiometric compounds formed on the surface of ice, (2) the rates of formation, and (3) guest and host lattice interactions. Time-resolved ^{129}Xe NMR spectra were acquired to monitor the formations of the type II SF_6/Xe and the acetone- d_6/Xe deuteriohydrates at 223 K. Under the experimental conditions, it was found that the enclathration of xenon occurs on the timescale of minutes, rather than hours or days, as was reported for formations observed at 77 K.⁴⁴ The SEOP enhanced ^{129}Xe NMR method may also be applicable to the study of many other mixed gas clathrates of the type II other structures. This technique may also provide the ability to compare rates of enclathration of type I hydrate formers in competition studies.

Experimental

Preparation of D_2O Ice

Approximately 1.3 g D_2O (99.9+% purity, Cambridge Isotope Laboratories) was frozen in liquid N_2 and pulverized into a fine powder with a mortar and pestle at 77 K. The ice was then transferred to a 10 mm O.D. (8 mm I.D.) medium-wall NMR tube having a total volume $16.0 \pm 0.2 \text{ cm}^3$. The tube was immersed in a dry ice/isopropyl alcohol bath at 205 K and evacuated to a pressure of 10^{-5} – 10^{-6} torr.

Formation of the Type I Xenon Clathrate Hydrate

When freshly ground ice particles are exposed to guest molecules such as xenon, there is an initial induction period during which the reaction proceeds at a relatively slow rate. This induction period is indicative of a crystallite nucleation process or a surface structure rearrangement that is initially rate limiting; a definite mechanism has yet to be fully elucidated. Whatever the nature of this structural rearrangement, a residual template of the formation of the clathrate hydrate seems to persist even after removal of the guest species under high vacuum conditions.^{42,110,111,129} It has been proposed that a number of occupied dodecahedral structures remain intact, and serve as preformed nucleation sites when the ice is re-exposed to the hydrate former.⁴² In previous SEOP enhanced ^{129}Xe studies of type I clathrate hydrate,^{29,129} a reduction in the duration of the induction period was clearly evident for ice particles that were re-exposed to the xenon gas. Higher initial reaction rates and more intense NMR signals were consistently observed when repeating the SEOP enhanced ^{129}Xe NMR experiment with “recycled” ice.

In these experiments, a type I pretreatment of the ice particles provided nucleation sites suitable for subsequent formation of type II mixed clathrate hydrates. The specific treatment of the ice began with formation of the type I xenon clathrate deuteriohydrate by exposure of freshly pulverized D_2O ice to an initial pressure of 1000 torr SEOP enhanced ^{129}Xe gas (as measured at STP in the sealed 10 mm O.D. NMR tube described previously), maintained at a sample temperature of 223 K. Success of this first step was monitored by ^{129}Xe NMR. After this pretreatment reaction was complete, the sample was removed from the spectrometer and evacuated at a temperature of 205 K until the

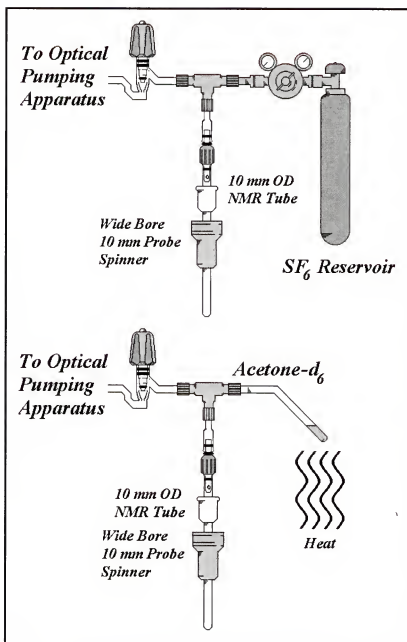


Figure 8-1. Diagrams of the vacuum manifolds used to prepare the type II clathrate hydrate samples. A 10 mm medium-wall NMR tube, with a Teflon resealable valve, contains ~1.3 g pulverized D₂O ice. The type II former is added to the 10 mm tube, and then is allowed to react with the ice for a period of 30-45 minutes at 205 K. After that time, the tube is immersed in liquid nitrogen and the spin exchange polarized ¹²⁹Xe gas is condensed onto the solid D₂O/hydrate former mixture. The tube is held at 77 K in a magnetic field of 0.15 T to preserve the xenon polarization for transport to the NMR spectrometer.

pressure stabilized below 10^{-5} torr.

Formation of the Type II SF₆/Xe Clathrate Hydrate

The apparatus shown in **Figure 8-1a** was used to condense a known quantity of SF₆ gas into the sample tube containing the pretreated ice at 77 K. The calculated final SF₆ pressure after sublimation in the sealed 10 mm O.D. NMT tube is 2.36 atm at 298 K, neglecting the reduction in pressure due to enclathration. The SF₆/D₂O ice compound was maintained at 205 K for a period of 30-45 minutes. At this temperature, the vapor pressure above solid SF₆ is about 400 torr.¹³⁵ Just prior to condensing the SEOP enhanced ¹²⁹Xe onto the SF₆/D₂O ice mixture, the sample tube was removed from the dry ice/isopropyl alcohol bath and immersed in liquid nitrogen. To preserve the ¹²⁹Xe polarization during its condensation and during the transfer of the tube to the NMR magnet, the sample was held in the magnetic field of a 0.15 T in a permanent magnet assembly. Once delivered to the spectrometer, the sample was removed from the permanent magnet assembly and inserted into the temperature-controlled NMR probe maintained at 223 K as rapidly as possible to minimize relaxation losses at zero-field.

Formation of the Acetone-d₆/Xe Type II Clathrate Hydrate

The size and geometry of acetone are such that as a guest molecule, acetone directs the formation of a type II clathrate hydrate. The 1.2 g sample of pulverized D₂O ice was subjected to the same type I pretreatment as described above. Following this pretreatment, 0.3-0.4 mL of acetone-d₆ (100% pure, Sigma-Aldrich) were introduced to

the sample tube containing the ice at a 205 K by distillation of the liquid acetone from an attached reservoir of the liquid. (See **Figure 8-1b.**) The acetone- d_6 /D₂O (ice) mixture was maintained at 205 K for a period of 30-45 minutes during which the ^{129}Xe gas was polarized by spin exchange optical pumping. It should be noted that the vapor pressure of acetone at 205 K is < 1 torr.¹³⁵ The tube was then immersed in liquid nitrogen and the SEOP enhanced ^{129}Xe was condensed in the sample tube following the same procedure as described above for the SF₆/Xe mixed clathrate hydrate.

Spin Exchange Optical Pumping of ^{129}Xe

Xenon isotope-129 in natural abundance xenon gas was polarized using the Rubidium SEOP method.^{19,64,123,132} Xenon gas at a pressure of 200-250 torr was combined with Rb metal droplets in a cylindrical borosilicate glass pumping cell with a volume of $77.6 \pm 0.2 \text{ cm}^3$. The optical pumping cell was maintained at 373-383 K in a magnetic field of approximately 100 G. Rubidium vapor was excited with 1.75 W circularly polarized light at 794.7 nm, the wavelength corresponding to the D_1 line. An argon-ion (Coherent I-200) pumped titanium sapphire (Coherent 899) ring laser provided the optical pumping beam. The xenon gas was polarized for a period of 30-45 minutes. Prior to transferring the xenon gas from the pumping cell to the sample tube, the cell temperature was reduced to allow for the condensation of Rb vapor.

Acquisition of NMR Spectra

SEOP Enhanced ^{129}Xe NMR Spectra. NMR spectra were acquired using a Bruker

Avance 400 MHz spectrometer equipped with a 10 mm high-resolution double-resonance probe. The probe was maintained at 223 K and tuned to the ^{129}Xe NMR detection frequency of 110.7 MHz. A series of free induction decays were recorded using 24° , 8 μs pulses in the case of the SF_6/Xe deuteriohydrate and 45° , 15 μs pulses in the case of the acetone- d_6/Xe deuteriohydrate.

^{19}F NMR Spectra. ^{19}F NMR spectra were acquired using a Varian Inova 500 MHz spectrometer equipped with a 10 mm high-resolution double-resonance probe. The probe was maintained at 223 K and tuned to the ^{19}F NMR detection frequency of 470.1 MHz. A series of free induction decays were recorded using 90° , 22.5 μs pulses, with a recycle time of 4 s to allow complete spin lattice relaxation of the ^{19}F spins.

Results and Discussion

^{129}Xe NMR Spectra of Mixed Type II Clathrate Deuteriohydrates

SEOP enhanced ^{129}Xe NMR spectra of mixed SF_6/Xe clathrate deuteriohydrates following a reaction time of approximately 240 s at 223 K are shown in **Figure 8-2**. These two spectra were obtained through the introduction of different initial quantities of SF_6 , 1000 torr and 3500 torr, as measured at 298 K, respectively. The spectra are presented here in their absolute intensities, and the signal intensities are not scaled according to pulse widths. In neither spectrum are ^{129}Xe NMR signals associated with occupied tetrakaidecahedral cavities of a type I xenon clathrate deuteriohydrate observed.

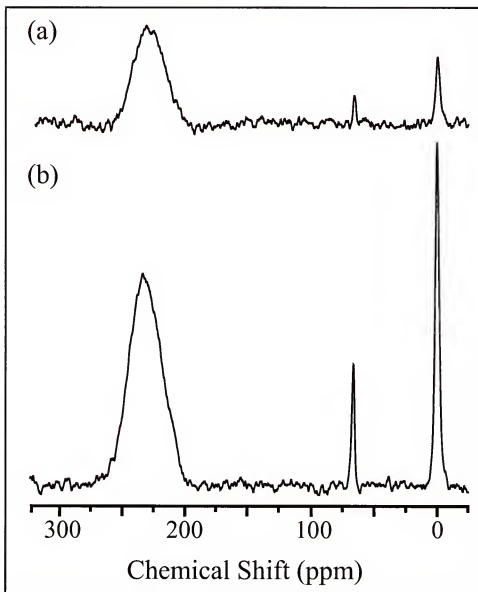


Figure 8-2. SEOP enhanced ^{129}Xe NMR spectra (110.7 MHz) of SF_6/Xe type II clathrate deuteriohydrates at 223 K. The type II structure was preformed in the absence of xenon by reacting ~ 1.1 g D_2O ice with a known quantity of SF_6 gas over a period of 30–45 minutes at 205 K. The spectra were recorded following a 240-s exposure to polarized ^{129}Xe and sample equilibration at 223 K. The conditions of the 10 mm tube sample tubes were (a) maximum pressures of 1000 torr xenon gas, 960 torr of SF_6 at 298 K and (b) maximum pressures of 1500 torr xenon gas, 2700 torr of SF_6 at 298 K. Spectrum (a) was taken with a 10 μs pulse (30° tip angle); (b) with a 30 μs pulse (90° tip angle). The chemical shift scale is referenced to the gas signal (0 ppm). A signal due to xenon occupying $5^{12}6^4$ cavities is observed at ~ 66 ppm, and for occupied 5^{12} cavities at 235 ppm.

The resonance peak shifted downfield 66.4 ± 0.1 ppm relative to the xenon gas reference corresponds to xenon enclathrated into $5^{12}6^4$ cavities, while the ^{129}Xe resonance at 235 ± 1 ppm is attributed to occupied 5^{12} cavities and exhibits a slightly asymmetric Gaussian line shape. (See **Figure 8-4b**.) The observed ratios of the 5^{12} and $5^{12}6^4$ ^{129}Xe signals is roughly 40:1 and 20:1 in **Figures 8-2a and 8-2b**, respectively. (See **Table 8-1**) These ratio values, so much larger than the ideal composition ratio of 2:1, indicate that xenon is extensively displaced from the tetrakaidecahedral cavities by SF_6 . This provides clear evidence that type II material has formed exclusively and that the xenon has been displaced from the $5^{12}6^4$ cavities. Furthermore, **Figure 8-2** suggests that the exclusion is more complete where a larger quantity of SF_6 was introduced. The spectra were acquired after differing reactions times, so a possible explanation for this disparity in ratio values could be efficient gas phase relaxation involving coupling of the ^{129}Xe and the ^{19}F nuclear spins. Assuming there was a fairly rapid exchange of nuclear spins from ^{129}Xe to the ^{19}F nuclei of SF_6 , the very short ^{19}F nuclear spin relaxation time for gaseous sulfur hexafluoride¹³⁶ would be consistent with the rapid depletion of the free gas SEOP ^{129}Xe magnetization.

To confirm that indeed the resonance at 66.4 ppm corresponds to xenon-occupied hexakaidecahedral cavities and, therefore, that a type II clathrate structure was indeed formed, the possibility that residual unpolarized xenon occupied tetrakaidecahedral cages following the pretreatment procedure must be ruled out. This may be done, on the basis of two independent observations, as follows. Firstly, the amount of residual xenon gas that remains after evacuation was found to be only a few percent of the enclathrated

xenon, as determined by measuring the pressure after melting the solid ice to water following gas uptake trials. Hence, there is a negligible amount of residual unpolarized xenon resulting from pretreatment of the ice. Secondly, the $5^{12}6^2:5^{12}$ occupancy ratio of the type I formation on freshly pulverized ice was found to be within experimental error the same as the ratio obtained for type I formation on pretreated ice. The following series of experiments were performed:

1. Freshly pulverized D_2O ice was exposed to xenon to form the type I hydrate. Once fully formed, the sample was evacuated to remove the hydrate former. The cage occupancy ratio for the 5^{12} to the $5^{12}6^2$ cavities is 3.30:1.00, respectively.
2. The resultant ice was reacted with SF_6 (or acetone- d_6) and then exposed to xenon in order to form a type II mixed clathrate. Again, the sample was re-evacuated to remove both guest components of the hydrate.
3. The evacuated sample was then re-exposed to spin polarized xenon. The result is a type I spectrum with the same cage occupancy ratio as obtained in freshly pulverized ice. (3.31:1.00)

The results confirm that xenon is removed by evacuation almost completely from both the 5^{12} and the $5^{12}6^2$ cavities, so that the ratio of the NMR peak integrations for occupied 5^{12} and $5^{12}6^4$ cavities leads to the conclusions that the type II material has formed exclusively and that xenon has been excluded from the large cavities.

The SEOP enhanced ^{129}Xe NMR spectrum of the mixed acetone- d_6 /Xe type II deuteriohydrate at 223 K is shown in **Figure 8-3**. The small, sharp resonance observed at

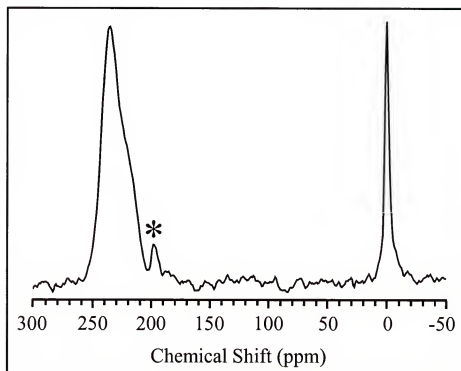


Figure 8-3. SEOP enhanced ^{129}Xe NMR spectrum (110.7 MHz) of the acetone- d_6 /Xe type II clathrate deuteriohydrate formed at 223 K. The type II structure was performed in the absence of xenon by distilling ~ 0.4 mL acetone- d_6 into the sample tube containing ~ 1.3 g ice and allowing the reaction to occur over 30–45 minutes at 205 K. The spectrum was recorded following a 240-s exposure to polarized ^{129}Xe at 223 K with a $15\ \mu\text{s}$ (45°) pulse. The calculated maximum pressure of the xenon gas following sublimation is 1250 torr. The asterisk indicates the peak due to xenon dissolved in liquid acetone- d_6 .

197 ppm corresponds to that of ^{129}Xe dissolved in liquid acetone. A resonance peak that would correspond to ^{129}Xe enclathrated into $5^{12}6^4$ cavities is not visible in this spectrum or any other acetone- d_6 /Xe hydrate spectra that were acquired during the time-resolved experiment. Lack of a ^{129}Xe NMR resonance corresponding to xenon-occupied hexakaidecahedral cavities in **Figure 8-3** suggests that exclusion of xenon from the larger cavities is more complete in the case of the acetone- d_6 /Xe deuteriohydrate. The isotropic ^{129}Xe NMR resonance of xenon enclathrated into 5^{12} cavities appears at 236 ppm, a shift

comparable to the previously reported value for xenon mixed type II clathrate hydrates.¹²⁷ Fitting of the line shape to a chemical shift powder pattern using a cylindrically symmetric shielding tensor yields a good fit with a chemical shielding anisotropy (CSA) of $\Delta\sigma = \sigma_{\parallel} - \sigma_{iso} = -19.4$ ppm, a value slightly larger in magnitude than the ^{129}Xe CSA values of -16.6 and -15.7 ppm that have been reported for the xenon occupying the $5^{12}6^4$ cavities of the mixed tetrahydrofuran (THF) and 1,1,1-dichlorofluorethane (DCFE) clathrate hydrates, respectively.^{47,127}

^{129}Xe NMR spectra for occupied dodecahedral cavities of the SF_6/Xe and acetone- d_6/Xe mixed hydrates are provided in **Figure 8-4** for comparison of their line shapes. Distortions of the 5^{12} cavities from regular icosahedral symmetry in type II clathrate hydrates have been documented in the literature,^{42,47,137} but the measured changes in the positions of the oxygen atoms of the lattice molecules have proven to be the order of tenths of angstroms.⁴⁷ Such small deformations are unlikely to account for differences observed in between the ^{129}Xe NMR spectra of the SF_6/Xe and acetone- d_6/Xe hydrate clathrates shown in **Figure 8-4**. Instead the dissimilarities of their observed line shapes can be attributed to differences in the water reorientation dynamics of these compounds.¹² The activation energy, E_a , for the reorientation of water molecules in the structure II acetone hydrate is $6.5 \text{ kcal mol}^{-1}$, whereas for the SF_6 hydrate, E_a is $12.3 \text{ kcal mol}^{-1}$.¹³⁸ At 233.2 K the dielectric relaxation times of water in the acetone and SF_6 clathrate hydrates are 0.57 s and 0.80 s, respectively,¹²⁶ indicating that the presence of SF_6 reduces the rate of relaxation of the lattice water molecules and effectively freezes out their motion.¹³⁸ Thus, at 233 K, the faster reorientation of water molecules in the structure II

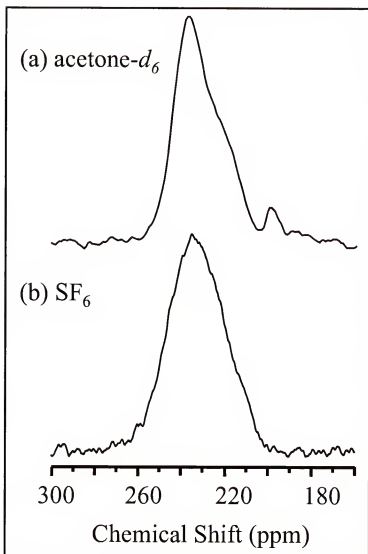


Figure 8-4. Comparison of the SEOP enhanced ^{129}Xe NMR spectra (110.7 MHz) of the 5^{12} cavity signals in the (a) acetone- d_6 /Xe and the (b) SF_6 /Xe type II clathrate deuteriohydrates recorded at 223 K. The quantity of xenon gas in each case provided calculated maximum pressures of the xenon gas of (a) 1250 torr and (b) 1500 torr (at 298 K). (a) The acetone- d_6 /Xe type II deuteriohydrate was formed by reacting ~ 0.4 mL acetone- d_6 and ~ 1.3 g ice for 30-45 minutes at 205 K, then introducing xenon gas to the sample mixture. The spectrum was recorded following a 240-s exposure to polarized ^{129}Xe at 223 K with a $15\ \mu\text{s}$ (45°) pulse. (b) The SF_6 /Xe type II clathrate deuteriohydrate was formed by reacting ~ 1.1 g D $_2\text{O}$ ice with a quantity of SF_6 gas (2700 torr maximum pressure at 298 K) over a period of 30-45 minutes at 205 K, then adding xenon gas to the sample mixture. Spectrum (b) was acquired after the sample was equilibrated to 223 K with a $30\ \mu\text{s}$ pulse (90° tip angle).

Table 8-1. Summary of ^{129}Xe NMR Chemical Shielding Parameters (2 ppm Error), Referenced to the Gaseous ^{129}Xe Signal, in the Type I Xenon Deuteriohydrate and the Type II SF_6/Xe and Acetone- d_6/Xe Deuteriohydrates. Note: $\Delta\delta = \delta_{\text{iso}} - \delta_{\text{zz}}$

Deuteriohydrate	$\delta_{\text{iso}}(5^{12})$, ppm	$\Delta\delta(5^{12})$ or FWHM, ppm	$\delta(5^{12}6^4)$ or $\delta(5^{12}6^2)$, ppm	$\Delta\delta(5^{12}6^4)$ or $\Delta\delta(5^{12}6^2)$, ppm
type-I Xe ^a	239	Gaussian, 8.7	148	-29.1
type-II SF_6 ^b	233	Gaussian, 26.4	66.5	Gaussian, 2.36
type-II Acetone ^b	231	-19.4		

^a $T = 263\text{ K}$, 138.2 MHz; ^b $T = 223\text{ K}$, 110.7 MHz

acetone- d_6/Xe hydrate results in an average environment characteristic of the true crystallographic symmetry, whereas the slow water dynamic for the SF_6/Xe hydrate would yield a reduced local symmetry. Thus, the ^{129}Xe line shape in the NMR spectrum for the SF_6/Xe deuteriohydrate represents a superposition of cage environments that are effectively static on the NMR timescale. The chemical shielding parameters for the acetone- d_6/Xe and SF_6/Xe type II deuteriohydrates are summarized in **Table 8-1**.

Time-Resolved ^{19}F NMR of the Type II SF_6 and the SF_6/Xe Deuteriohydrates

At present, no results have been published addressing a shift of the ^{19}F NMR resonance frequency for hydrate-enclathrated SF_6 from that of the free SF_6 gas. Most ^{19}F NMR experiments conducted on the SF_6 type II clathrate hydrate were performed in the 1970s,^{44,139-141} and addressed primarily measurements of the ^{19}F spin-lattice relaxation times, of the NMR line shapes, or of the ^{19}F second moments. In addition, most of these experiments were performed with sample temperatures at or below 4 K, and the results are not applicable to the clathrate hydrate at 223 K.

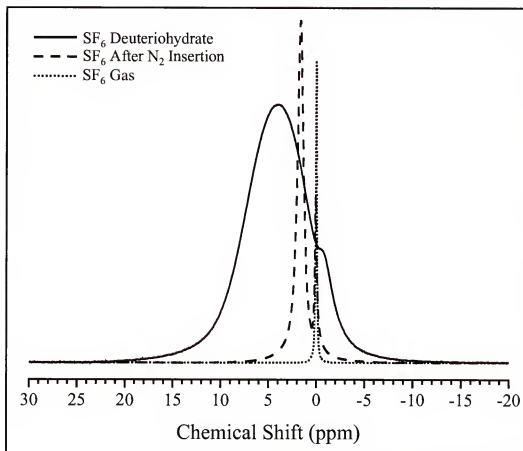


Figure 8-5. ^{19}F NMR spectra taken at a resonance frequency of 470.1 MHz. The SF_6 gas signal equilibrated at 223 K (dotted line); the combined SF_6 gas and solid signals (dashed line) obtained by insertion of the sample tube into a liquid nitrogen bath prior to probe insertion (probe temperature 223 K); and the SF_6 deuteriohydrate signal (solid line) as the sample temperature equilibrates to 223 K. Note that for the SF_6 deuteriohydrate we observe a gas signal shifted slightly upfield from that of the enclathrated SF_6 ; this gas signal which disappears as the sample equilibrates to the probe temperature. Spectra were signal averaged over 8 FIDs, which were each acquired with 90° , 22.5 μs pulses, and with a recycle delay of 4 s. The SF_6 deuteriohydrate sample was prepared by reacting ~ 1.7 g D_2O ice with a quantity of SF_6 gas (1000 torr maximum pressure at 298 K) over a period of 30-45 minutes at 205 K.

The validity of the assumption that a type II SF_6 clathrate hydrate structure was preformed prior to exposure to xenon gas under the reaction conditions has been

confirmed by recording ^{19}F NMR spectra of SF_6 , at a resonance frequency of 470.1 MHz, as a function of time for the exposure of the gas to ice surfaces that have undergone the same preconditioning with xenon gas as described in the experimental section. The ^{19}F NMR spectra of SF_6 gas, SF_6 solid and SF_6 enclathrated at the surfaces of preconditioned D_2O ice particles after chemical and thermal equilibrium at 223 K have been reached are shown in **Figure 8-5**. The chemical shift corresponding to solid SF_6 is located 1.8 ppm downfield from that of the free SF_6 gas. The broad resonance centered at 4.5 ppm is consistent with SF_6 in a type II clathrate hydrate environment that is quite distinct from the gaseous and solid-state resonance lines. These ^{19}F NMR results demonstrate that the type II SF_6 clathrate deuteriohydrate is already preformed when it is subsequently reacted with polarized ^{129}Xe to form the mixed SF_6/Xe type II deuteriohydrate as monitored by SEOP enhanced ^{129}Xe NMR.

Furthermore, the time dependence of the SF_6 ^{19}F spectra can be monitored during the reaction of xenon gas with a pre-existing SF_6 type II structure (prepared using the same procedure described earlier) by thermally polarized ^{19}F NMR, as shown in **Figure 8-6**. As the NMR tube warms to a probe temperature of 223 K, the xenon sublimates and then is enclathrated to form the mixed type II SF_6/Xe clathrate deuteriohydrate. The conditions of the experiment make it possible to observe time-resolved ^{19}F NMR signals attributed to solid and gaseous SF_6 , and to SF_6 enclathrated into the hexakaidecahedral cavities of the mixed SF_6/Xe type II structure. When both chemical and thermal equilibrium have finally been reached after approximately 12 minutes, only a broadened gaseous signal due to non-enclathrated SF_6 and a type II SF_6 clathrate hydrate signal are

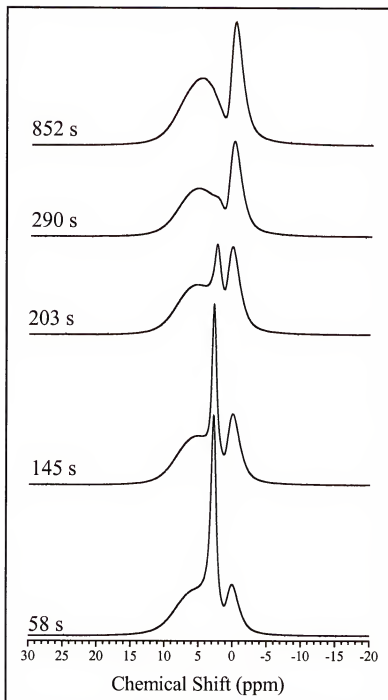


Figure 8-6. Time-resolved ^{19}F NMR spectra of SF_6 enclathrated into $5^{12}6^4$ cavities of the type II SF_6/Xe mixed clathrate deuteriohydrate recorded at a probe temperature of 223 K. Individual spectra were signal averaged over 8 FIDs, acquired with 90° , $22.5\ \mu\text{s}$ pulses, and with a recycle delay of 4 s. Acquisition times are reported as the time at which the final FID is detected. Maximum pressures of both SF_6 and xenon are ~ 1000 torr.

evident in the ^{19}F spectrum. The intensity of the ^{19}F signal corresponding to the enclathrated SF_6 remains essentially constant throughout the experiment, until near the end of the experiment, where it is believed that the sample either (1) experiences an increase in the pressure of the SF_6 free gas as the solid sublims or (2) enclathrates additional SF_6 to accommodate the inclusion of xenon into the hydrate structure. These ^{19}F NMR results demonstrate that the type II SF_6 hydrate clathrate is already preformed when it is subsequently reacted with polarized ^{129}Xe to form the mixed Xe/SF_6 type II deuteriohydrate as monitored by SEOP enhanced ^{129}Xe NMR.

Enclathration of SF_6 into a simple clathrate hydrate structure has been performed elsewhere in order to magnetically isolate these spherical top molecules.^{44,139-141} Majid *et al.*¹⁴² had demonstrated, that in the fully protonated hydrate, the main contribution to the ^{19}F second moment, M_2 , comes from interaction with the protons of the hydrate lattice. Intermolecular interaction of the fluorine spins of SF_6 molecules contributes to the second moment a value of $317.4 \sum_k R_k^{-6} G^2$, where R_k is the distance between a cage center and the center of a neighboring cage which contains fluorine nucleus k . With a distance of 7.45 Å to the first neighbor and 12.17 Å to each second neighbor, the contributions to the ^{19}F second moment are 0.044 G^2 and 0.007 G^2 , respectively. The contribution of the first and second neighbors to the total M_2 in the clathrate hydrate is approximately 4.43 percent. Thus, the interaction of the hydrogen nuclei of the hydrate lattice with ^{19}F nuclei and not direct ^{19}F - ^{19}F intermolecular coupling, contributes decisively to the total intermolecular dipolar interaction of the guest molecule.

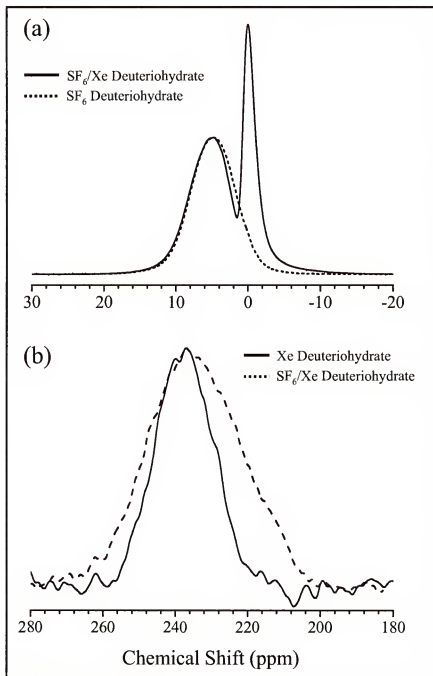


Figure 6-7. (a) Overlay of the ^{19}F NMR spectra of the (dashed) SF_6 and the (solid) SF_6/Xe type II deuteriohydrates at 223 K, signal averaged over 8 FIDs, with 22.5 μs (90°) rf pulses. Spectra have been normalized according to the enclathrated SF_6 signal intensity. (b) Overlay of the SEOP ^{129}Xe NMR spectra of the (dashed) SF_6/Xe type II and the (solid) Xe type I deuteriohydrates at 223 K, single FID, 30 μs (90°) rf pulse. Spectra have been normalized according to the xenon-occupied 5^{12} cavity signals.

There has been evidence, however, that the ^1H spins of an $(\text{H}_2\text{O})_n$ lattice can indirectly couple guest-guest spins. For example, Ripmeester *et al.*,¹⁶ cited a reduction in the ^{129}Xe NMR spin lattice relaxation time for ^{129}Xe enclathrated into the dodecahedral cavities of the adamantane/Xe type H hydrate. To prevent a possible indirect coupling of the ^{129}Xe and ^{19}F nuclear spins, ^1H nuclei of the hydrate lattice were replaced with ^2H to prepare the type II clathrate deuteriohydrate. This should, therefore, provide almost complete magnetic isolation of both guest molecules. The work of Garg *et al.*,⁴⁴ supported this proposition by demonstrating that in the THF/ CH_4 type II deuteriohydrate the contribution to the ^1H second moment is almost the same as that attributed to the $(\text{D}_2\text{O})_n$ lattice, a contribution of approximately 0.88 percent of the total value for M_2 . Davidson *et al.*¹⁴³ provided a similar result for the ^{19}F second moment for the mixed NF_3/THF type II deuteriohydrate. Direct ^{19}F second moment calculations for enclathrated SF_6 are not possible with our results since these signals are much broader than the natural line widths. **Figure 8-7a** superimposes the ^{19}F NMR line shapes of the simple SF_6 and the mixed SF_6/Xe deuteriohydrates at 223 K. Comparison of the ^{19}F line shapes indicates no observable broadening due to ^{19}F - ^{129}Xe dipolar interactions under the experimental conditions. Additionally, **Figure 8-7b** superimposes the ^{129}Xe NMR line shapes of the same type I xenon deuteriohydrate and the mixed SF_6/Xe deuteriohydrate at 223 K. Although there is a slight broadening of the ^{129}Xe NMR line shape, the resulting anisotropic broadening of the resonance suggests that any ^{19}F - ^{129}Xe dipolar interaction is not as influential as are changes in the dimensions of the dodecahedral cavities between those of the type I and the type II varieties. The analysis of **Figure 8-7** should not

decisively exclude the possibility that ^{19}F - ^{129}Xe dipolar guest interactions are present, but they are consistent with the small M_2 values calculated for similar systems.

Time Dependence of the ^{129}Xe Enclathration Into the Mixed Type II Clathrate Deuteriohydrates

When a molecule directing the structure of the type II or the type H clathrate hydrate is added to a preformed type I clathrate hydrate, a conversion to the more thermodynamically stable type II, or type H, structure occurs.^{16,42} Such conversions have been observed at gas-liquid interfaces at temperatures approaching the freezing point of water.¹⁶ However, clathrate hydrate conversions occurring in bulk liquid may take hours or days to reach completion, so that ^{129}Xe NMR spectra can be acquired by conventional CP-NMR techniques every several hours to monitor the reaction. Under the experimental conditions of the present work, the clathrate hydrate formation occurs on the time-scale of tens of seconds to minutes. Therefore, the conventional CP-NMR approach is of limited use. Furthermore, cavity occupation ratios derived from the CP enhanced signals are not necessarily reliable, as noted above. The advantage of the SEOP method is that the formation mechanisms can be studied at temperatures more comparable to natural conditions. At these higher temperatures a liquid-like surface water phase exists on the ice particle surfaces, and molecular motion, diffusion and hydrogen bonding rearrangements in this phase will be significantly more rapid.¹⁴⁴⁻¹⁴⁷

Using SEOP enhanced ^{129}Xe NMR we were able to follow in real time the formation of both the SF_6/Xe and acetone- d_6/Xe deuteriohydrates on the surfaces of

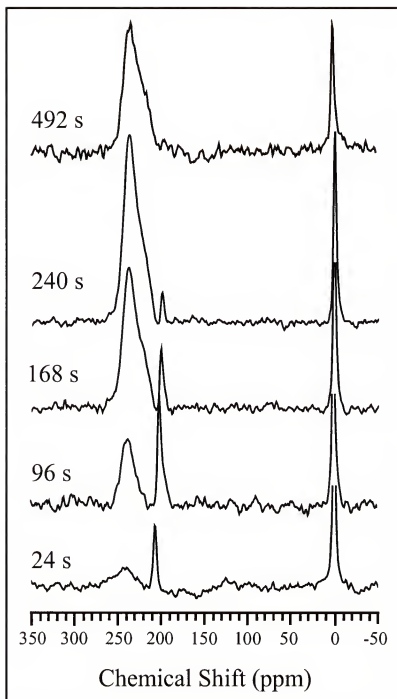


Figure 8-8. Time-resolved SEOP enhanced ^{129}Xe NMR spectra (110.7 MHz) following the formation of the acetone- d_6 /Xe clathrate hydrates, *in situ*. The reaction was run at 223 K with ~ 1.4 g ice, 0.4 mL acetone- d_6 , and a calculated maximum xenon pressure of 1250 torr. The free induction decay signals were acquired using $15\ \mu\text{s}$ pulses (45°) at 12-s intervals, with the origin of time being defined as the time of insertion of the sample into the NMR magnet.

finely powdered ice crystals. **Figure 8-8** shows individual single-scan ^{129}Xe NMR spectra of the acetone- d_6 /Xe deuteriohydrate recorded at the times indicated. Once again, the resonance at 197 ppm corresponds to that of ^{129}Xe dissolved in acetone. This signal decays as ^{129}Xe either relaxes or leaves this phase to become incorporated into 5^{12} cavities. At longer reaction times, a decay of the ^{129}Xe signals is observed, as shown in **Figures 8-9** and **8-10**. The magnetization decay of ^{129}Xe in the 5^{12} cavities is presented for both the SF_6/Xe and acetone- d_6 /Xe deuteriohydrates. The curves have been normalized at the peak of their signal amplitudes. The single scan acetone- d_6 /Xe hydrate NMR spectra were acquired every 12 s with 45° rf pulses, while the SF_6/Xe hydrate spectra were acquired with 23° rf pulses every 20 s.

Notice that even with more frequent pulsing with a greater flip angle, the ^{129}Xe signal decays more slowly in the case of the acetone- d_6 clathrate hydrate. The factors affecting the observed time dependence of the ^{129}Xe signal amplitudes include the xenon enclathration rate, the spin-lattice relaxation times in the cavities or on the ice surface, magnetization destruction due to the application of successive rf pulses, and possibly the chemical exchange between the gaseous and clathrate phases. The solid curves of **Figures 8-9** and **8-10** represent the calculated loss of magnetization due only to the successive rf pulses for the SF_6/Xe hydrate and the acetone- d_6 /Xe hydrate. The experimental time dependence of the intensity of the ^{129}Xe NMR signal, S , for the SF_6/Xe deuteriohydrate follows an $S(t_n) = S(t_{n+1}) \cos^n \theta$ curve, where θ represents the applied tip angle (23°), and t_n is the time at which the n^{th} pulse is applied. The close association of the experimental signal intensities to the curve suggests that (1) the hydrate has been fully

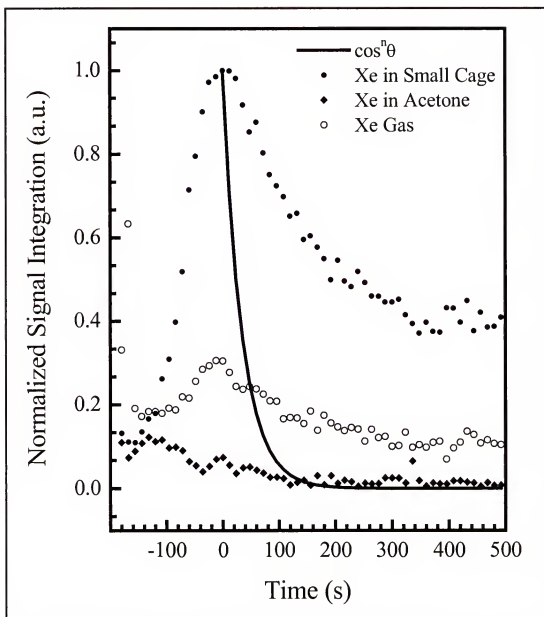


Figure 8-9. Time dependence of the SEOP enhanced ^{129}Xe NMR absorption signal integrals acquired during the *in situ* formation of the acetone- d_6 /Xe type II deuteriohydrate at 223 K. Spectra were recorded immediately following insertion into the spectrometer/probe. The data have been normalized to the area of the maximum observed 5^{12} -cavity signal, and the origin of time has been shifted to coincide with the time at which the maximum observed 5^{12} -cavity signal was obtained. In each plot, the function is plotted as a solid curve. The sample tube initially contained ~ 1.4 g ice, 0.4 mL acetone- d_6 , and a calculated maximum pressure of 1250 torr spin polarized xenon gas. Spectra were acquired every 12 s with a $15\ \mu\text{s}$ ($\theta = 45^\circ$) pulse.

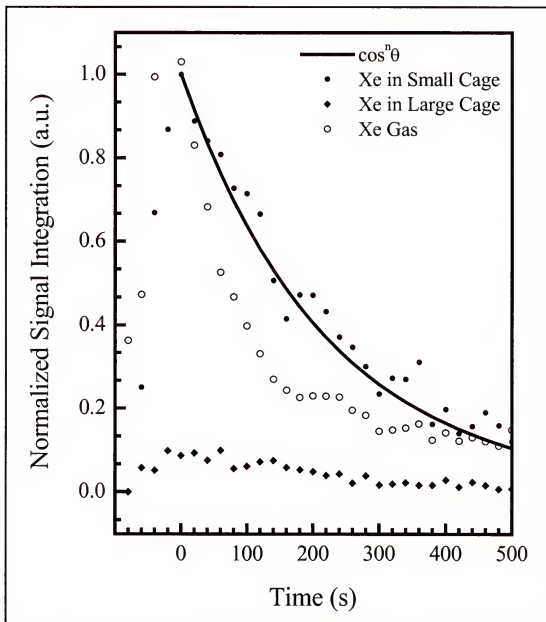


Figure 8-10. Time dependence of the SEOP enhanced ^{129}Xe NMR absorption signal integrals acquired during the *in situ* formation of the SF_6/Xe type II deuteriohydrate at 223 K. Spectra were recorded immediately following insertion into the NMR spectrometer/probe. The data have been normalized to the area of the maximum observed 5^{12}-cavity signal, and the origin of time has been shifted to coincide with the time at which the maximum observed 5^{12}-cavity signal was obtained. In each plot, the function is plotted as a solid curve. The initial calculated SF_6 pressure is 1600 torr (at 298 K) and xenon gas pressure is 1530 torr. Spectra were acquired every 20 s with an $8\ \mu\text{s}$ ($\theta = 23^\circ$) pulse.

formed within the initial 240 s of the experiment, and that (2) the decay of ^{129}Xe magnetization in the hydrate is dominated by the effects of repeated pulsing as opposed to ^{129}Xe spin lattice relaxation. In contrast, the experimental time dependence for the acetone- d_6 /Xe deuteriohydrate exhibits a substantial deviation from the curve modeling the depletion of magnetization through rf pulses. From the data available, one cannot rule out the possibility that there may be chemical exchange between xenon in the gas phase and enclathrated xenon. Since the gaseous xenon occupies the entire volume of the NMR tube and not only the region within the rf coil, the destruction of the gaseous xenon magnetization due to rf pulses would be mitigated. However, it is also possible that the formation of acetone/Xe hydrate continues to occur at times well beyond 240 s. Note that the sharp peak at 197 ppm, which is assigned to ^{129}Xe dissolved in acetone, initially increases, presumably as the xenon gas dissolves into the solvent, and then decreases at longer reaction time as both the acetone and xenon are consumed to form the type II mixed hydrate. Simultaneously, the NMR signal attributed to the xenon enclathrated into 5^{12} cages grows larger. The lower vapor pressure of acetone- d_6 compared to that SF_6 at the reaction temperature could explain the apparent slow but continued formation of new hydrate that compensates for the loss of signal due to magnetization destruction by the rf pulses.

Future work will address the use of higher polarizations so that smaller rf tip angles may be employed. Higher ^{129}Xe spin polarizations could permit direct measurement of the spin-lattice relaxation time following the enclathration of xenon into the type II structure. Previously, it was suggested that guest molecules confined to the

large cavities of the type II deuteriohydrate are magnetically isolated from one another – *i.e.* the dipole-dipole couplings to guest molecules in surrounding large cavities are effectively negligible.^{139,142,148} To support this conjecture, it has been shown for several mixed type II clathrate hydrates that intermolecular dipolar couplings of guest molecules do not significantly contribute to the second moment of the of either ^1H or ^{19}F NMR line shapes.^{16,44,142,143} SEOP enhanced ^{129}Xe relaxation studies, however, may potentially be more sensitive to guest-guest dipolar interactions, where the dipolar relaxation rate should follow a $1/r^6$ dependence. This property could be used to obtain further information about cage occupancy pattern in the type II SF_6/Xe clathrate hydrate.

Conclusions

This chapter reports the observation of formation of SF_6/Xe and acetone- d_6/Xe mixed type II clathrate deuteriohydrates on the surfaces of ice particles at the relatively high temperature of 223 K using time-resolved SEOP enhanced ^{129}Xe NMR. In the SF_6/Xe deuteriohydrate, the NMR signal amplitude for the ^{129}Xe enclathrated into the $5^{12}6^4$ cavities is about one-twentieth that of xenon trapped in the 5^{12} cavities. The lack of any signal due to xenon in $5^{12}6^4$ cavities of the acetone- d_6/Xe deuteriohydrate indicates an even higher propensity of acetone to occupy the large cages to the greater exclusion of xenon. These high quality polarized ^{129}Xe NMR data clearly demonstrate that there is a negligible amount of residual unpolarized xenon resulting from pretreatment of the ice, and that the pretreatment has no effect on the cage occupancy ratio of type I or type II.

Thus, we can eliminate the possibility that residual, unpolarized xenon plays a role in displacing polarized xenon from the large cages in either type I or type II hydrate.

Time-resolved ^{19}F NMR spectra were also acquired in order to monitor the formation of type II SF_6 deuteriohydrate under reaction conditions identical to those of the SEOP enhanced ^{129}Xe formation studies. The ^{19}F NMR data clearly supports the conclusion that the type II SF_6 hydrate is preformed prior to addition of spin polarized xenon, and that the xenon reacts directly with this preformed type II SF_6 deuteriohydrate. Additional proof that the type II has formed in the case of the SF_6/Xe mixed hydrate comes directly from the spectra in **Figure 8-2**. The peak having a chemical shift of 66.4 ppm has been previously attributed to xenon in a type II clathrate hydrate structure. However, the ratio of the NMR peak areas is very much larger than the stoichiometric ratio of 2:1. (A ratio for the $5^{12}:5^{12}6^4$ occupied cavities of almost 20:1 was obtained for the sample conditions used in acquiring the spectrum of **Figure 8-2b**, and of almost 40:1 for the spectrum of **Figure 8-2a**.) This is an additional compelling argument that type II material has formed exclusively and that the xenon has been displaced from the large cages.

The observed time dependence of the ^{129}Xe signal amplitude leads to the conclusion that the reaction to form SF_6/Xe deuteriohydrate has reached completion within about 240 s. The decay of the signal is in accordance with the dependence expected if the loss of magnetization is primarily due to the application of successive rf pulses. A qualitatively different result was obtained in the case of the acetone- d_6/Xe deuteriohydrate formation. In this reaction, the signal due to ^{129}Xe in the 5^{12} cages

decayed more slowly than that which would be expected from the destruction of magnetization by rf pulses. Two possible explanations for this behavior are offered. Due to the low vapor pressure of the liquid acetone in the sample tube, the enclathration of ^{129}Xe into the type II compound appears to continue over a longer time-scale. As the acetone evaporates, it combines with ice and xenon to form new mixed clathrate hydrate material. The incorporation of polarized ^{129}Xe gas into the solid compensates for the depletion of magnetization due to the applied rf pulses. Alternatively, chemical exchange between enclathrated xenon at the ice surface with xenon in the gas phase could explain the relatively slow decay of the 5^{12} -cavity signal.

A comparison of the ^{129}Xe NMR line shapes due to xenon enclathrated into the 5^{12} cavities of the SF_6 and acetone- d_6 type II clathrate deuteriohydrates shows significant differences that can be attributed to differences in the reorientation dynamics of each guest. Fast water dynamics in the acetone hydrate will result in an average environment characteristic of the true crystallographic symmetry, whereas the slow water dynamics in the SF_6 hydrate would give rise to a freezing in of the water disorder. The ^{129}Xe NMR line shape in the SF_6 hydrate represents a superposition of cage environments that are effectively static on the NMR timescale. It has been demonstrated, in the preceding chapter using the xenon type I clathrate deuteriohydrate, that a temperature dependence of the effects of lattice disorder on the NMR line shape of the tetrakaidecahedral guest molecule can be explored using temperature-jump SEOP enhanced ^{129}Xe NMR. Previously, this effect had only been demonstrated by conventional (thermally polarized) ^{129}Xe NMR for the type I clathrate hydrate.

The methods presented here should be applicable to a wide range of type II and type H xenon clathrate hydrate systems. The SEOP enhanced ^{129}Xe NMR technique combines the advantages of increased signal, as is necessary to monitor enclathration at the ice surface at relatively high temperatures where the reaction time-scale is on the order of seconds to minutes, with the high chemical shift dispersion of ^{129}Xe atom. The ^{129}Xe spectrum contains information about the size and shape of the cavities, and the signal integrals are directly proportional to the cage occupancy numbers. All in all, the method is extremely well suited to the study of xenon clathrate structure, kinetics and mechanism.

CHAPTER 9

EXPLORING SURFACES AND CAVITIES IN SELECTED PROTEINS BY SEOP ENHANCED ^{129}Xe NMR

Introduction

Recent improvements in the preparation of SEOP enhanced ^{129}Xe have led to innovative applications in NMR,^{2,19} including the studies of xenon bound to the solid surfaces,^{74,132} the medical imaging of xenon in lungs¹⁴⁹ and in blood,¹⁵⁰ and the imaging of microporous materials.^{151,152} Fractional ^{129}Xe nuclear spin polarizations greater than 70% have been achieved in small batch quantities of ^{129}Xe ,^{83,153} and with the advent of continuous flow optical pumping cells and high power diode laser arrays, large quantities of SEOP enhanced gases can be produced and stored for hours.¹⁵⁴ A great deal of effort is being expended to optimize the conditions for efficient intermolecular polarization transfer from the high magnetization ^{129}Xe reservoir to other nuclei of interest. Improved sensitivities for nuclei in close dipolar contact with spin polarized ^{129}Xe have been realized using thermal mixing,⁷² Hartmann-Hahn cross-polarization,⁷⁴ and intermolecular nuclear Overhauser effect in solution^{151,155} and on solids,¹³² but the potential for dramatic NMR signal enhancements of four to five orders of magnitude through polarization transfer has yet to be realized. To date, maximum polarization transfer enhancements of

up to 200 have been reported.⁷² As techniques for the production of large volumes of highly polarized ^{129}Xe are developed, and more efficient polarization transfer conditions are determined, the diversity of these applications will continue to expand.

Presented here are the results of the application of SEOP enhanced ^{129}Xe NMR to selected lyophilized protein solids. By this method, the binding interactions of xenon to the surface of several different proteins in the solution and lyophilized states were explored, and the results are compared with N_2 , Xe , and CH_4 gas adsorption isotherms. The experiments are intended to gain a better understanding of the xenon-protein interactions and to investigate the conditions under which maximal dipolar contact between the ^{129}Xe nuclei and nuclear spins situated in specific Xe binding sites on proteins can be achieved. Isoform 1 of soybean lipoxygenase (SBL-1), a protein with a large internal cavity,¹⁵⁶⁻¹⁵⁸ and three other proteins in the lyophilized solid state, metmyoglobin (metMb), methemoglobin (methHb), and hen egg white lysozyme (Hel), are compared with respect to xenon binding. With the exception of Hel, these proteins all possess a paramagnetic iron center. In principle, a large paramagnetic shift of the ^{129}Xe NMR signal should be observed if the xenon is in exchange between the gas phase and a binding site in close proximity to the iron, and fast spin-lattice relaxation of the ^{129}Xe should also be evident. Of the proteins chosen for study, information about xenon binding is available from solution NMR and/or X-ray crystallography studies for metMb,^{26,159-161} methHb,^{26,159-161} and Hel,¹⁶² but SBL-1 has not been studied previously with regard to xenon binding. In our solution state studies, the previously reported exchange of free xenon with xenon bound to metMb is revisited. In an SBL-1 solution, an analogous

exchange behavior is observed, but with a transition from the slow to intermediate exchange regime occurring at higher temperature than in metMb solutions. The solution state data is compared with the ^{129}Xe NMR and gas adsorption isotherm data of the lyophilized state of these proteins.

Studies of xenon binding in proteins originated with the X-ray crystallographic work of Schoenborn *et al.*,²⁶ who demonstrated that xenon binds near the heme of metMb in the proximal cavity. Subsequent X-ray examination revealed other binding sites in metMb and in methHb.^{159,161} Dozens of structures that include xenon bound at specific sites in cavities or pockets in proteins have been reported,¹⁶² and these heavy atom sites are used for phasing in the X-ray structure determination. Access of xenon to cavities in proteins that functionally bind gas molecules is especially interesting. Solution state ^{129}Xe NMR studies of myoglobin and hemoglobin in various spin states provided further information on kinetic parameters of xenon binding.¹⁶⁰ Xenon line widths and chemical shifts were found to be functions of xenon gas pressure, protein concentration, spin state of the protein, and temperature. Analysis of the ^{129}Xe NMR signals in terms of multiple site exchange provided association rates and binding activation energies. X-ray crystallographic studies conducted at 270 K and 7 atm of xenon provided evidence of 4 xenon-occupied sites with fractional occupancies ranging from 0.45 to 1.0.¹⁶¹ It was concluded^{160,161} that the NMR experiments could distinguish two types of Xe sites on metMb and one on methHb. In some cases, it has been shown that Xe binding is not unique; other small molecules, such as cyclopropane¹⁶³ and benzene,¹⁶⁴ also bind to internal cavities in proteins.

Lipoxygenases catalyze the first step in oxidation of unsaturated fatty acids to form oxidation products involved in a variety of inflammatory responses.¹⁶⁵ Although structures of several representatives of the SBL-1 family of enzymes exist,^{156,157,165-168} there is only limited information about how substrates (unsaturated fatty acids and oxygen) interact with the large internal cavity. The iron ion involved in catalysis is located adjacent to the cavity. Thus far, one inhibitor¹⁶⁶ and several water molecules¹⁶⁴ have been located near or within the cavities of lipoxygenases by X-ray crystallography studies. The solid state ^{129}Xe NMR spectra and the gas adsorption isotherm data presented here show that lyophilized SBL-1 has a higher affinity than metMb, methHb, and Hel (per mole of protein) for xenon and several other gases.

Description of Proteins Selected for ^{129}Xe NMR Studies

Methemoglobin. The structure of hemoglobin consists of an iron-containing pigment, called *heme*, and a simple protein, globin, and it is the heme group that is responsible for the binding of a single O_2 molecule. The binding of an O_2 molecule directs conformation changes in the protein, centered about the histidine branch proximal to the binding site. Methemoglobin is a compound form of hemoglobin that can hinder the ability to carry adequate amounts of oxygen to the body tissues. In methemoglobin, the iron heme has been converted from its ferrous state to the ferric oxidation state. The presence of methemoglobin usually results from contamination of unaltered hemoglobin with aniline dyes, potassium chlorate, or various other chemicals, particularly nitrites.

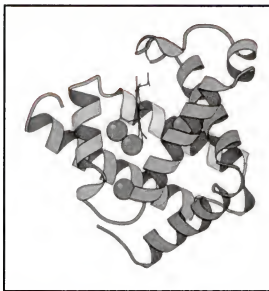


Figure 9-1. The tertiary structure of metmyoglobin is presented here, with the primary regions known to bind gases such as xenon shown as blue spheres. Reprinted with permission from B.J. Gaffney.

Metmyoglobin. Metmyoglobin, also known as ferrimyoglobin, is the compound form of myoglobin where iron is in its most oxidized state. The tertiary structure of the myoglobin molecule consists of eight alpha helices tightly packed about a prosthetic heme group.¹⁶⁹ Information from infrared and other spectroscopic techniques suggest that the xenon experiences only a weak interaction with the iron heme, unlike the stronger interactions of oxygen, carbon monoxide, and cyanide with iron.¹⁷⁰ Additional cavities are occupied at higher pressures. At a pressure of 7 bar, there is one fully occupied, and three half-occupied sites.¹⁷¹ (See **Figure 9-1.**) The cavity that hosts the xenon atom in the protein at 7 bar is located 8.1 Å away from the heme iron.¹⁷²

X-ray diffraction studies put the xenon in a most highly occupied site opposite to that of the actual O₂ absorption site in metmyoglobin.^{169,170} The distance of the xenon

absorption site from the actual heme group may lengthen the relaxation time enough to explain why the ^{129}Xe NMR resonance corresponding to this site is observable, but why it was not observed with the methemoglobin. In metmyoglobin solutions, the ^{129}Xe T_1 has been reported to be as short as 5.2 ms, but perhaps in the lyophilized protein. Spectral studies support the statement that the iron-xenon interaction is weak, and very different from that between iron and strong ligands, like CO, O₂, and CN⁻.¹⁷⁰

Soybean Lipoxygenase. The lipoxygenase enzyme catalyzes oxidation of fatty acids.¹⁷³⁻¹⁷⁵ Quantities of soybean lipoxygenase-1 can be separated from the oil vesicles in whole soybeans. The crystal structure of SBL-1 has been studied in detail elsewhere.^{157,166,176} SBL-1 has two important active sites, located in void spaces within the protein structure designated simply as cavities I and II.¹⁵⁷ The catalytic iron atom of SBL-1 is buried nearly at the center of the second domain and two of the histidine ligands associated with the iron atom is on the long helix (HIS504, HIS690). This catalytic iron center, unlike that of myoglobin, is not coupled to any heme groups. Buried deeply inside the structure of the protein, only two paths are available by which substrates may approach the catalytic center. One passageway is conical in shape, wide at the protein surface and narrow as it approaches the position opposite His504. The other path consists of a winding path, 40 Å in length, from the protein surface to the interior. This channel passes by the unoccupied site on the iron opposite His690.

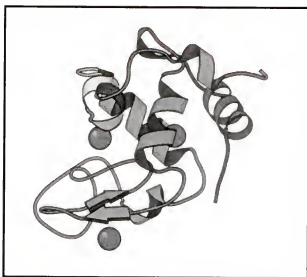


Figure 9-2. The tertiary structure of hen egg white lysozyme is presented here, with the primary regions known to bind gases such as xenon shown as blue spheres. Reprinted with permission from B.J. Gaffney.

Hen Egg White Lysozyme. As early as 1921 Fleming announced that he had found a "remarkable bacteriolytic element" present in many tissues and secretions that was able to interfere with the growth of some specific bacterial colonies. Lysozyme can be isolated from hen egg white, tears from the lacrimal glands, and in gastric and other biological secretions. As a sterilizing agent, Lysozyme catalyzes the breakdown of certain carbohydrates found in the cell walls of certain bacteria. As a component of lacrimal fluid, the enzyme protects the cornea of the eye from infection. Nature has provided hen egg white with high content of lysozyme, at a level of about 3% of the egg white.¹⁷⁷

Site II in hen egg white lysozyme (Hel), depicted in **Figure 9-2**, is actually the main site for xenon occupation, and it is, expectedly, a hydrophobic cavity. This site is void of ordered water molecules, and is, in fact, believed to be void of all moisture. This has not been proven experimentally, but the possibility has been explored in

thermodynamic calculations.¹⁶⁹ According to the data prepared by Prangé *et al.*,¹⁷¹ at a pressure of 12 bar there are four occupied sites. The fourth site is expected to have low occupancy. Sites I and IV are intermolecular sites; II and III are Intramolecular. It is also known that site II is a spherical cavity, buried deep inside the protein structure.¹⁷⁸

Experimental

Preparation of Lyophilized Proteins

Lyophilization is a freeze-drying technique by which moisture is removed from a frozen sample by sublimation of the solid moisture. These vapors are then re-condensed away from the sample. A lyophilized biological sample is much more resistant to disease and bacteria, and can be stored for much longer periods of time.

All four proteins studied in these experiments were examined in their lyophilized forms. Moisture from the samples was condensed on a rod that is kept at a low temperature. Details of the protein lyophilization are as follows: Lipoygenase (isoform SBL-1) was purified by a modification¹⁷⁹ of the procedure of Axelrod *et al.*¹⁸⁰ After purification by HPLC, the protein solution was concentrated in a B-15 Minicon (Amicon, Beverly MA) to about 1.5 mM (142 mg/mL), dialyzed against 0.02 M TRIS (pH 7.5) for 12 hours, and lyophilized in a SpeedVac concentrator (Savant, Farmingdale, NY). Methemoglobin (horse) and metmyoglobin (horse skeletal muscle) were purchased as powders from Sigma (St. Louis, MO), and hen egg white lysozyme (recrystallized three times) was obtained as a lyophilized powder from Calbiochem (La Jolla, CA). The latter

three proteins were dissolved and filtered (Millipore, 0.22 μm filter) to give solutions of 60 mg/mL in 0.02 M TRIS (pH 7.5) and lyophilized using procedures similar to the one used for SBL-1.

Generation of SEOP Enhanced ^{129}Xe

Nuclear polarization enhanced ^{129}Xe gas was prepared using the alkali atom noble gas spin-exchange optical pumping method.^{2,56,58,131} Natural abundance xenon gas at a pressure of 0.20-0.60 atm was combined with a rubidium metal droplet in a cylindrical borosilicate glass pumping cell with a total volume of 77.6 cm^3 . The temperature of the pumping cell was maintained at a temperature within the range 363 to 373 K in a magnetic field of approximately 100 G while the rubidium vapor was excited with circularly polarized light at the wavelength corresponding to the 1D line (794.7 nm). The 1.75 W beam was generated by an Argon-Ion (Coherent I-200) pumped Titanium Sapphire ring laser (a converted Coherent 899 dye laser) that was operated in multi-frequency mode.

In preparation for each SEOP ^{129}Xe NMR experiment, xenon was loaded into the optical pumping cell and polarized for a period of 20-30 minutes. The volume of the 10 mm NMR tubes used in the SEOP ^{129}Xe NMR experiments is $8.5 \pm 0.5 \text{ cm}^3$. The quantities of xenon gas optically pumped provide approximately 2 to 7 atm pressure in the sealed 10 mm NMR tube (calculated for an empty tube at 298 K).

SEOP Enhanced ^{129}Xe NMR of Lyophilized Protein Samples

The experiments were conducted using 10 mm high-resolution liquid state NMR probes on both the Varian Unity 500 MHz and the Bruker Avance 400 MHz spectrometers. A known amount of lyophilized protein (100-150 mg) was added to a 10 mm medium-wall borosilicate glass NMR tube. This tube was carefully evacuated to a pressure of 10^{-4} torr to remove excess moisture from the sample without denaturing the protein. The sample was not subjected to vacuum beyond the point at which the pressure dropped into the 10^{-4} torr regime.

The SEOP ^{129}Xe NMR spectra of **Figure 9-5** have been acquired following exposures of the solid proteins (Hel, metMb, metHb, and SBL-1) to 2.0 atm of ~2% spin polarized ^{129}Xe . All of the spectra of **Figure 9-5** were acquired on the Varian Unity 500 MHz spectrometer. The additional SEOP ^{129}Xe NMR spectra on SBL-1 presented in **Figure 9-6** were acquired on a Bruker Avance 400 MHz spectrometer at several temperatures between 173 and 223 K and at xenon pressures of 2.5 and 6.0 atm. To facilitate transfer of the SEOP enhanced ^{129}Xe from the pumping cell to the NMR tube containing the protein solid while preserving the polarization of the enhanced ^{129}Xe , the NMR tubes were immersed in a liquid nitrogen bath contained within the poles of a 0.2 T permanent magnet assembly. Following the freeze-over of xenon, the tubes were sealed, removed from the vacuum manifold, and transported immediately to the spectrometer. After inserting the sample into the NMR probe, FID acquisition was delayed 240 s to allow time for the xenon to fully sublime, and for the sample to reach the desired equilibrium temperature. Each spectrum was acquired using a single 20 μs pulse,

corresponding to a 45° flip angle. By using a flip angle of 45° rather than 90° , the ^{129}Xe nuclear magnetization inside the NMR coil is only partially destroyed, allowing multiple spectra to be acquired for each exposure to polarization enhanced xenon. Exchange of xenon in and out of the coil region by diffusion also has the effect of replenishing the magnetization, so that the reduction of the ^{129}Xe NMR signal by the application of successive rf pulses is less than would be expected if there were no exchange. Since the coil volume of approximately 1 mL is much smaller than the total tube volume of 8.5 mL, several spectra can be obtained without a significant loss in signal intensity.

After obtaining a spectrum at the initial preset temperature, additional spectra were recorded at several lower temperatures. A 120-s delay was allotted to allow equilibration of probe and sample after significant temperature changes. To confirm that the delay was sufficient to reach equilibration, an experiment was performed wherein spectra were acquired as a function of time following a temperature change. The lack of any line width or chemical shift changes after several minutes indicated that temperature equilibration was indeed complete. Furthermore, the observed gas-liquid and liquid-solid phase transition temperatures were found to coincide well with values measured by conventional ^{129}Xe NMR in a reference sample containing a Xe-O₂ gas mixture which had been allowed to equilibrate for 30 min. The signals from liquid and solid ^{129}Xe occur at ~250 ppm (depending slightly on temperature) and ~300 ppm at 173 K with respect to the 298 K xenon gas signal at 0 ppm.

^{129}Xe NMR of Protein Solutions.

NMR spectra of ^{129}Xe dissolved in solutions of SBL-1 and metMb were recorded on the Bruker Avance 400 spectrometer fitted with a high-resolution, variable temperature 10 mm probe. Reported temperatures are accurate to within ± 2 K. These spectra were recorded by thermally polarized ^{129}Xe NMR, with signal averaging of 6000 free induction decays (FIDs) and a recycle delay of 500 ms. The chemical shift scale was referenced to the 298 K xenon gas signal at 0 ppm.

The metMb sample consisted of 3.3 mM protein dissolved in a cryo-protectant solution: 50% deuterium oxide, 25% methanol, and 25% ethylene glycol. This solution was degassed by three freeze-pump-thaw cycles prior to introduction of xenon gas. The spectra were recorded at xenon pressure 2.2 atm (at 298 K) over a temperature range of 248 to 308 K in 5 or 10 K increments. The concentration of the SBL-1 sample was 50 mg/mL in a solvent composed of 70% buffer solution (0.01 M potassium phosphate buffer and 0.015 M sodium azide in 90% deuterated water) and 30% glycerol. To reduce the risk of denaturing the protein, the SBL-1 solution was degassed gradually at ambient temperature. Spectra were recorded at a xenon pressure 1.7 atm (at 298 K) for the temperature range of 248 to 303 K. The temperature across this range was incremented by 5 or 10 K for each spectrum.

Gas Adsorption Isotherm Measurements.

Methane and xenon gases were purchased from Matheson (Montgomeryville, PA), and N_2 was purchased from BITEC (Tampa, FL). All gases were 99.99% pure. For

the N₂ BET (Brunauer, Emmett, and Teller) and CH₄ gas adsorption isotherms, each protein powder solid was degassed for ~8 hours under a vacuum (10^{-4} torr) at 77 K. Prior to recording the xenon adsorption isotherms, each protein powder solid was degassed for ~8 hours under a vacuum of 10^{-4} torr at the following temperatures: SBL-1, 263 K; metMb, 293 K; and Hel, 293 K.

Nitrogen adsorption isotherms at 77 K were performed using a Micromeritics (Norcross, GA) ASAP 2000 gas analyzer. The BET surface areas were determined using a five-point BET calculation.^{181,182} Gaseous uptake of CH₄ and xenon on the protein powder solids was measured at 210 K on the Micromeritics ASAP 2000 instrument with chemisorption/physisorption software employing a 75-point pressure table ranging from 0.1 torr to 760 torr. The system was considered to be at equilibrium when the pressure change was less than 1% of the selected pressure point in a 20-s equilibration time interval. Pressure tolerances were 1% with the 10 torr transducer and 1 millitorr with the 1000 torr transducer. Low-temperature baths consisting of a solvent/liquid nitrogen mixture were employed to collect isotherms at low temperatures.¹⁸³ The temperatures of the baths were maintained to within ± 1 K.

Results and Discussion

Solution State ^{129}Xe NMR.

The 110.7 MHz ^{129}Xe spectra in metMb solution, recorded as a function of temperature, are presented in **Figure 9-3a**. This series can be directly compared with the 27.7 MHz spectra of Tilton and Kuntz.¹⁶⁰ Note that for these experiments, horse muscle myoglobin was used, whereas Tilton and Kuntz had studied myoglobin extracted from a sperm whale. Dependences of the spectral line width and of the chemical shift on sample temperature are shown in **Figure 9-3b**. In general, the features of the original ^{129}Xe NMR temperature dependence in the metMb solution are well reproduced, albeit with higher dispersion and signal:noise due to improvements in NMR instrumentation since the original work. A maximum linewidth of 860 Hz is observed at a temperature of 263 K. The ^{129}Xe signals observed in **Figure 9-3** exhibit a maximum upfield resonance shift of 7 ppm (3.3 mM metMb), whereas a maximum shift of ~ 12 ppm had been found in the original study at higher protein concentration (8 mM).¹⁶⁰ In addition, no discernible peak in the 0-300 ppm range could be attributed to xenon bound to metMb in the slow to intermediate exchange regime, a feature that had been detected by Tilton and Kuntz.¹⁶⁰

The 110.7 MHz spectra of ^{129}Xe dissolved in a 50 mg/mL (0.5 mM) SBL-1 solution, recorded over a temperature range of 263-303 K, are presented in **Figure 9-4a**. The discontinuity in the chemical shift and line width appearing at 263 K corresponds to freezing of the protein/cryo-protectant solution. Because denaturing of SBL-1 occurs with unfolding of the protein at elevated temperatures¹⁸⁴ ($T_m > 333$ K), the maximum

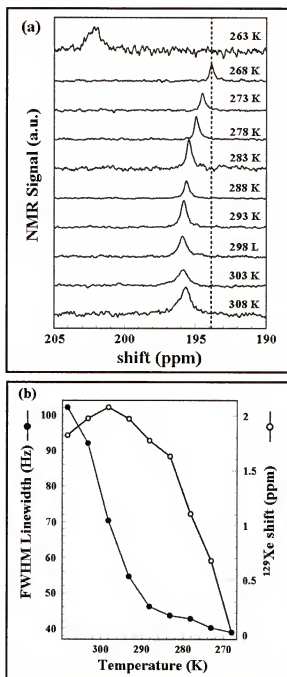


Figure 9-3. The conventional ^{129}Xe NMR spectra, depicted in (a), was acquired as a function of temperature for a solution containing 3.3 mM metMb in 0.50 mL of ethylene glycol, 0.50 mL of methanol, and 1.0 mL of D_2O . The 8.5-mL volume sample tube contained 2.2 atm (298 K) of xenon. Fourier transformed spectra were acquired by signal averaging 6000 FIDs with a 500-ms recycle delay. The summary of the temperature dependence of the ^{129}Xe NMR line widths (●) and line shifts (○) in the metMb sample is presented as (b).

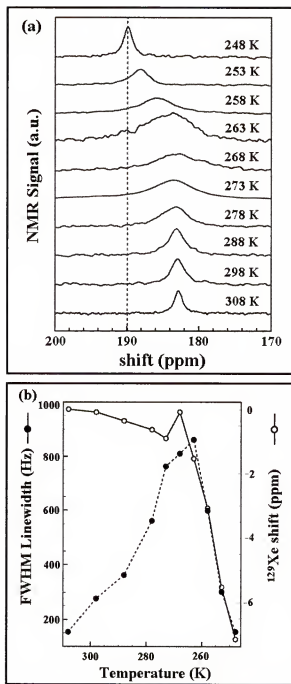


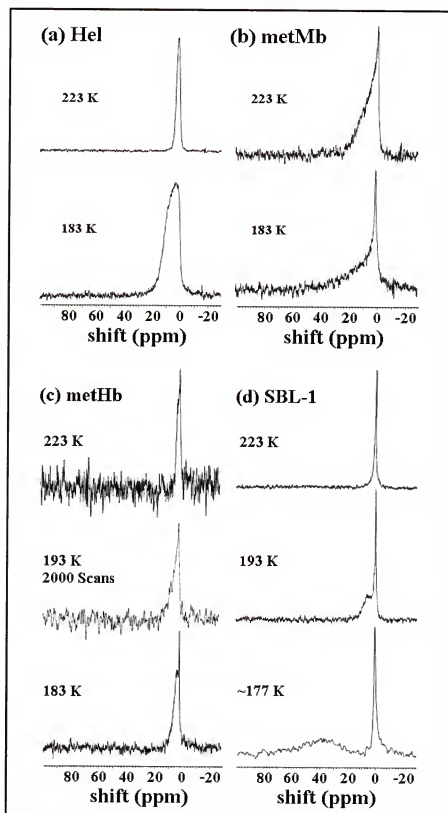
Figure 9-4. The conventional ^{129}Xe NMR spectra are depicted in (a) for a 1 mL solution containing 50 mg of lipoxygenase, type SBL-1 from soybeans, dissolved in a 0.01 mM potassium cryoprotectant solvent. The spectra were acquired as a function of temperature at a Xe pressure of approximately 1.7 atm. A total of 4000 FIDs were signal-averaged using a recycle delay of 500 ms. The summary of the temperature dependence of the ^{129}Xe NMR line widths (●) and line shifts (○) in the SBL-1 sample is depicted in (b).

temperature investigated by solution NMR was 303 K. **Figure 9-4b** shows that both the line width and chemical shift vary nonlinearly with temperature and appear to reach maximum values near 303 K. These observations are consistent with xenon exchanging between the binding sites on the protein and the solvent in the slow to intermediate exchange regime. At no temperature within the range studied was a distinct ^{129}Xe resonance corresponding to xenon bound to SBL-1 in the slow exchange regime observed.

SEOP Enhanced ^{129}Xe NMR Studies on Lyophilized Proteins.

Figure 9-5a-d presents the 138.4 MHz SEOP enhanced ^{129}Xe NMR spectra of xenon in contact with each lyophilized protein (Hel, metMb, metHb, and SBL-1) at 193 and 223 K. The final xenon pressure in each sample corresponded to 2.0 atm at 298 K. The 193 K spectrum of **Figure 9-5c** was obtained from a sample containing thermally polarized ^{129}Xe by signal averaging 2000 FIDs with a 1-s recycle delay, 90° rf pulses; the resulting NMR line shape is consistent with the line shapes of the polarization enhanced ^{129}Xe NMR spectra obtained at higher and lower temperature. Although the spectra derived from thermally polarized and SEOP polarized ^{129}Xe have similar signal-to-noise ratios, it should be emphasized that the SEOP enhanced ^{129}Xe spectra were acquired in only a single scan using a 45° rf pulse. Use of this smaller flip angle prevented rapid depletion of the ^{129}Xe polarization. This made it possible to acquire ^{129}Xe NMR spectra at several different temperatures in a single optical pumping run. Exchange of xenon between the protein surface and the gas-phase has the effect of replenishing the xenon

Figure 9-5. SEOP enhanced ^{129}Xe NMR study of xenon adsorption on 100-150 mg samples of lyophilized powders of (a) hen egg white lysozyme (Hel), (b) metmyoglobin (metMb), (c) methemoglobin (metHb), and (d) soybean lipoxygenase (SBL-1) at several temperatures, as indicated. The spectra have been normalized to the maximum intensity in each spectrum, and no correction has been applied to account for the loss of xenon spin magnetization by spin lattice relaxation or rf pulses. Except for the 193 K spectrum of part (c), the ^{129}Xe NMR spectra were all recorded at 138.4 MHz using a single 45° pulse (20- μs pulse width) in the presence of enhanced xenon gas at a pressure equivalent to 2.0 atm at room temperature. The samples were thermally equilibrated for several minutes prior to acquisition. The 193 K spectrum of (c) is a conventional (field-polarized) ^{129}Xe NMR spectrum acquired at 110.7 MHz by signal averaging 2000 FIDs with a 1-s recycle delay.



magnetization, especially at the higher temperatures, thus mitigating destruction of the xenon magnetization through successive rf pulses.

Note that the vertical axes of the spectra in **Figure 9-5** are normalized to the maximum intensity in each case. The apparent variation in the signal-to-noise ratio for each temperature series depends not only on the history of pulses and relaxation during delays between FID acquisitions, but also on amount of xenon adsorbed by the sample and the change in the NMR line width as the temperature is reduced. In view of the inability to obtain a good estimate of the effect of all these factors, no attempt has been made here to interpret the relative intensities of the ^{129}Xe signals.

The line shapes presented in **Figure 9-5** are qualitatively different for all four proteins. The 177 K spectrum of SBL-1 exhibits a particularly well-resolved protein-associated ^{129}Xe resonance shifted downfield from the gas peak by about 35 ppm. In metHb, the broad component becomes resolved from the gas peak as the temperature is lowered, while in Hel and metMb no distinct resonance is observed. In Hel and metMb, moreover, the line shape broadens and becomes increasingly asymmetric with decreasing temperature.

The spectra of metMb show an asymmetrically broadened peak with a tail extending downfield to about 40 ppm. After several minutes, the "bound" ^{129}Xe peak in the metMb sample decayed below the limit of detection, while the signal from the gas phase peak could be observed for as long as 320 s. The NMR spectra of the metHb sample exhibited a resolved adsorption peak with a small (~ 2 ppm) downfield shift from the gas-phase peak. Note that the intensity of the gas phase ^{129}Xe peak represents only a

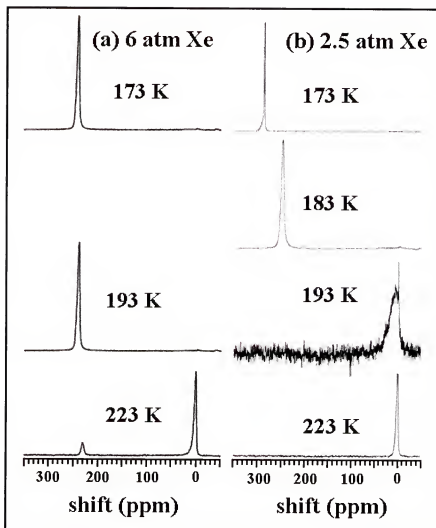


Figure 9-6. SEOP Enhanced ^{129}Xe NMR study of xenon adsorption on 142 mg of lyophilized soybean lipoxygenase (SBL-1) exposed to (a) 2.5 atm (298 K) and (b) 6.0 atm of enhanced xenon. At each pressure, spectra are shown for several different temperatures. The sample was thermally equilibrated for several minutes prior to recording the 110.7 MHz spectra in a single scan following a 45° pulse. The spectra have been normalized to the maximum intensity in each spectrum, and no correction has been applied to account for the loss of xenon spin magnetization by spin-lattice relaxation or rf pulses.

small fraction of the total amount of xenon in the lyophilized protein samples due to the displacement of the gas by the protein solid in the detected volume of the sample tube.

The line width of the signal of ^{129}Xe bound to metHb was narrower (~ 5 ppm FWHM) than the line width of the signal obtained with metMb.

Adsorption of nuclear polarization enhanced ^{129}Xe onto lyophilized Hel yielded ^{129}Xe NMR peaks at ~ 5 ppm at 223 K and ~ 12 ppm at 183 K. The narrow resonance due to gaseous xenon was not resolved in the Hel spectra. Unlike the other proteins studied, Hel is not paramagnetic, and hence the nuclear spin relaxation mechanism due to coupling with unpaired electrons is not present in Hel. This probably accounts for the comparatively higher intensity of the ^{129}Xe signal in Hel as well as its persistence for over 480 s.

The SEOP ^{129}Xe NMR spectra of SBL-1 at several different temperatures and at xenon pressures corresponding to 2.5 and 6.0 atm at 298 K are presented in **Figure 9-6**. The spectra have been normalized to the maximum intensity. In the 2.5 atm series, a broad (~ 30 ppm FWHM) but resolved peak develops at temperature 193 K. Upon lowering the temperature to 183 K, a strong peak appears at 250 ppm-evidence for a phase transition to liquid xenon. In the 6.0 atm series, the liquid xenon peak is initially observed at 223 K, with a shift of 230 ppm. The temperatures corresponding to the xenon gas-liquid phase transition for pressures 2.5 and 6.0 atm (pressures at 298 K) were independently established by conventional ^{129}Xe NMR on sealed xenon gas reference samples. The phase transition temperatures were the same in the gas reference and protein samples to within expected error, indicating that the presence of protein does not substantially alter the thermodynamics of xenon liquefaction. The reported shifts in the positions of the adsorbed peaks and the changes in line width of the gas phase peak with

temperature are consistent with a dynamic equilibrium between gas phase xenon and gas adsorbed onto the protein surface.

The following facts are relevant to the interpretation of the ^{129}Xe NMR spectra. The large chemical shift range of ^{129}Xe in different chemical environments affords a characterization of the xenon binding in both the solution and solid phases. Proteins can offer a large diversity of potential xenon binding sites, including surface exposed pockets, internal cavities or void spaces, and channel pores.¹⁶¹ These sites may be lined with aliphatic, aromatic, or polar groups and could even involve reconfiguration or displacement of waters. Fluctuations in side-chain conformations are also thought to contribute to creating sites for xenon binding in proteins.¹⁶⁹ Although sites for xenon binding in proteins can be located by X-ray methods, NMR has the advantage of being able to characterize the binding dynamics in both the solid or solution phases. Polarization transfer from SEOP enhanced ^{129}Xe to nuclei of residues near xenon binding sites in proteins will be particularly important in determining structure in proteins for which crystal structures are not available.

In the experiments on the lyophilized samples, each protein yielded a distinct ^{129}Xe NMR line shape (**Figure 9-5**). In the range of temperatures from 183 to 223 K, the NMR chemical shift of the adsorbed component varied from 0 to 40 ppm, relative to the free gas signal. The signals broadened and shifted downfield as the temperature was lowered. Although discrete peaks due to xenon bound to protein are not observed in metMb and Hel, the line shapes do become increasingly asymmetric as the temperature is lowered, and the intensity of the downfield side of the line shape increases

correspondingly. A reasonable explanation for this behavior is that the xenon is undergoing exchange between the gas and several unresolved sites associated with the surface or cavities. The broad tail of the line shape observed for metMb is consistent with the multiple sites (up to five at a pressure of 2 atm)^{161,169} which have been detected in X-ray measurements of crystals and in calculations. The observation of a relatively narrow peak in metHb is consistent with a single type of xenon binding site, as reported previously¹⁵⁹ for this protein. X-ray studies of Hel crystals revealed two intramolecular xenon-binding sites.¹⁶¹ Although the Hel and metMb spectra do not show fully resolved binding sites, the asymmetric shape of the peaks observed does suggest the presence of more than one type of binding site in these proteins.

The largest observed ¹²⁹Xe chemical shift resulted from adsorption onto 142 mg of SBL-1 at a pressure corresponding to several atmospheres of xenon (at 298 K). Adsorbed peaks can be seen, at 10 ppm at 193 K and 35 ppm at ~177 K (**Figure 9-5d** and **Figure 9-6b**). The experimental conditions correspond to a large molar excess of xenon over protein. The internal cavity in soybean lipoxygenase-1 is referred to as cavity II, to distinguish it from a pocket known as cavity I that is open to the surface. Cavity II has two lobes and is lined by side chains of about 61 residues.^{157,166} Calculations of the solvent-exposed surface area¹⁸⁵ of these side chains give an approximately linear increase from 10 to 1000 Å² for probe radii ranging from 2.5 to 1.0 Å, respectively. The accepted radius of xenon (2.1 Å) is on the large side of this range, but the calculations suggest that the exposed surface area in cavity II of SBL-1 could accommodate binding of multiple xenon atoms. The differences between SBL-1 and the other proteins, with respect to

xenon binding, could also reflect the larger mass of SBL-1 (100 kDa) which may provide a greater number of buried sites capable of accommodating a xenon atom than the smaller proteins of 14-17 kDa mass.

Results of the thermally polarized ^{129}Xe NMR study of metMb and SBL-1 solutions provide additional information. The previous observations of Tilton and Kuntz¹⁶⁰ demonstrated that xenon undergoes exchange between bound and free forms in the presence of metMb, with the bound signal exhibiting an upfield shift with respect to the chemical shift of xenon in solvent. They showed by extrapolation to infinite protein concentration that the chemical shift of ^{129}Xe bound to metmyoglobin in aqueous solution at 273 K is ~ 44 ppm from the signal of ^{129}Xe dissolved in solvent or about 153 ppm downfield from the gas-phase ^{129}Xe signal. The ^{129}Xe signal in the metMb solution is broadest at about 264 K and is sharper above and below this temperature. In agreement with this prior study, the data presented here is consistent with a transition from the fast to intermediate exchange regime near 264 K, but at 248 K. The second broad signal attributed by Tilton and Kuntz¹⁶⁰ to the bound component in slow exchange was never observed in the current study. It should be noted that our measurements are made at about four times higher Larmor frequency and at one-third lower protein concentration than in the original study. Under our conditions, increased paramagnetic broadening at higher magnetic field may render the bound signal more difficult to observe than in the lower field study of the original work, and in addition, the lower protein concentration in our work would further diminish the possibility of detecting the bound signal. The temperature at which the transition from rapid to slow exchange occurs is approximately

the same in both experiments, a finding consistent with small activation energy for the exchange. Chemical shifts of ^{129}Xe in the solvent alone (50% D_2O , 25% methanol, 25% ethylene glycol) do not reveal any phase transitions between 273 and 303 K.¹⁶⁰

An alternative interpretation of the broadening of peaks in the metMb solution over the range of temperatures from 278 to 253 K (**Figure 9-3a**) is that metMb undergoes "cold denaturation" in this range.¹⁸⁶ Under that interpretation, two forms of protein, native and unfolded, are in equilibrium, and xenon is in rapid exchange between the solvent and the two protein environments. Studies of cold denaturation of metMb¹⁸⁶ show that a transition at about 263 K would be associated with a pH around 4 rather than the pH of our experiment (pH^{25°C} 7.4, 0.02 M TRIS). However, cold denaturation of metMb has not been examined in the cryoprotectant solvent system used in our experiments, so further studies are necessary to fully rule out this alternative explanation for the observed temperature dependence of the linewidth and line shift in the solution-state ^{129}Xe NMR.

In lipoyxygenase solutions, increasing the temperature from 268 to 303 K results in an increase in the ^{129}Xe NMR line width and a downfield change of the chemical shift. Higher temperatures were not studied to avoid thermal denaturation of SBL-1.¹⁸⁴ The sign of the change in chemical shift is opposite to that observed in metMb, whereas the signal in the fast exchange limit is shifted upfield with respect to ^{129}Xe in solvent in metMb. In methHb, on the other hand, Tilton and Kuntz¹⁶⁰ report a downfield shift in the solution state. These differences in the direction and magnitude of the paramagnetic shift change may be attributed to differences in the relative orientation and proximity of xenon to the unpaired electron in these paramagnetic proteins. No peak that might be attributed

to xenon bound to SBL-1 at low temperature was observed over the 0 to 300 ppm range. Again, this could be due to several factors, such as a low fractional occupancy of the bound state at 1.7 atm, the relatively low protein concentration, or severe paramagnetic broadening of the bound ^{129}Xe signal.

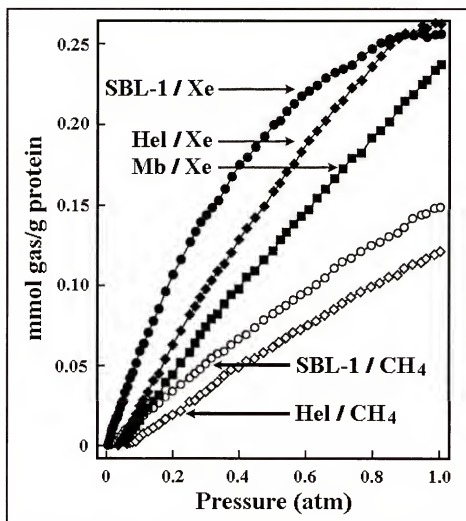
N_2 , Xe and CH_4 Gas Adsorption Isotherms.

The binding of xenon, methane, and nitrogen to the protein samples in the lyophilized state was also characterized by adsorption isotherm analysis. The adsorption of xenon on SBL-1 reaches a plateau near 1.0 atm, suggesting near saturation of the adsorption sites, while the other proteins appear to continue to adsorb more xenon at pressures exceeding 1.0 atm (**Figure 9-7**). **Table 9-1** summarizes the xenon adsorption data. On a per gram basis, all three proteins adsorbed similar amounts of xenon at 1.0 atm. On a per mole basis, SBL-1 adsorbs 25 xenon atoms per protein molecule at 1.0 atm pressure whereas metMb and Hel adsorb only about 4 xenon atoms per molecule of protein. SBL-1 and metMb exhibit lower affinities for CH_4 than for xenon. As reported in **Table 9-1**, the 77 K N_2 adsorption isotherms for SBL-1, Hel, and metMb yielded BET surface areas of 504, 23.3, and 13.0 m^2/g , respectively.

A lyophilized SBL-1 sample that had been subjected to several rounds of ^{129}Xe NMR experiments and to the adsorption isotherm measurements (over a period of a few months) still retained 50% of the original specific activity. The prolonged activity of the protein confirmed that the integrity of the protein was preserved throughout the duration

Table 9-1. Parameters from Adsorption Isotherm Data for Lyophilized Proteins

Protein	N ₂ BET surface area (m ² /g)	mmol Xe adsorbed per gram of protein	Mol Xe asorbed per mol protein ^a
Hel	13.0 ± 0.7	0.262	3.67
metMb	23.3 ± 3.6	0.237	4.00
SBL-1	504 ± 9	0.256	25.1

^a At a pressure of 1 atm.**Figure 9-7.** Xenon and methane adsorption isotherms for binding at 210 K to lyophilized proteins, lipoxxygenase (SBL-1), metmyoglobin (metMb), and hen egg white lysozyme (Hel). Adsorption data is also reported in Table 9-1.

of the ^{129}Xe NMR experiments. Solution state ^{129}Xe NMR experiments with SBL-1 were performed on a separate sample having specific activity $180 \pm 10 \text{ mol min}^{-1} \text{ mg}^{-1}$.

The xenon adsorption isotherms at 210 K show that SBL-1, metMb, and Hel bind approximately the same quantity of xenon per gram of protein at a xenon pressure of 1.0 atm. The curvatures of the binding isotherms, however, demonstrate that SBL-1 approaches saturation at 1.0 atm. In metMb and Hel, the xenon adsorption is still nearly linear with gas pressure. The xenon adsorption isotherm for a metMb/water solution at room temperature has been published,¹⁷⁰ and those experiments showed saturation as the xenon pressure approached 5.0 atm. The higher affinity of SBL-1 for xenon per unit mole of protein is therefore evident, though not unique to this gas, since SBL-1 also has a higher affinity for methane relative to the other proteins examined.

The N_2 BET surface areas of **Table 9-1** show that the available surface area *per gram* of protein in SBL-1 is much higher ($504 \text{ m}^2/\text{g}$) than for metMb, metHb, and Hel, per gram of protein. As a result of the smaller size of nitrogen and the fact that the experiments were performed below the critical temperature of N_2 , it may be concluded that N_2 has greater access to the internal surface structure and that liquefaction of the gas is involved in the adsorption process. The dramatic difference in the nitrogen and xenon adsorption behavior in SBL-1 indicates that no liquid xenon forms up to a pressure of 1.0 atm at 210 K, a finding supported by the lack of any liquid ^{129}Xe NMR signal at this same temperature and at even higher pressures.

Conclusions

Presented here are the first SEOP ^{129}Xe NMR spectra obtained for the noble gas in the presence of lyophilized protein powders: soybean lipoxygenase, methemoglobin, metmyoglobin, and hen egg white lysozyme. The ^{129}Xe NMR signal enhancement afforded by spin exchange optical pumping dramatically illustrates the advantage of using polarization enhanced ^{129}Xe in protein studies. While it is possible to obtain adequate ^{129}Xe NMR spectra with considerable signal averaging in the case of a paramagnetic protein such as methemoglobin, this will probably not be practical for diamagnetic proteins such as lysozyme. Moreover, it is possible to obtain reproducible spectra at several different temperatures by using the large reservoir of nuclear polarization generated in a single optical pumping run.

Each lyophilized protein exhibited a distinct and reproducible ^{129}Xe NMR line shape. The small shifts of the ^{129}Xe resonances observed suggest that the peaks are due to surface-bound xenon in exchange with gaseous xenon in the slow to intermediate rate regimes. The protein-associated peak in lipoxygenase was more distinct than in the other proteins. This could be attributed to the large channel pore in this particular protein-an explanation that is consistent with the greater BET surface area and greater xenon uptake as observed by independent gas adsorption measurements. Polarization transfer experiments could help to unambiguously resolve this issue.

The xenon phase diagram ultimately constrains the pressure and temperature range over which the protein-bound ^{129}Xe signals can be observed. If the pressure is too

high or the temperature too low, xenon condenses into a bulk phase that yields no information about the xenon-protein interaction. In addition, such conditions will not produce effective polarization transfer to nuclei of the protein. Our SEOP ^{129}Xe NMR studies reveal two possible strategies for observing xenon bound to internal cavities in lyophilized proteins. In the first approach, a relatively high pressure and high temperature achieve a high fractional occupancy of the xenon binding. Alternatively, the adsorption may be done at relatively low pressure and low temperature, where the enhanced ^{129}Xe will not condense into a bulk phase and will be present at a concentration comparable to the density of xenon binding sites on the protein. The first approach should even be amenable to studies of paramagnetic proteins because the xenon will be in fast exchange with excess polarized xenon in the gaseous state. In the latter approach, it is clear that a higher xenon polarization will be required, and the immobilized xenon will experience rapid spin-lattice relaxation if the binding site is in close proximity to a paramagnetic center.

Lysozyme is an ideal candidate for a ^{129}Xe - ^1H or ^{129}Xe - ^{13}C polarization transfer experiment because it is diamagnetic and exhibits both X-ray and NMR evidence for xenon binding. Hel can accommodate an isotopically enriched substrate molecule that could also be the target of polarization transfer enhancement. Competitive binding studies can also be envisaged. For instance, if xenon is found to be competitive with O_2 binding in SBL-1, then it may be possible to trap an enzymatic intermediate state involving simultaneous binding of both xenon and the fatty acid substrate. Demonstrating

polarization transfer from the nuclear polarization enhanced ^{129}Xe to the ^1H or ^{13}C nuclei of the substrate could prove the existence of such an intermediate.

APPENDIX I
EXPERIMENTAL APPARATI FOR THE GENERATION OF
SEOP ENHANCED ^{129}Xe NMR

Table-Top System

Generation of SEOP Enhanced ^{129}Xe Gas

A schematic diagram of the apparatus used to generate spin polarized ^{129}Xe gas after spin exchange with optically pumped rubidium metal vapor is provided as **Figure AI-1**. A cylindrical borosilicate glass cell having a volume of $77.6 \pm 0.2 \text{ cm}^3$ serves as the pumping cell for this apparatus. The inner surfaces of the cell have been coated with a thin layer of octamethyldichlorotetrasiloxane, under the manufacturing label of Surfasil (Pierce Scientific). The cell has been prepared to receive the coating first by conditioning the inner surfaces with *Aqua Regia* (3 parts HCl to 1 part HNO_3), then allowing the cell to completely air dry under nitrogen for several hours. The coating was delivered as directed by Pierce Scientific, using several washings of a 1-2 % siloxane solution in dry heptane, then by application of vacuum overnight to remove excess solvent and to drive off water resulting from siloxane condensation with the borosilicate surface. A sidearm to the pumping cell serves as a rubidium reservoir, which is filled with several droplets of the alkali metal. A removable valve above the reservoir provides easy refilling of the reservoir.

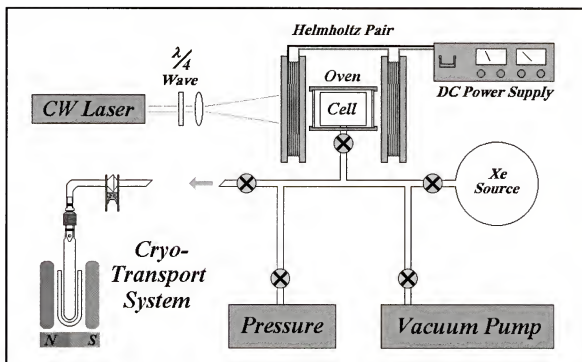


Figure AI-1. Diagram of an $Rb-^{129}Xe$ SEOP apparatus mounted atop the laser table. The manifold is permanently attached to the pumping cell. Details of the components are discussed in the text.

A heated nitrogen stream and a specially constructed oven maintain the pumping cell at a temperature between 80 and 120 °C. During the generation of SEOP enhanced ^{129}Xe , the pumping cell and oven are maintained inside a homogeneous magnetic field of ~ 100 G, which is provided by a pair of Helmholtz coils. Therefore, the oven materials must not perturb the magnetic field applied across the pumping cell. Two borosilicate windows at opposing ends of the oven allow transmission of the excitation beam through the cell, and measurement of absorbance of the beam by the alkali metal vapor.

The pumping cell is irradiated at the D_1 resonance line of rubidium (794.7 nm) by an Argon-ion pumped Titanium Sapphire tunable laser (Coherent Inova; Coherent 899

Ring Laser), operated in multi-frequency mode. Left circularly polarized light (σ^+) is selected by passing the excitation beam through a $\lambda/4$ -wave plate. The beam is then expanded to irradiate the cell as efficiently as possible. Changes in the rubidium absorption profile due to cell temperature, pressure and magnetic field differences are accommodated by tuning the laser to the resonance line while monitoring the fluorescence or absorption of the alkali metal vapor. A photodiode and oscilloscope are used to monitor this absorption profile.

High vacuum is preserved throughout the experiment to prevent oxygen from contaminating the manifold. (A Balzers Turbomolecular Pump supplied high vacuum conditions.) The pumping cell is filled with natural abundance xenon (Matheson Gas) and heated to 100-120 °C. After approximately 30 minutes of continuous laser excitation, the cell is allowed to cool to separate the rubidium from the xenon gas. To collect the SEOP enhanced ^{129}Xe gas, the manifold is opened to a 10 mm NMR tube immersed in a liquid nitrogen bath, and maintained at a field of ~ 1.5 kG by a pair of permanent ferromagnets. Xenon solidifies rapidly in liquid nitrogen, and magnetization of the sample may be preserved without significant loss of polarization for the time necessary to transport it to the NMR spectrometer.

Modification of the SEOP ^{129}Xe Cryo-Transport System

The inability to achieve rapid sample temperature equilibration to a desired probe temperature is a shortcoming of cryogenically transferring SEOP enhanced ^{129}Xe from the pumping cell to the sample tube. In addition, solid xenon is in direct contact with the

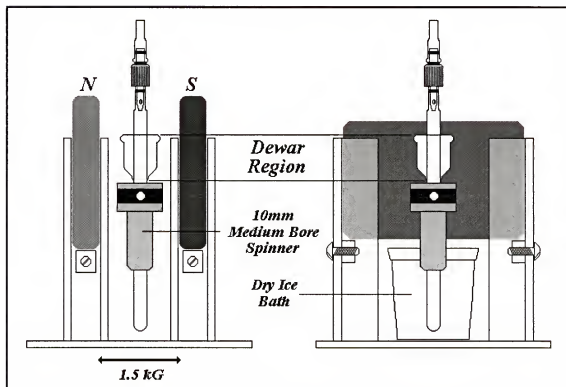


Figure AI-2. Modified 10 mm O.D. medium wall NMR tube. The tube has been modified with a 28 mm O.D. dewar in the upper region of the tube. Xenon may be condensed in its solid form above the sample, which itself can be maintained at the desired sample and NMR probe temperature until insertion into the spectrometer.

surface of the sample during transport of the sample from the cryo-transport system to the spectrometer. To alleviate both of these limitations, both the 10 mm medium-wall NMR tube and the cryo-transport system were modified, as shown in **Figure AI-2**.

The sample tube itself was altered by the permanent attachment of a borosilicate dewar, of maximum outer diameter allowable by the bore of the spectrometer. Permanent magnets of the cryo-transport system were raised to maximize the strength of the field applied across the dewar, but also to accommodate the addition of a dry-ice bath, which could be maintained at the temperature of the NMR probe, prior to insertion into the

spectrometer. In this manner, the sample temperature would be equilibrated to that of the NMR probe, and would allow minimal exposure of the sample to the SEOP enhanced ^{129}Xe gas.

Spectrometer-Top, Stopped Flow System

The schematic diagram of the apparatus used to generate spin-polarized ^{129}Xe directly atop the Bruker Avance 400 spectrometer is depicted in **Figure AI-3**. The magnet-top system incorporates the advantages of the laser table-top system: (1) the sample is maintained at the desired probe temperature throughout the generation of SEOP ^{129}Xe gas; (2) the sample can be manipulated and evacuated without disruption of the optical pumping process; (3) contact of the sample with xenon gas is prevented until the desired time. This new configuration, however, also allows for use of N_2/Xe mixtures, which improve greatly enhancements of the ^{129}Xe nuclear spin polarization. In addition, sample contact with xenon gas is completely prohibited until the gas has completely sublimed, thereby allowing for more well-defined starting times for kinetics experiments.

A cylindrical borosilicate glass cell with volume 97.6 cm^3 is coated with Surfasil by the same procedure described in the previous section. The pumping cell is filled with several droplets of rubidium metal, which are chased to the bottom edge of the cell to minimize laser reflection from the shiny metallic surfaces of the droplets. During the generation of SEOP enhanced ^{129}Xe , the pumping cell and heating devices are located inside a homogeneous magnetic field of $\sim 100\text{ G}$, provided by a pair of Helmholtz coils. The pumping cell is irradiated at the D_1 resonance line of Rb (794.7 nm) by an Argon-ion

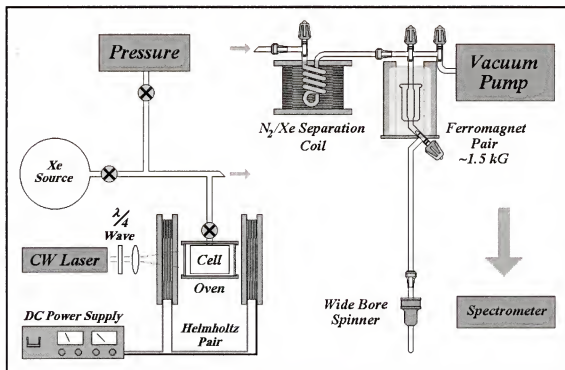


Figure AI-3. Diagram of an $Rb-^{129}Xe$ SEOP apparatus mounted atop the *Bruker Avance 400* spectrometer. The manifold, N_2/Xe separation coil and pumping cell are attached through high pressure Rotaviss® connectors. All other components are designed similar to those discussed for the laser tabletop system.

pumped Titanium Sapphire tunable laser (Coherent Inova; Coherent 899 Ring Laser), operated in multi-frequency mode. Left circularly polarized light (σ^+) is supplied by passing the excitation beam through a $\lambda/4$ wave plate. Absorption by rubidium at the D_1 resonance line is monitored using a photodiode directed orthogonal to the axis of the laser excitation beam.

As discussed previously, high vacuum is maintained throughout the manifold for the duration of the experiment. The pumping cell is filled with natural abundance xenon (Matheson Gas) and heated to 120–130 °C. After approximately 20 minutes of laser

excitation, the pumping cell is allowed to cool before SEOP enhanced ^{129}Xe is to be collected. When N_2/Xe mixtures are used, the glass portion of the separation coil is immersed in liquid nitrogen, the stopcock of the pumping cell is opened, and a flow of the gas is directed by opening the stopcock to the vacuum carefully. (A current of about 18 A is applied to the separation coil, only for the duration of the separation and the transfer to the permanent magnet storage system at the top of the magnet bore.) Once all of the nitrogen has been separated from the solid xenon, a valve at one end (closest to the pumping cell) is closed, and the gas is allowed to expand. Liquid nitrogen is added to the dewar found inside the ferromagnet pair (see **Figure AI-3**) to condense the SEOP enhanced ^{129}Xe in the stronger storage field (~ 1.5 kG) supplied by the permanent magnets. Finally, the region of the dewar is sealed off, the nitrogen is removed from the dewar to allow complete sublimation of the SEOP ^{129}Xe , and the gas can be expanded when desired by opening a stopcock valve found just below the dewar region of the transfer line.

APPENDIX II CALCULATING THE ^{129}Xe NMR SIGNAL ENHANCEMENT

Measuring Nuclear Spin Polarization

For a spin $\frac{1}{2}$ nucleus such as that of ^{129}Xe in an applied magnetic field, there are only two spin states, where the lower energy state is typically denoted α , for the $m_s = +\frac{1}{2}$ spin state, and β , for the $m_s = -\frac{1}{2}$ state. At thermal equilibrium, under the applied magnetic field of strength B (expressed in Tesla), the energy of separation, ΔE (in Joules), of the α and β states is given by equation AII-1,

$$\Delta E = \gamma \hbar B, \quad (\text{AII-1})$$

where γ is the gyromagnetic ratio in MHz T^{-1} of the nucleus of interest and $\hbar = h/2\pi$, for h being Planck's constant (6.626×10^{-34} J s). For the population of the α spin state being given by N_α , and of the β spin state by N_β , we have a Boltzmann relationship,

$$\frac{N_\alpha}{N_\beta} = \exp\left(-\frac{\Delta E}{kT}\right), \quad (\text{A-2})$$

where k is the Boltzmann constant ($1.381 \times 10^{-23} \text{ J K}^{-1}$), and T is the absolute temperature of the sample. The polarization of the sample, P , is then defined by equation A-3,

$$P = \frac{N_{\alpha} - N_{\beta}}{N_{\alpha} + N_{\beta}}. \quad (\text{A-3})$$

Rearrangement and substitution of equation AII-2 into AII-3, and also applying the approximation $\exp(-\Delta E/kT) \approx 1 - \Delta E/kT$ (Taylor series expansion), provides us with the relationship

$$P \approx \frac{\Delta E}{kT}. \quad (\text{AII-3})$$

Since we determined the value of ΔE in equation AII-1 with respect to the strength of the applied field, B , we have

$$P \approx \frac{\gamma \hbar B}{kT}, \quad (\text{AII-4})$$

which then provides the more easily used relationship,

$$P \approx \frac{h \nu_L}{kT}, \quad (\text{AII-5})$$

where ν_L refers to the Larmor frequency in Hertz of the nucleus of interest.

For the measurement of SEOP ^{129}Xe NMR signal enhancements on the Varian Unity 500, a thermal standard was prepared in a medium-wall tube made of the same borosilicate glass as the sample tube. The tube was pressurized to with a mixture of 654.3 torr of natural abundance xenon gas and 270 to 290 torr of oxygen gas. To know the ^{129}Xe polarization, we require only the Larmor frequency (138.30 MHz, at 11.744 T) and the temperature. Substitution into equation A-5 reveals a polarization of 0.00111 % for the ^{129}Xe nuclei at room temperature (298 K). For measurement of the signal enhancements on the Bruker Avance 400, the thermal standard was a medium-wall flame sealed tube, with 5.00 atm (3.80×10^3 torr) of xenon gas, and 250 to 270 torr of oxygen gas. For the Larmor frequency (110.68 MHz, at 9.395 T), and room temperature (298 K), substitution into equation A-5 reveals a polarization of 0.000891 %.

In general, one is concerned more directly with the enhancement of the signal and the absolute signal intensity that is observed. The enhancement factor for the SEOP enhancement of the ^{129}Xe NMR signal, therefore, is more frequently calculated. Calculation of the enhancement factor requires normalization of the ^{129}Xe NMR signal of the thermally equilibrated sample for several factors: (1) the number of FIDs in the signal averaging; (2) the pressure of the thermally equilibrated sample; (3) differences in the tip angle (rf pulse width). Since natural abundance xenon gas was used for both the thermal standard and the SEOP enhanced ^{129}Xe sample, we can neglect this feature in the calculation of the enhancement factor.

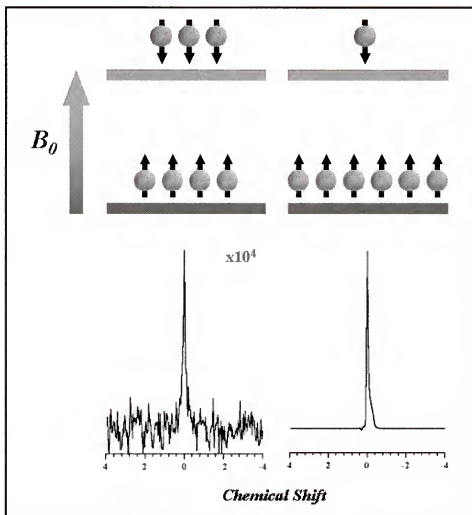


Figure AII-1. Enhancement of the ^{129}Xe NMR signal obtained through spin exchange with optically pumped rubidium vapor with the magnet-top system. The spectrum for the thermally equilibrated standard (lower left) was acquired for a sample 777 torr in xenon, with 90° tip angle rf pulses, and was signal averaged over 512 FIDs. The spectrum for the SEOP enhanced sample (lower right) was acquired through a single scan, 30° tip angle rf pulse, for a sample 748.8 torr in xenon.

For example, with the magnet-top system described in Appendix I, a thermal standard consisting of 777 torr of xenon and 250 - 290 torr of oxygen was used. The spectrum of the thermal reference, shown in the lower left of **Figure AII-1**, was acquired through the

signal averaging of 512 scans, with a 90° tip angle rf pulse. For the purpose of calculating the enhancement factor, it should be noted that signal averaging on the Bruker Avance 400 system is performed through simple addition of acquired FIDs. Thus, for the spectrum obtained with 748.8 torr of SEOP enhanced ^{129}Xe and a single 30° tip *rf* angle pulse which provided an NMR signal of integration 9.033 times that of the thermal standard, we have an enhancement factor, E , of

$$E = \frac{9.033 (SEOP)}{1.00 (Thermal)} \times \frac{\sin\left(\frac{\pi}{2}\right)}{\sin\left(\frac{\pi}{6}\right)} \times \frac{777 \text{ torr}}{748.8 \text{ torr}} \times \frac{512 \text{ scans}}{1 \text{ scan}} \approx 9.60 \times 10^3. \quad (\text{AII-6})$$

SEOP enhancement of the ^{129}Xe NMR signal is nearly 10^4 , corresponding to a nuclear polarization of 8.55 %.

APPENDIX III
APPARATUS FOR MEASUREMENT OF THE TIME-DEPENDENCE OF PRESSURE
DURING THE FORMATION OF THE XENON TYPE I CLATHRATE HYDRATE

Experimental Setup

Because real time measurements of xenon pressure during the formation of the type I deuteriohydrate were performed external to the NMR spectrometer, an apparatus was developed to accurately control the temperature of the sample tube in a manner similar to that found within NMR probes. **Figure AIII-1** depicts the system developed to control the sample temperature for the duration of the experiment. Stability of the sample temperature is paramount due to the sensitivity of the measured pressure to changes in temperature. The system presented maintained the sample to ± 0.2 °C for the duration of the experiment.

The sample chamber consisted of an outer PVC (polyvinylchloride) casing and an inner PVC chamber, with expanding foam used to as insulation in the lining. After flowing through a coil inserted in cryogenic bath, the dry nitrogen gas stream enters the lower portion of the sample chamber, and exits the upper portion. The chilled gas flows vertically upward, in a manner similar to the flow in the NMR probe. Careful control of the gas stream flow rate accurately maintains the temperature at the desired value.

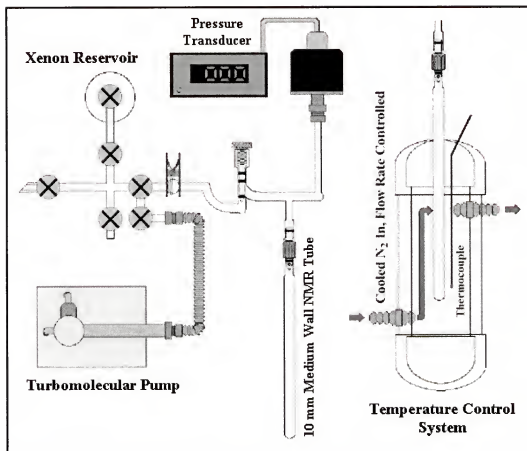


Figure AIII-1. Apparatus for real-time measurement of pressure during the formation of the xenon type I clathrate hydrate. A known quantity of xenon gas was expanded into the branched region above the sample tube, which was maintained at the desired temperature (± 0.02 °C). Opening of the NMR tube valve allowed the xenon gas to expand, and provide an appropriate initial starting point.

The pressure was measured with an MKS pressure transducer, as it was enclathrated into the ice. The transducer provides a DC output in mV that is directly proportional to the measured pressure; this output was coupled to a computer and data points were acquired with a short recycle time (1 to 5 s, typically). Hysteresis of the transducer is short compared to the sampling time, allowing for real-time measurement of the pressure.

REFERENCES

1. Walker, T.G. *Phys. Rev. A*, **1989**, 40(9), 4959.
2. Cates, G.D.; Fitzgerald, R.J.; Barton, A.S.; Bogorad, P.; Gatzke, M.; Newbury, N.R.; Saam, B. *Phys. Rev. A*, **1992**, 45(7), 4631.
3. Walker, T.G.; Thywissen, J.H.; Happer, W. *Phys. Rev. A*, **1997**, 56(3), 2090.
4. Anderson, L.W.; Pipkin, F.M.; Baird, J.C. *Phys. Rev.*, **1959**, 116, 87.
5. Barrat, J.P.; Cohen-Tannoudji, C. *J. Phys. (Paris)*, **1961**, 22, 329.
6. Bouchiat, M.A. *J. Phys. Radium*, **1963**, 24, 379.
7. Walker, T.G.; Happer, W. *Rev. Mod. Phys.* **1997**, 69, 629.
8. Bouchiat, M.A.; Carver, T.R.; Varnum, C.N. *Phys. Rev. Lett.* **1960**, 5, 373.
9. Fraissard, J.; Ito, T. *Zeolites* **1988**, 8, 350.
10. Fraissard, J. *Phys. Chem.* **1988**, 269, 657.
11. Ito, T.; Fraissard, J. in *Int. Conf. Zeolites*; Heyden; Naples, **1980**, Pp. 150.
12. Davidson, D.W.; Handa, Y.P.; Ripmeester, J.A. *J. Phys. Chem.* **1986**, 90, 6549.
13. Bowers, C.R.; Driehuys, B. *NHMFL Newsletter – Look up Dates*.
14. Pietraß, T.; Gaede, H.C. *Adv. Mater.* **1995**, 7(10), 826.
15. Ripmeester, J.A.; Davidson, D.W. *Bull. Magn. Reson.* **1981**, 2, 139.
16. Ripmeester, J.A.; Ratcliffe, C.I.; Tse, J.S. *J. Chem. Soc. Faraday Trans. I* **1988**, 84, 3731.
17. Jokisaari, J. *Progress in NMR Spectroscopy*, **1994**, 26, 1.
18. Stengle, T.R.; Hosseini, S.M.; Williamson, K.L. *J. Sol. Chem.* **1986**, 15(9), 777.
19. Raftery, D.; Long, H.; Meersman, T.; Grandinetti, P.J.; Reven, L. Pines, W. *Phys. Rev. Lett.* **1991**, 66, 584.

-
20. Pietraß, T.; Kneller, J.M.; Assink, R.A.; Anderson, M.T. *J. Phys. Chem. B* **1999**, *103*(42), 8837.
 21. Terskikh, V.V.; Mudrakovskii, I.L.; Mastikhin, V.M. *J. Chem. Soc., Faraday Trans.* **1993**, *89*(23), 4239.
 22. Davidson, D.W.; Ripmeester, J.A. "NMR, NQR and Dielectric Properties of Clathrates" in *Inclusion Compounds*, Volume 3, Atwood, J.L. *et al.*, ed. **1984** (Academic).
 23. Ripmeester, J.A. *J. Am. Chem. Soc.* **1982**, *104*, 289.
 24. Ripmeester, J.A.; Davidson, D.W. *J. Mol. Struct.* **1981**, *74*, 67.
 25. Pietraß, T.; Gaede, H.C.; Bifone, A.; Pines, A.; Ripmeester, J.A. *J. Am. Chem. Soc.* **1995**, *117*, 7520.
 26. Schoenborn, B.P.; Watson, H.C.; Kendrew, J.C. *Nature* **1965**, *207*, 28.
 27. Schoenborn, B.P. *Nature* **1965**, *208*, 760.
 28. Schiltz, M.; Fourme, R.; Broutin, I.; Prange, T. *Structure* **1995**, *3*(3), 309.
 29. Moudrakovski I.L.; Sanchez A.A.; Ratcliffe C.I.; Ripmeester J.A. *J. Phys. Chem. B* **2001**, *105*, 12338.
 30. Moudrakovski I.L.; Ratcliffe C.I.; Ripmeester J.A. *Angew. Chem. Int. Ed.* **2001**, *40*, 3890.
 31. Storhaug, V.J.; Liebig, F.; Bowers, C.R. *J. Phys. Chem. B* **2002**, *106*, 2884.
 32. Mason, J., in *Multinuclear NMR*, Plenum Press, New York, USA, 1987.
 33. Horikawa, S.; Itoh H.; Tabata, J.; Kawamura, K.; Hondoh, T. *J. Phys. Chem. B* **1997**, *101*, 6290.
 34. Jameson, A.K.; Jameson, C.J.; Gutowski, H.S. *J. Chem. Phys.* **1970**, *53*(6), 2310.
 35. Stengle, T.R.; Reo, N.V.; Williamson, K.L. *J. Phys. Chem.* **1981**, *85*, 3772.
 36. Derouane, E.G.; Nagy, J.B. *Chem. Phys. Lett.* **1987**, *137*(4), 341.
 37. Jameson, C.J.; de Dios, A.C. *J. Chem. Phys.* **1992**, *97*(1), 417.

-
38. Springuel-Huet, M.A.; Bonardet, J.L.; Gédéon, A.; Fraissard, J. *Magn. Reson. Chem.* **1999**, *37*, S1.
 39. Horikawa, S.; Itoh, H.; Tabata, J.; Kawamura, K.; Hondoh, T. *J. Phys. Chem. B* **1997**, *101*, 6290.
 40. Wittebort, R.J.; Olejniczak, E.T.; Griffin, R.G. *J. Chem. Phys.* **1987**, *86*, 5411.
 41. Handa, Y.P.; Tse, J.S. *J. Phys. Chem.* **1986**, *90*, 5917-5921
 42. Sloan, E. Dendy, Jr. *Clathrate Hydrates of Natural Gases*, Marcel Dekker, Inc.: New York, 1990.
 43. Collins, M.J.; Ratcliffe, C.I.; Ripmeester, J.A. *J. Phys. Chem.* **1990**, *94*, 157.
 44. Garg, S.K.; Gough, S.R.; Davidson, D.W. *J. Chem. Phys.* **1975**, *63*, 1646.
 45. Stengle, T.R.; Reo, N.V.; Williamson, K.L. *J. Phys. Chem.* **1981**, *85*, 3772.
 46. Mason, J., in *Multinuclear NMR*, Plenum Press, New York, USA, 1987.
 47. Ripmeester, J.A.; Ratcliffe, C.I. *J. Phys. Chem.* **1990**, *94*, 8773.
 48. Pines, A.; Gibby, M.G.; Waugh, J.S., *J. Chem. Phys.*, **1973**, *59*, 569.
 49. Levron, D.; Walter, D.K.; Appelt, S.; Fitzgerald, D.K.; Korbly, S.E.; Sauer, K.L.; Happer, W.; Earles, T.L.; Mawst, L.J.; Botez, D.; Harvey, M.; DiMarco, I.; Conolly, J.C.; Möller, H.E.; Chen, X.J.; Cofer, G.P.; Johnson, G.A. *Appl. Phys. Lett.* **1998**, *73*(18), 2666.
 50. Driehuys, B.; Cates, G.D.; Miron, E.; Sauer, K.; Walter, D.K.; Happer, W. *Appl. Phys. Lett.*, **1996**, *69*, 1668.
 51. Zeng, X.; Miron, E.; van Wijngaarden, A.; Schreiber, D.; Happer, W. *Phys. Lett.* **1983**, *96*, 191.
 52. Sieradzan, A.; Franz, F.A. *Physical Review A*, **1982**, *25*, 2985.
 53. Appelt, S.; Baranga, A.B.; Erickson, C.J.; Romalis, M.V.; Young, A.R.; Happer, W. *Phys. Rev. A*, **1998**, *58*, 1412.
 54. Appelt, S.; Ünlü, T.; Zilles, K.; Shah, N.J.; Baer-Lang, S.; Halling, H. *Appl. Phys. Lett.*, **1999**, *75*, 427.

-
72. Bowers, C.R.; Long, H.W.; Pietra, T.; Gaede, H.C.; Pines, A. *Chem. Phys. Lett.* **1993**, *205*, 168.
 73. Hartmann, S.R.; Hahn, E.L. *Phys. Rev.* **1962**, *128*, 2042.
 74. Long, H.W.; Gaede, H.C.; Shore, J.; Reven, L.; Bowers, C.R.; Kritzenberger, J.; Pietraß, T.; Pines, A. *J. Am. Chem. Soc.* **1993**, *115*, 8491.
 75. Solomon, I. *Phys. Rev.* **1955**, *99*, 559.
 76. Robbins, T.; Knobler, C.B.; Bellew, D.R.; Cram, D.J. *J. Am. Chem. Soc.* **1994**, *116*, 111.
 77. Cram, D.J.; Tanner, M.E.; Knobler, C.B. *J. Am. Chem. Soc.* **1991**, *113*, 7717.
 78. Branda, N.; Grotzfield, R.M.; Valdés, C.; Rebek, J., Jr. *J. Am. Chem. Soc.* **1995**, *117*, 85.
 79. Luhmer, M.; Goodson, B.M.; Song, Y.Q.; Laws, D.D. Kaiser, L.; Cyrier, M.C.; Pines, A. *J. Am. Chem. Soc.* **1999**, *121*, 3502.
 80. Bartik, K.; Luhmer, M. Dutasta, J.-P.; Collet, A.; Reisse, J. *J. Am. Chem. Soc.* **1998**, *120*, 784.
 81. Brotin, T.; Lesage, B.A.; Emsley, L.; Collet, A. *J. Am. Chem. Soc.* **2000**, *122*, 1171.
 82. Wolber, J.; Doran, S.J.; Leach, M.O.; Bifone, A. *Chem. Phys. Lett.* **1998**, *296*, 391.
 83. Jansch, H. J.; Hof, T.; Ruth, U.; Schmidt, J.; Stahl, D.; Fick, D. *Chem. Phys. Lett.* **1998**, *296*, 146.
 84. Davies, G.R.; Halstead, T.K.; Greenhow, R.C.; Packer, K.J. *Chem. Phys. Lett.* **1994**, *230*, 237.
 85. Meersman, T.; Logan, J.W.; Simonutti, R.; Caldarelli, S.; Comotti, A.; Sozanni, P.; Kaiser, L.; Pines, A. *J. Phys. Chem.* **2000**, *104*, 11665.
 86. Haake, M.; Pines, A.; Reimer, J.A.; Seydoux, R. *J. Am. Chem. Soc.* **1997**, *119*, 11711.
 87. Seydoux, R.; Pines, A.; Maake, M.; Reimer, J.A. *J. Phys. Chem. B* **1999**, *103*, 4629.

-
88. Nossov, A.V.; Soldatov, D.V.; Ripmeester, J.A. *J. Am. Chem. Soc.* **2001**, *123*, 3563.
 89. Soldatov, D.V.; Ripmeester, J.A.; Sheringa, S.I.; Sokolov, I.E.; Zanina, A.S.; Gromilov, S.A.; Dyadin, Yu.A. *J. Am. Chem. Soc.* **1999**, *121*, 4179.
 90. Soldatov, D.V.; Ripmeester, J.A. *Chem. Mater.* **2000**, *12*, 1827.
 91. Holloway, John H., **1968**, *Noble-Gas Chemistry* (Methuen & Co., Ltd.)
 92. Jeffrey, G.A. "Hydrate Inclusion Compounds" in *Inclusion Compounds*, Volume 1, Atwood, J.L. et al., ed. **1984** (Academic).
 93. Villard, P. *Compt. Rend.* **1896**, *123*, 377.
 94. von Stackelberg, M.; Müller, H.R. *Zeit. Electrochem.* **1954**, *58*, 25.
 95. De Forcrand, R.H. *Compt. Rend.* **1923**, *176*, 335.
 96. De Forcrand, R.H. *Compt. Rend.* **1925**, *181*, 15.
 97. Sparks, K.A.; Tester, J.W.; Cao, Z.; Trout, B.L. *J. Phys. Chem. B* **1999**, *103*, 6300.
 98. Ripmeester, J.A.; Ratcliffe, C. I.; Tse, J.S. *J. Chem. Soc., Faraday Trans. I* **1988**, *12*, 3731.
 99. Cady, G.H. *J. Chem. Ed.* **1983**, *60*(11), 815.
 100. Barrer, R.M.; Edge, A.V.J. *Proc. Roy. Soc. A* **1967**, *300*, 1.
 101. Parsonage, N.G.; Staveley, L.A.K. "Thermodynamic Studies of Clathrates and Inclusion Compounds" in *Inclusion Compounds*, Volume 3, Atwood, J.L. et al., ed. **1984** (Academic).
 102. Dharmawardhana, P.B.; Parrish, W.R., Sloan E.D. *Ind. Eng. Chem. Fund.* **1980**, *19*(4), 410.
 103. Handa, Y.P.; Tse, J.S. *J. Phys. Chem.* **1986**, *90*, 5917.
 104. Davidson, D.W.; Handa, Y.P.; Ratcliffe, C.I.; Tse, J.S.; Powell, B.M. *Nature* **1984**, *311*, 142.
 105. Collins, M.J.; Ratcliffe, C.I.; Ripmeester, J.A. *J. Phys. Chem.* **1990**, *94*, 157-162.

-
106. Falabella, B.J. *A Study of Natural Gas Hydrates*, Dissertation, U. Mass., 1975, Ann Arbor, MI.
 107. Falabella, B.J.; Vanpee, M. *Ind. Eng. Chem. Fund.* **1974**, *13*, 228.
 108. Makogon, Y.F. *Hydrates of Natural Gases*, Moscow, Nedra, Izadatelstro, 1980, Pp. 208.
 109. Chen, T.S. *A Molecular Dynamic Study of the Stability of Small Prenucleation Water Clusters*, Dissertation, U. Missouri-Rolla, 1980, Ann Arbor, Michigan.
 110. Rodger, P.M. *Ann. N.Y. Acad. Sci.* **2000**, *912*, 474.
 111. Uchida, T.; Ebinuma, T.; Narita, H. *J. Cryst. Growth* **2000**, *217*, 189.
 112. Hwang, M.J.; Wright, D.A.; Kapur, A.; Holder, G.D. *J. Inclus. Phenom.* D.W. Davidson Memorial Volume, 1989.
 113. Barrer, R.M.; Ruzicka, D.J. *J. Chem. Soc., Faraday Trans.* **1962**, *58*, 2253.
 114. Barrer, R.M.; Ruzicka, D.J. *J. Chem. Soc., Faraday Trans.* **1962**, *58*, 2262.
 115. Miller, S.L.; Smythe, W.D. *Science*, **1970**, *170*, 531.
 116. Selim M.S.; Sloan E.D.; Ullerich J.W. *AIChE Journal* **1987**, *33*(5), 747.
 117. Bishnoi, P.R.; Vysniauskas, A. *Kinetics of Gas Hydrate Formation Pt. II*, Final Report to the Gas Research Institute, Chicago, 1980.
 118. Englezos, P.; Kalogerakis, N.; Dholabhai, P.D.; Bishnoi, P.R. *Chem. Eng. Sci.* **1987**, *42*(11), 2647.
 119. Sloan E.D., Fleyfel F. *AIChE J.* **1991**, *37*(9), 1281.
 120. Baez, L.A.; Clancy, P. *Ann. N. Y. Acad. Sci.* **1994**, *715*, 177.
 121. Moudrakovski, I.L.; Sanchez, A.A.; Ratcliffe, C.I.; Ripmeester, J.A. *J. Phys. Chem. B* **2001**, *105*, 12338.
 122. Moudrakovski, I.L.; Ratcliffe, C.I.; Ripmeester, J.A. *Angew. Chem. Int. Ed.* **2001**, *40*, 3890.
 123. Ripmeester, J.A.; Ratcliffe, C.I. *J. Phys. Chem.* **1988**, *92*, 337.

-
124. Ripmeester, J.A.; Ratcliffe, C.I., *Energy Fuels*, **1998**, *12*, 197.
 125. Jacobs, D.M.; Zeidler, M.D.; Kanert, O. *J. Phys. Chem. A* **1997**, *101*, 5241.
 126. Ripmeester, J.A.; Ratcliffe, C.T. In *Inclusion Compounds*; Atwood, J.L.; Davies, J.E.D.; MacNicol, D.D., Eds.; Oxford University Press; Oxford, **1991**, Vol. 5, Chapter 2.
 127. Clausen, W.F. *J. Phys. Chem.* **1951**, *19*, 259.
 128. von Stackelberg, M.; Müller, H.R. *J. Phys. Chem.* **1951**, *19*, 1319.
 129. Storhaug, V.J.; Liebig, F.; Bowers, C.R.; *XeMAT 2000*, Siestre Levante, Italy, 2000.
 130. Pines, A.; Gibby, M.G.; Waugh, J.S., *J. Chem. Phys.*, **1973**, *59*, 569.
 131. Zeng, X.; Wu, Z.; Call, T.; Miron, E.; Schreiber, D.; Happer, W. *Phys. Rev. A*. **1985**, *31*, 260.
 132. Brunner, E.; Seydoux, R.; Haake, M.; Pines, A.; Reimer, J.A. *J. Magn. Res.* **1998**, *130*, 145.
 133. Bowers, C.R.; Pietrass, T.; Barash, E.; Pines, A.; Grubbs, R.K.; Alivisatos, A.P. *J. Phys. Chem.* **1994**, *98* 9400.
 134. Bowers, C.R.; Storhaug, V.; Webster, C.E.; Bharatam, J.; Cottone III, A., Gianna, R.; Betsey, K.; Gaffney, B.J., *J. Am. Chem. Soc.* **1999**, *121*, 9370.
 135. From the *CRC Handbook of Chemistry and Physics*, Weast, R.C.; Lide, D.R.; Astle, M.J.; Beyer, W.H., Eds.; CRC Press, Inc.; Boca Raton, **1989**, p. D-194.
 136. Dunn, M.B.; McDowell, C.A. *Chem. Phys. Lett.* **1972**, *15*(4), 508.
 137. Ikeda, T.; Mae, S.; Yamamuro, O.; Matsuo, T.; Ikeda, S.; Ibberson, R.M. *J. Phys. Chem. A* **2000**, *104*, 10623.
 138. Gough, S.R.; Hawkins, R.E.; Morris, B.; Davidson, D.W. *J. Phys. Chem.* **1973**, *77*(25), 2969.
 139. Garg, S.K.; Davidson, D.W. *Chem. Phys. Lett.* **1972**, *13*(1), 73.
 140. Garg, S.K. *J. Chem. Phys.* **1977**, *66*(6), 2517.

-
141. Dunn, M.B.; McDowell, C.A. *Chem. Phys. Lett.* **1972**, *13*(3), 268.
 142. Majid, Y. A.; Garg, S. K.; Davidson, D. W., *Can. J. Chem.*, **1968**, *46*, 1683.
 143. Davidson, D.W.; Garg, S.K.; Ratcliffe, C.I.; Tse, J.S.; Gough, S.R. *Can. J. Chem.* **1984**, *62*, 1229.
 144. Seife, C. *Science* **1996**, *152*, 2061.
 145. Dash, J.G.; Fu, H.Y.; Wettlaufer, J.S. *Rep. Prog. Phys.* **1995**, *58*, 115.
 146. Clary, D.C. *Science* **1996**, *271*, 1509.
 147. Mantz, Y.A.; Geiger, F.M.; Molina, L.T.; Molina, M.J.; Trout, B.L. *J. Chem. Phys.* **2000**, *113*(23), 10733.
 148. Davidson, D.W.; Ripmeester, J.A. In *Inclusion Compounds*; Atwood, J.L.; Davies, J.E.D.; MacNicol, D.D., Eds.; Oxford University Press; Oxford, **1984**, Vol. 3, Chapter 3.
 149. Albert, M.S.; Cates, G.D.; Driehuys, B.; Happer, W.; Saam, B.; Springer, C.S. Jr.; Wishnia, A. *Nature* **1994**, *370*, 199.
 150. Wolber, J.; Cherubini, A.; Dzik-Jurasz, A.S.K.; Leach, M.O.; Bifone, A. *Proc. Natl. Acad. Sci. U.S.A.* **1999**, *96*, 3664.
 151. Navon, G.; Song, Y.-Q.; Room, T.; Appelt, S.; Taylor, R.E.; Pines, A. *Science* **1996**, *271*, 1848.
 152. Tseng, C.H.; Wong, G.P.; Pomeroy, V.R.; Mair, R.W.; Hinton, D.P.; Hoffmann, D.; Stoner, R.E.; Hersman, F.W.; Cory, D.G.; Walsworth, R.L. *Phys. Rev. Lett.* **1998**, *81*, 3785.
 153. Ruth, U.; Hof, T.; Schmidt, J.; Fick, D.; Jänsch, H.J. *Appl. Phys. B* **1999**, *68*, 93.
 154. Gatzke, M.; Cates, G.D.; Driehuys, B.; Fox, D.; Happer, W.; Saam, B. *Phys. Rev. Lett.* **1993**, *70*, 690.
 155. Fitzgerald, R.J.; Sauer, K.L.; Happer, W. *Chem. Phys. Lett.* **1998**, *284*, 87.
 156. Gaffney, B.J. *Annu. Rev. Biophys. Biomol. Struct.* **1996**, *25*, 431.
 157. Boyington, J.C.; Gaffney, B.J.; Amzel, L.M. *Science* **1993**, *260*, 1482.

-
158. Minor, W.; Steczko, J.; Bolin, J.T.; Otwinowski, Z.; Axelrod, B. *Biochemistry* **1993**, 32, 6320.
 159. Schoenborn, B.P. *J. Mol. Biol.* **1969**, 45, 297.
 160. Tilton, R.F. Jr.; Kuntz, I.D., Jr. *Biochemistry* **1982**, 21, 6850.
 161. Tilton, R.F., Jr.; Kuntz, I.D., Jr.; Petsko, G. A. *Biochemistry* **1984**, 23, 2849.
 162. Prange, T.; Schiltz, M.; Pernot, L.; Colloc'h, N.; Longhi, S.; Bourguet W.; Fourme, R. *Proteins: Struct., Funct., Genet.* **1998**, 30, 61.
 163. Schoenborn, B.P. *Nature (London)* **1967**, 214, 1120.
 164. Feher, V.A.; Baldwin, E.P.; Dahlquist, F.W. *Nat. Struct. Biol.* **1996**, 3, 516.
 165. Samuelsson, B., Ramwell, P.W., Paoletti, R., Folco, G., Granström, E., Nicosia, S., Eds. *Advances in Prostaglandin, Thromboxane and Leukotriene Research*, v. 23; Raven Press: New York, 1995.
 166. Minor, W.; Steczko, J.; Stec, B.; Otwinowski, Z.; Bolin, J.T.; Walter, R.; Axelrod, B. *Biochemistry* **1996**, 35, 10687.
 167. Skrzypczak-Jankun, E.; Amzel, L. M.; Kroa, B.A.; Funk, M.O. *Proteins: Struct. Funct. Genet.* **1997**, 29, 15.
 168. Gillmor, S.A.; Villasenor, A.; Fletterick, R.; Sigal, E.; Browner, M.F. *Nat. Struct. Biol.* **1997**, 4, 1003.
 169. Tilton, R.F. Jr.; Singh, U.C.; Weiner, S.J.; Connolly, M.L.; Kuntz, I.D. Jr.; Kollman, P.A. *J. Mol. Biol.* **1986**, 192, 443.
 170. Ewing, G.J.; Maestas, S. *J. Phys. Chem.* **1970**, 74, 2341.
 171. Prangé, T.; Schiltz, M.; Pernot, L.; Colloc'h, N.; Longhi, S.; Bourguet, W.; Fourme, R. *Proteins: Structure, Function and Genetics* **1998**, 30, 61.
 172. Brunori, M.; Vallone, B.; Cuttruzolla, F.; Travaglini-Allocatelli, C.; Berendzen, J.; Chu, K.; Sweet, R.M.; Schlichting, I. *Proc. Natl. Acad. Sci. USA* **2000**, 97, 2058
 173. Clapp, C.H.; Senchak, S.; Stover, T. J.; Potter, T.C.; Findeis, P.M.; Novak, M.J. *J. Am. Chem. Soc.* **2001**, 123, 747.

-
174. Boyington J.C.; Gaffney B.J.; Amzel L.M. *J. Biol. Chem.* **1990**, 265(22), 12771.
175. Clapp, C. H.; McKown, J.; Xu, H.; Grandizio, A. M.; Yang, G.; Fayer, J. *Biochemistry* **2000**, 39, 2603.
176. Minor, W., Steczko, J.; Bolin, J.T.; Otwinowski, Z.; Axelrod, B. *Biochemistry* **1993**, 32, 6320.
177. Fevold, H.L. *Adv. in Protein Chem.* **1951**, 6, 188.
178. Gordon, A.J.; Ford, R.A. *The Chemist's Companion*; John Wiley and Sons, New York, **1972**, p. 451.
179. Gaffney, B.J.; Mavrophilipos, D.V.; Doctor, K.S. *Biophys. J.* **1993**, 64, 773.
180. Axelrod, B.; Cheesbrough, T. M.; Laakso, S. *Methods Enzymol.* **1981**, 71, 441.
181. Brunauer, S.; Emmett, P.H.; Teller, E. *J. Am. Chem. Soc.* **1938**, 60, 309.
182. Drago, R.S.; Webster, C.E.; McGilvray, J.M. *J. Am. Chem. Soc.* **1998**, 120, 538.
183. Gordon, A.J.; Ford, R.A. *The Chemist's Companion*; John Wiley and Sons: New York, 1972, p 451.
184. Gaffney, B.J.; Sturtevant, J.M.; Yuan, S.M.; Lang, D.M.; Dagdigian, E. *Biophys. J.* **1994**, 66, A178.
185. Fraczekiewicz, R.; Braun, W. *J. Comput. Chem.* **1998**, 19, 319.
186. Privalov, P.L. *Annu. Rev. Biophys. Biophys. Chem.* **1989**, 18, 47.

BIOGRAPHICAL SKETCH

Vincent was born the only son of John P. and Beverly A. Storhaug, on January 27th, 1970, in Staten Island, New York. In 1979, his family moved to Florida, finally making their home, to this date, in the small town of Lake Helen, Florida. Vincent graduated valedictorian from DeLand Senior High School, in neighboring DeLand, Florida, in 1988. He then concentrated his search on small, liberal arts colleges and settled on a Presbyterian affiliated college in central Ohio.

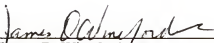
Vincent received his Bachelor's of Arts in Chemistry from College of Wooster, Wooster, Ohio. He applied and was accepted to the Department of Chemistry at Michigan State University that upcoming fall. After a little over a year at this position, Vincent decided to come a little closer to home, transferring from Michigan State to the Department of Chemistry at his final destination, the University of Florida, in Gainesville, Florida.

I certify that I have read this study and that in my opinion it conforms to acceptable standards of scholarly presentation and is fully adequate, in scope and quality as a thesis for the Doctor of Philosophy.



Clifford R. Bowers, Chairman
Associate Professor of Chemistry

I certify that I have read this study and that in my opinion it conforms to acceptable standards of scholarly presentation and is fully adequate, in scope and quality as a thesis for the Doctor of Philosophy.



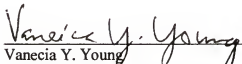
James D. Winefordner
Graduate Research Professor
of Chemistry

I certify that I have read this study and that in my opinion it conforms to acceptable standards of scholarly presentation and is fully adequate, in scope and quality as a thesis for the Doctor of Philosophy.



Martin H. Vala
Professor of Chemistry

I certify that I have read this study and that in my opinion it conforms to acceptable standards of scholarly presentation and is fully adequate, in scope and quality as a thesis for the Doctor of Philosophy.



Vanecia Y. Young
Associate Professor of Chemistry

I certify that I have read this study and that in my opinion it conforms to acceptable standards of scholarly presentation and is fully adequate, in scope and quality as a thesis for the Doctor of Philosophy.



Christopher D. Batich
Professor of Materials Science and
Engineering

This dissertation was submitted to the Graduate Faculty of the Department of Chemistry in the College of Liberal Arts and Sciences and to the Graduate School and was accepted as partial fulfillment of the requirements for the degree of Doctor of Philosophy.

December 2002

Dean, Graduate School